THE INFLUENCE OF CONTACT TRANSPARENCY ON THE SUPERCONDUCTING PROXIMITY EFFECT IN THIN SEMICONDUCTING FILMS

BY

MICHAEL ROBERT VISSERS

DISSERTATION

Submitted in partial fulfillment of the requirements
for the degree of Doctor of Philosophy in Physics
in the Graduate College of the
University of Illinois at Urbana-Champaign, 2009

Urbana, Illinois

Doctoral Committee:

Assistant Professor Nadya Mason, Chair
Professor James Eckstein, Director of Research
Professor Paul Goldbart
Professor James Wiss

Abstract

The superconducting proximity effect allows for the introduction of pair correlations into otherwise normal metals provided that they are coupled through a sufficiently transparent junction. The influence of this proximity effect manifests itself by modifying both the normal layer sheet resistance in the proximity affected region, R_s, and the junction conductance across the N-S boundary, G_c. These two quantities are impossible to measure simultaneously with any single two terminal device even if it is a four point measurement. However, a new three terminal device structure allows us to make two independent four point voltage measurements, which permits the extraction of these two intrinsic aspects of the proximity effect when combined with simple Ohm's law modeling. Devices with completely *in-situ* junctions between niobium and heavily doped n-GaAs and n-InAs were fabricated via molecular beam epitaxy. In order to reduce the Schottky barrier, a graded and delta-doped InGaAs cap was inserted at the interface. Careful construction of the doping profile in the cap allows for extremely transparent junctions just prior to the onset of superconductivity, the most transparent Nb-GaAs junctions yet reported. The transparency of the junction can be evaluated by calculating the number of available quantum channels between the two different Fermi surfaces and using the Landauer formalism to determine the ideal junction conductance. Comparison to the experimental junction conductance permits the discovery of the fundamental transmission coefficient for transport across the N-S interface. If the semiconducting depth is small enough the presence of correlations in the semiconductor are observed. Samples with deeper depths exhibit no direct evidence of superconductivity inside the

semiconductor. Samples consisting of doped InAs were also fabricated and measured. These samples exhibit almost perfect contact between the superconductor and the semiconductor and pair correlations are observed in the semiconductor despite their thickness. These observations confirm that the manifestation of the superconducting proximity effect is due to the competition between the normal and superconducting reservoirs. When the semiconducting layers are thick there exists a region that is unaffected by superconductivity. This region acts as an effective normal reservoir. The weak coupling at the Nb-InGaAs interface limits the strength of pairing in the semiconductor, and if a normal reservoir is present the superconductivity is completely suppressed. This effect is not seen in the more transparent InAs-Nb interfaces. This implies that the InAs is sufficiently transparent that the strong coupling to the superconductor across the N-S interface overcomes the negative effect on pairing due to the normal reservoir and a proximity affected region in the semiconductor near the interface is created. In summary, we are able to tune the strength of the induced pair correlations in the semiconductor by adjusting either the transmission coefficient of the N-S interface and by turning on or off the coupling to a normal reservoir.

To Jennifer

Acknowledgments

Many people helped to shepherd this project to its conclusion. In particular I would like to thank all the members of Jim Eckstein's group at Illinois. I would like to especially thank Soren Flexner for helping me understand the vagaries of GaAs Molecular Beam Epitaxy, patiently helping me through my numerous mistakes and showing me the importance of using deterministic mysticism to succeed in science. No matter how perfect the semiconducting structures I created were, they would have been worthless without Paul, Kevin, Tim, and Allison spending their valuable time, and using their pristine MBE chamber to grow room temperature Niobium for my devices. I would also like to thank Stephanie for her assistance in keeping the lab running and joining me in the quest for superconducting GaAs; I know the chamber is in good hands.

I would in particular like to thank Jim Eckstein for his indefatigable attitude that this project would be completed successfully despite the numerous setbacks, catastrophes, and frequent pilot error. It was always a pleasure discussing the experiment, the data, the problems, and the successes with him; I know that I am better scientist because of it.

In addition I would like to thank Doug Jeffers for his vital help on UHV technology, specifically the MBE chambers. He was always able to provide helpful advice that made the seemingly impossible repair jobs doable, and the apparently possible ones easy. I would like to also thank Tony, Kevin, and Bharat for keeping Microfab running as well as it did, and Scott, Tim, Vania, Jim, and Rick from the CMM for their assistance in characterizing our samples.

Finally, I would like to thank my wife, Jennifer, for spending her life here with me in Illinois. She put up with the late nights, long days, low pay, and the blatant disregard of science for regular working hours with far too good humor.

I would also like to thank the Department of Energy, Basic Energy Sciences, for providing funding for this work under the auspices of the Quantum Materials at the Nanoscale Cluster here at the Fred Seitz Materials Research Lab at the University of Illinois at Urbana-Champaign.

Table of Contents

Chapter 1 Introduction and Motivation

The superconducting proximity effect induces pair correlations in intrinsically non-superconducting materials. These correlations alter the transport in the normal metal and the transport across the normal-superconducting interface. Semiconductors are of particular interest in this field because they have a greatly reduced carrier concentration relative to the elemental superconductors. A semiconductor, even one doped at the semi-metallic limit, has thousands of times fewer carriers than a typical normal metal. This disparity in the carrier concentration implies that at a transparent N-S interface the superconductor will be able to enhance pair correlations in the semiconductor, but pairing in the superconductor should not be affected by the semiconductor. Recent experiments by Kastalsky *et al*. [1] have shown that it is possible to induce pair correlations in the semiconductor provided that the N-S interface is sufficiently transparent. Additionally, Nazarov's extension [2] of the Usadel theory of dirty superconductors [3] predicts that if the proximity affected region is also coupled to a physically separate normal reservoir, pair correlations in the proximity affected region will be suppressed.

In this project we have been able to fabricate extremely conductive N-S junctions by utilizing Indium based capping layers. The use of a 3 terminal device geometry and device theory, first introduced by Flexner [4], allows the extraction of the specific N-S junction conductance, G_c, and the sheet resistance in the proximity affected region, R_s. However the important parameter for determining the transparency of the N-S junction is not the conductance of the N-S junction, it is the transmission coefficient. This parameter can be found by comparing the measured G_c of our device to its ideal limit predicted by a

theory of contacts which we develop. Utilizing the Landauer formalism, the ideal contact conductance can be found by calculating the number of independent quantum modes carrying current to the junction. The most transparent $In_{0.30}Ga_{0.70}As$ capped devices we've made have a transmission coefficient $|T|^2$ =0.04. While these devices are the most conductive Nb-InGaAs interfaces yet reported, the N-S junction theory of Blonder, Tinkham, and Klapwijk [5] predicts that the probability of Andreev reflection in these junctions is still low. The low probability of Andreev reflection implies that the strength of the coupling between the superconductor and semiconductor will be weak which in turn weakens the proximity effect. This is further exacerbated in some of our sample architectures by the good contact of the proximity affected interfacial region to a thicker normal reservoir layer below it.

In the case of thick semiconducting and superconducting layers, the portion of the semiconductor furthest from the N-S interface will not be affected by superconductivity and apparently becomes an effective normal reservoir. If the proximity affected region in the semiconductor near the InGaAs-Nb interface is in contact to such a normal reservoir, the presence of superconductivity can be completely suppressed. The normal reservoir imposes a strong normal state boundary condition on the substrate side of the interface region. The weak coupling to the superconducting reservoir through the InGaAs-Nb interface cannot overcome this negative effect of the normal reservoir and in the language of Nazarov and Gueron the interface region is "pinned" in the normal state by the strong normal boundary condition. On the other hand, if the doped semiconductor layer is sufficiently thin, this effect goes away. When devices consisting of Niobium and just 200 Angstroms of semiconductor are tested, the entire semiconducting layer is influenced by

superconductivity and the normal reservoir is no longer present. The boundary condition on the substrate side of the interface region no longer fixed in the normal state, it is now free. Since the interface region is now solely influenced by the superconducting electrode, even the weak N-S coupling of the Nb-InGaAs interface causes pair correlations to exist near the N-S interface. These pair correlations are manifest as a slight decrease in the extracted sheet resistance of the proximity affected region and a zero bias conductance maximum. Since the proximity induced region is now only influenced by the superconducting electrode, Thouless predictions about how correlations disperse in a diffusive conductor as a function of temperature and energy should apply. For thicknesses larger than this 200A depth the presence of the normal reservoir adds an additional factor which suppresses these correlations at a much faster rate than the Thouless theory would predict as the layer thickness is increased. This crossover between the two regimes accounts for the large qualitative differences in the measured data between the thicker and thinner semiconducting layers with identical N-S interfaces.

We were also able to construct semiconducting structures completely out of InAs. Since InAs does not form a Schottky barrier to Nb, extremely transparent N-S interfaces are formed with $|T|^2$ =0.7. The use of this material therefore allows us to tune the transmission coefficient of the N-S interface to almost its theoretical limit set by Fermi velocity mismatch. Analysis using the BTK theory says that the probability of Andreev reflection is high. This high probability of Andreev reflection means that the superconducting reservoir is able to easily transmit pair correlations across the N-S interface and induce them in the semiconducting layer. The high probability of Andreev reflection results in an increased N-S junction conductance, and decreased sheet

resistance in the proximity affected region as the temperature is reduced. These correlations are present even when the proximity affected region is in intimate contact with a normal reservoir. The coupling to the superconducting reservoir through the ideally transparent InAs-Nb interface is strong enough to exceed the negative effect of coupling to the normal reservoir.

All of our findings can be summarized as follows: We were able to tune the strength of the induced pair correlations in the semiconductor by adjusting the transmission coefficient of the N-S interface and by turning on or off the coupling to a normal reservoir. For junctions with poor transmissivity, evidence for pair correlations was only found if the semiconducting layer was thin enough that none of it constituted a "normal reservoir". The transition between thin enough and too thick is not as smooth as the Thouless theory of correlation diffusion predicts, rather is almost discontinuous. We attribute this to a qualitative change in the nature of the boundary condition that the correlations have below the proximity effected layer, changing from pinned to the normal state in thicker samples to being free to float in thinner ones. The evidence for pair correlations in the thin layer samples is similar to what is seen in all samples using pure InAs as the semiconductor. In the case of InAs, the junction transmissivity is almost perfect and the pair correlations can survive at the interface even when the doped semiconductor layer is thick.

Chapter 2 Theory of the Superconducting Proximity Effect

There are several approaches to the theory of spatially dependent superconducting interactions, pairing, and correlations. Paired electrons behave at low energies as bosons, and condense into a macroscopic ground-state wavefunction. In the simplest approach one calculates the spatial variation via a Schrodinger-like wave equation. This approach, known as the Ginzburg-Landau theory, is based upon Landau's theory of second-order phase transitions. For a superconductor, the order parameter Ψ is complex, and functions as the macroscopic wavefunction for the condensed pairs; $|\Psi|^2$ is the density of pairs. The wave equation governing Ψ comes from minimizing a free energy functional involving powers of $|\Psi|^2$ and derivatives of Ψ.

Unlike the phenomenological Ginzburg-Landau approach, the formulation of Bardeen, Cooper, and Schrieffer (BCS) [6], provides a microscopic description of the condensed state in terms of a many body wavefunction. In its simplest form, BCS theory describes uniform superconductors, and does not allow for spatial variation of the superconducting properties. The Bogoliubov-de Gennes equations are an extension of the BCS theory that self-consistently permits the spatial variation of superconductivity. Utilizing these equations and the appropriate matching conditions for current continuity and momentum states at the boundary, Blonder, Tinkham, and Klapwijk [5] were able to calculate the effect of superconductivity on transport between semi-infinite normal and superconducting layers across a N-S junction of geometrical size comparable to a mean free path in diameter. The small lateral size of this junction causes the normal and

superconducting layers on both sides of the interface to be only weakly coupled. Even for a transparent contact, the coupling area is small, this means that the normal and superconducting layers retain their native states at the interface, normal on one side and pair correlated superconducting on the other. While this theory describes how the N-S junction transport changes with temperature, the weak-coupling nature of this contact means that the theory is not able to describe changes in any of the normal-layer transport properties, such as R_s, i.e., the sheet resistance of the proximity affected region.

In order to properly describe the interface region between the normal and superconducting layers a generalized theory of the proximity effect formulated by Usadel [3] should be used. This approach utilizes Green function techniques in dirty systems, i.e., the mean free path is less than the superconducting coherence length. This disorder renders all the interactions and governing equations effectively local, as the dynamics is averaged over a length determined by the mean free path which, in a disordered system, is small. The equations that then govern the strength of the pair correlations are solved using boundary conditions set by the physical state of the bounding material. Specifically, in our system the boundary materials are the contacts to the fully normal and superconducting reservoirs. Their solution provides the strength of the pair correlations throughout the N-S system, as a function of energy and of position.

By using this theory Nazarov [2] predicted that not only will superconductivity in the normal layer be induced by sufficiently strong coupling to a superconducting reservoir but also, coupling to a normal reservoir at a physically separate location will suppress the strength of superconductivity in the proximity-affected region. Our experimental results support the prediction that the strength of the pair correlations in the normal layer can be

tuned by adjusting the conductance of the N-S contact and being in electrical contact to a normal reservoir. These results are in accordance with the physical picture presented by Nazarov, even though the details of the experiment and theoretical calculation differ. In our case the "normal reservoir" is part of a thick layer of normal-state material. This layer is sufficiently thick that the region far from the superconducting reservoir remains normal. As will be described below, when the coupling to the normal reservoir is strong enough the reservoir then acts to suppress pair correlations in the region adjacent to the N-S interface. On the other hand, by making the N-layer sufficiently thin, the normal reservoir no longer is present, and this allows pair correlations in the normal layer to emerge. It is also the case that proximity coupling to the superconductor by means of a nearly perfectly transparent junction provides a stronger proximity effect, in which pair correlations can exist, even in the presence of coupling to a normal reservoir.

2.1 Ginzburg Landau Theory of the Proximity Effect

As mentioned in the previous subsection, the Ginzburg-Landau description of superconductivity starts with Landau's phenomenological theory of phase transitions and uses a complex order parameter Ψ that is closely related to the pair density in the superconductor. Ginzburg and Landau also postulated that $\Psi(r)$ is a spatially varying pseudo-wavefunction that describes the macroscopic ground state. They postulated that, in thermodynamic equilibrium, the wave function could be obtained by minimizing a free energy functional describing superconductivity and involving powers of $|\Psi|^2$ and spatial derivatives of $\Psi(r)$. In particular, this approach implies that spatial variations in the order parameter incur a cost to the free energy. At an N-S interface it is necessary to resort to

microscopic BCS theory to obtain the boundary condition on Ψ in the superconductor at the boundary [7]. Ginzburg-Landau theory is also not able to describe the effect of pair correlations on transport in the N-layer at an N-S junction without making *ad-hoc* postulates.

Thuneberg [8] used the time-dependent Ginzburg-Landau equation in order to describe the junction conductance and the presence of "excess current" at an N-S junction. In the high junction-transparency limit, he *postulated* that the superconductor would couple strongly to the normal material and, as a result, a small step discontinuity in the order parameter would exist on the normal side of the interface. Conversely in the low junction-transparency limit, the N-S coupling is weak and the order parameter should be very small on the normal side of the interface. Thuneberg found that when he solved, self-consistently, for the proximity-induced order parameter, there was a "supercurrent" contribution to the junction conductance only when the N-S junction was postulated to be transparent enough to have a nonzero order parameter in the N-layer. This additional current term manifests itself experimentally through a current greater than $G_N V$, i.e., the product of the high-bias conductance and the applied voltage. In our experiment we observe this excess current in almost-perfectly-transparent Nb-InAs junctions, and also when the normal layer is very thin. Thuneberg's analysis implies that there exists a nonzero value of the order parameter in the semiconductor in these two cases: when either (1) the N-S junction transparency is very high, or (2) when the normal layer is sufficiently thin.

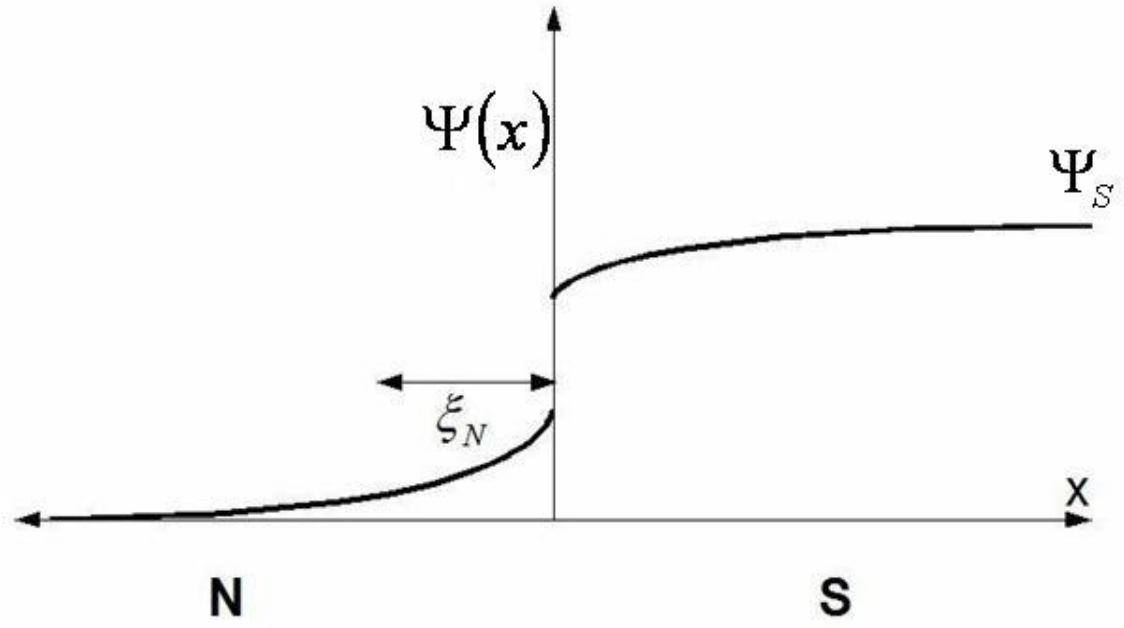

Figure 2.1: Graphical depiction of the order parameter Ψ(x) near the interface between thick normal and superconducting layers, obtained using the method of de Gennes [8]. Deep in the superconductor it reaches its bulk value Ψ_S, and deep in the normal metal it is zero. However, in the normal metal near the N-S interface the order parameter is nonzero and attenuates, spatially, with the characteristic length ξ_N defined in equation 2.2.

2.2 The de Gennes Approach

In contrast to the Ginzburg-Landau, purely phenomenological theory, BCS [6], developed a microscopic theory to describe the superconducting equilibrium state. They showed that an attractive interaction between electrons causes bound pairs of electrons, the bosonic members of the condensed state, to form at low temperatures. A key prediction of this theory is that the binding energy of a pair is 2Δ, where Δ is the energy gap of the superconductor. Gor'kov's analysis [9, 10] showed that the value of the Ginzburg-Landau order parameter Ψ(r) was proportional to the local value of the energy gap Δ(r), at least near the superconducting critical temperature T_c, and the Ginzburg-Landau formulation was therefore able to be derived from microscopic theory. Using the

Ginzburg-Landau equations and the Gor'kov microscopic theory for the N-S interface, the earliest complete treatment for the proximity effect at a N-S contact was developed by de Gennes in the 1960's [7, 11], and was summarized by Deutscher and de Gennes in 1969 [12]. In the thick electrode limit, i.e., where the normal and superconducting layers are both semi-infinite in depth, de Gennes was able to derive a self-consistent expression for the order parameter in the N-S structure; an example of his solution is shown in Fig 2.1. Near T_c where the pair density is small, the theory defines an order parameter $\Delta(x)=\Psi(x)$ within the bilayer. At large distances from the interface, the order parameter reaches its normal-state value of $\Psi = 0$ or its unperturbed superconducting value of Ψ, i.e. Ψ_S. However, near the N-S interface it predicts there will be nonzero pairing amplitude in the normal metal as well as a suppression of superconductivity in the superconductor. In the superconducting layer near the interface, the rate of change of the order parameter with distance, $\partial\Psi/\partial x$, is proportional to the ratio of the normal-state densities of states at the Fermi level in the two materials, N_N/N_S [7]. In our experiments, the density of states in the superconductor, Nb, is 2000 times greater than the density of states in the semiconductor. Therefore, the rate of change of $\Psi(x)$ will be much smaller on the superconducting side of the interface, and the strength of pair correlations in the superconductor will not be substantially affected by the presence of the N-layer. In the normal metal, the order parameter drops exponentially with a characteristic length-scale given by the normal-state coherence length ξ_N, the distance over which the mates of a pair diffuse but remain coherent into the normal metal. If the normal metal is "clean" then the pair correlations penetrate a distance

$$\xi_N = \xi_T = \frac{\hbar v_F}{2\pi kT}. \tag{2.1}$$

This is because the pairs only decohere after the time required for their spread in momentum to cause them to become out of phase with each other. In the "dirty" limit, the mean free path l is less than ξ_T and, instead, the coherence length in the normal metal resembles a diffusion length, and is given by

$$\xi_N = \sqrt{\frac{\xi_T l}{3}} = \sqrt{\frac{\hbar v_F l}{6\pi kT}}. \tag{2.2}$$

The N-S structures that I created in this project are in the dirty limit, and are predicted to have a normal-state coherence length ξ_N =30nm at 9 K.

2.3 The Bogoliubov-de Gennes Equations and the Blonder-Tinkham-Klapwijk Model

As discussed earlier, BCS results were extended by Bogoliubov and de Gennes who employed a generalized form of the self-consistent Hartree-Fock approximation to describe superconductive pairing and quasiparticle excitations of the superconductor via a coupled pair of wave equations that describe one-electron and one-hole quasiparticle states. This allows for a description of spatially varying superconductivity.

Blonder, Tinkham, and Klapwijk (BTK) [5] model used these equations to describe ballistic transport across a small contact between the normal and superconducting layers. The transparency of this contact is modeled by a Dirac delta function barrier at the N-S interface which is parametrized by a dimensionless barrier strength Z. In reality, barriers at the N-S interface are due to nonzero thickness oxide layers having irregular potential

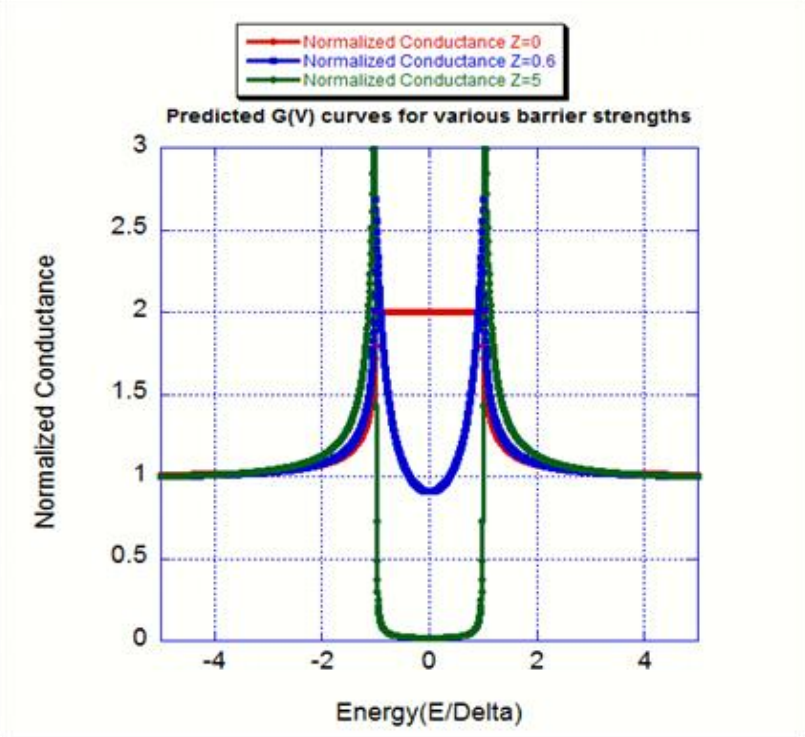

Figure 2.2: Plot of predicted normalized differential conductance versus bias voltage at zero temperature using the BTK model [5] for a perfect Z=0 interface, the Z=0.6 interface seen in the InAs devices, the Z=5 interface seen in the most transparent InGaAs devices.

profiles. The simplification to a delta function barrier vastly reduces the computational difficulty without significantly diminishing the overall power of the theory. The finite-sized rectangular or triangular barriers found in this project can be mapped to an equivalent delta-function barrier having an identical transmission coefficient for states near the Fermi energy.

BTK used the appropriate momentum state matching conditions across the boundary of the N-S interface. Four transport processes are possible, (a) Andreev reflection, (b) normal reflection, (c) single particle transmission and (d) single particle transmission with branch crossing to the other side of the Fermi surface. For voltages less than the gap energy, conservation of energy forbids the second two processes. The probabilities of these different outcomes were calculated as a function of energy and barrier strength Z.

The BTK model shows that the strength of the barrier at the interface plays a vital role in determining the current-voltage characteristics of the junction. Figure 2.2 shows the predicted differential conductance curves at zero temperature, obtained using the formulas for the probability of transmission in the BTK model [5] for a perfect Z=0 interface, the experimentally measured Z=0.6 barrier present in our InAs-Nb contacts, and the Z=5 barrier that describes our most transparent InGaAs contact. For small voltages, the conductance for small voltages drops dramatically as the barrier height increases; this is due to a rapid suppression of Andreev reflection when the barrier height is large. The sensitivity of Andreev reflection to barrier strength is due to its nature as a two-particle process. It is proportional to $|T|^4$, rather than the $|T|^2$ dependence appropriate for normal transport. In fact, in the less-transparent Nb-InGaAs junctions, the normalized zero-bias conductance is far smaller than the one we observed in the almost-perfectly transparent Nb-InAs junctions.

As discussed by Klapwijk [13] , Andreev reflection not only explains how electrons traverse the N-S boundary, it also describes the mechanism for coupling phase correlations from the superconductor into the normal metal. When an electron undergoes Andreev reflection at an N-S boundary, it carries with it a second electron, which occupies its time reversed single particle state and has opposite spin. When this process is aggregated over all of the incident Fermi surface, it leads to time-reversed opposite-spin pair-occupancy correlations in the normal metal. So the physical basis of the proximity effect is the Andreev reflection process. What Andreev reflection does not describe is the actual magnitude of resulting pair correlations. This is because the junction area in the Andreev process, for example as described by BTK, is assumed to be

very small; so small, in fact, that the impact of the induced pair correlations on the normal layer is negligible. The normal metal remains an uncorrelated normal metal. To describe the proximity effect, it is necessary to calculate how a large-area contact changes the electronic state in the two materials. The theory of Andreev reflection shows what the basic process is that leads to the transmission of pair correlations for each incident state, but it does not describe how the electronic state and energy levels change. As the N-S contact is assumed to be very small in area, BTK theory treats the normal and superconducting layers as if they are weakly coupled, regardless of the value of the transparency of the N-S interface, and the two layers remain in their respective states, even at the interface. No prediction is made about how induced superconductivity affects R_s or any of the other transport properties in the normal metal. Absent some mechanism to explain how the Andreev reflected state alters the transport in the normal metal, BTK theory does not provide a comprehensive description of the proximity effect.

2.4 The Usadel Equation

While the earliest treatments of the N-S interface relied on the Ginzburg-Landau equation near T_c, or solving the full non-local Gor'kov equations [9, 10], a more convenient theoretical framework [14] has been developed that can be used to determine the strength of the pair correlations as a function of position and how the density of states is altered as a function of energy. This quasi-classical equilibrium theory was first developed by Eilenberger [15] who assumed that the variation in the relevant quantities occurred on a length-scale much longer than the Fermi wavelength and, as a result, any dependences on the scale of the Fermi wavelength can be averaged out. Usadel [3] adapted this theory to dirty superconductors by introducing impurity-averaged Green

functions. In general, a Green function (also known as a propagator) describes the probability amplitude for an electron to travel from one place to another at a certain energy. Pair-correlation propagators account for the probability of correlations to be transmitted from points in the superconductor to those in the normal metal and *vice versa*, and the effect of superconductivity on transport as a function of both energy and position may be predicted using them. A thorough introduction to this approach and its applications to the proximity effect can be found in the dissertation of Gueron [16].

Instead of describing superconductivity through two-component plane-wave states, as

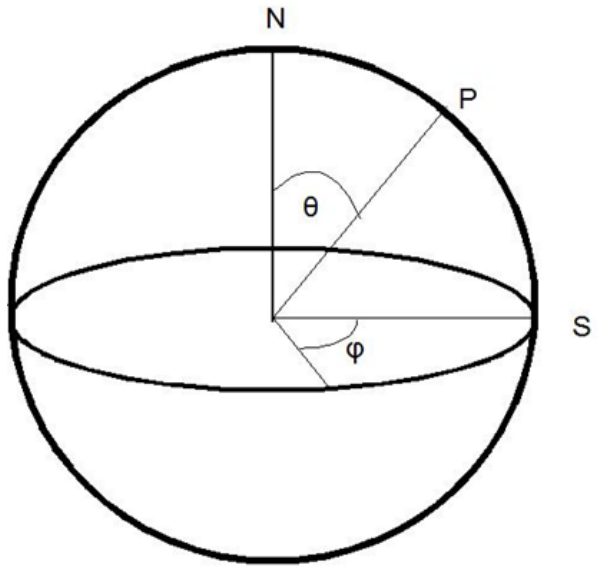

Figure 2.3: Nazarov's [2] parameterization of the strength of the proximity effect at a point P in terms of the pairing angle θ and the superconducting phase angle φ. The north pole of the sphere represents the normal reservoir which has no pairing at any energy, and the equator represents the superconducting reservoir at zero energy.

in the Bogoliubov-de Gennes equations, in the Green function approach the diffusive superconducting state is described using Usadel's three impurity averaged Green functions: $\hat{R}$, $\hat{A}$ and $\hat{K}$. The retarded and advanced Green functions, $\hat{R}$ and $\hat{A}$, describe

the equilibrium states of the system, and the Keldysh Green function, $\hat{K}$, allows for a description of transport. As described by Nazarov [2], these Green functions can be parametrized in a more intuitive and convenient form, by means of the two complex angles, θ(r, E) and φ(r, E), that define a complex unit sphere. A depiction of this sphere is shown in Fig. 2.4. The polar angle θ(r, E) quantifies the strength of pair correlations; it is a function of position and energy. The azimuthal angle φ(r, E) determines the superconducting phase. A location in space that is completely lacking in pair correlations is strictly normal, and would be characterized by a pairing angle equal to zero at all energies. Therefore, the normal metal will be represented on the sphere by the north pole. A position in space whose pairing angle cannot deviate from zero is defined to be a normal reservoir. The points on the sphere that describe a completely superconducting state have a latitude equal to the pairing angle $\theta \equiv \theta_{BCS} = \arctan i\frac{\Delta}{E}$ and lie at a longitude φ that is energy independent and equal to the phase of the superconducting wavefunction at that point [16]. At zero energy, a location that is completely in the superconducting state is represented by a point on the equator of the sphere with its longitude corresponding to its superconducting phase. A region whose pairing angle is fixed at the equator is taken to be a superconducting reservoir. In the simplest systems, the superconducting and normal reservoirs provide the boundary conditions to be imposed on the pairing angle determined via the Usadel equations.

A description of the proximity effect made in this manner transforms the equilibrium problem to a boundary value problem with known values of the pairing angle specified at the respective superconducting and normal electrodes. With these boundary conditions,

θ (r, E) can be found throughout the N-S interface region by solving the Usadel equation:

$$\frac{\hbar D}{2}\nabla^2\theta + \left(iE - \frac{\hbar}{\tau_{sf}}\cos\theta \right) + \Delta(x)\cos\theta = 0; \qquad (2.3)$$

this incorporates the diffusion constant in the normal metal D, and allows for spin-flip scattering via the term τ_{sf}. Solving this equation for θ leads to a number of diffusion-like equations that describe experimentally measurable quantities [16].

Belzig, Bruder, and Schon [17] studied a system comprising a thin dirty normal metal of thickness $L \approx \xi_N$ in perfect contact with a bulk superconductor on one side and an insulator on the other. The superconductor gives rise to the superconducting boundary condition $\theta = \pi/2$ at zero energy, and the insulator induces the boundary condition $d\theta/dx = 0$. The pairing angle θ is then solved for numerically, and a self-consistent solution for the strength of the correlations is then calculated as a function of position and energy. The authors thus obtained the density of states, normalized to its normal state value, i.e., $N(E)/N_0 = \mathrm{Re}[\cos\theta(x,E)]$, and found that the normal metal density of states develops a "minigap", i.e., a superconducting energy gap having a width in energy smaller than the full gap 2Δ present in the bulk superconductor. This gap, whose width is equal to 2Δ at the N-S interface, decreases with a characteristic depth $\sqrt{\hbar D/\Delta}$. It is also suppressed by spin-flip scattering. In our experiments, the diffusion constant that we calculate for semiconducting transport implies that the gapped state should persist to a depth of 50nm into the semiconductor. This distance is larger than we have observed experimentally. However, our system does not have perfect contacts and, more

importantly, in some of the devices we have tested it is also in contact with a normal reservoir.

The presence of such a normal reservoir, in addition to the superconducting reservoir, provides a source of normal electrons to couple to the proximity affected region. Nazarov [2] developed an Andreev circuit theory to describe the strength of pairing when both normal and superconducting reservoirs are connected to a thin normal wire. The relative strengths of these interfaces determine the degree of pair correlations at any point in the normal metal. As the conductance of the contact to the superconducting reservoir increases, the strength of the induced superconductivity increases as well. Conversely, superconductivity would be suppressed if the coupling to the normal reservoir is too strong. To account for the effect of both the normal and superconducting reservoirs, Gueron [16] found a mechanical analogy, illustrated in Fig 2.5, which she derived from Nazarov's Andreev circuit theory. By definition, both the normal and superconducting reservoirs are fixed at their boundary-value points, the north pole and the equator, respectively. An arbitrary point P is connected to both of these reservoirs by a spring whose stiffness is proportional to the conductance to the respective reservoir. Finding the value of the pairing angle at point P is equivalent to finding the equilibrium position of the pair of springs. In the limit in which the N-S junction conductance G_T is small compared to R^{-1} (i.e., the conductance of the diffusive link to the normal metal), the equilibrium position of the pairing angle at the point P is given by

$$\theta \approx RG_T . \qquad (2.4)$$

This equation implies that by adjusting the strength of the N-S conductance and the resistance of the coupling to the normal reservoir, the strength of the pair correlations can

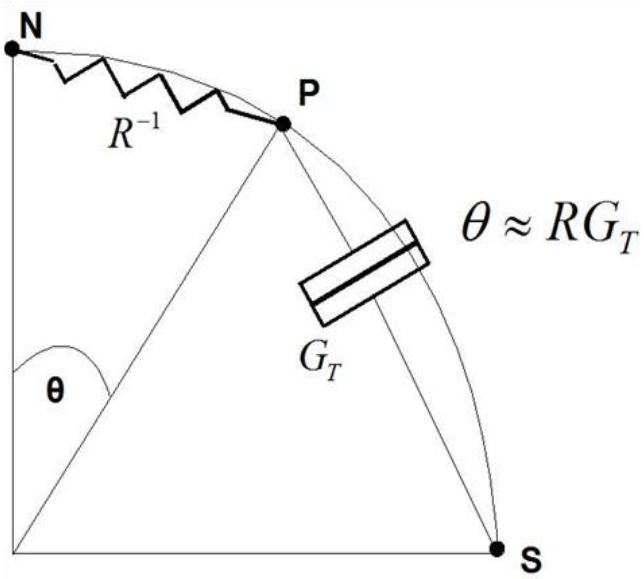

Figure 2.4: Toy model representation of the proximity affected region at point P connected to both a superconducting electrode and a normal reservoir. The strength of the two couplings determines the strength of the pair correlations in the proximity affected region. The stronger the spring connecting to the normal reservoir, the higher the junction conductance to the superconductor must be in order to have a large θ. Argument adapted from Nazarov [2] and Gueron [16]

be tuned. Strong contact to the normal reservoir would pin the proximity affected region to the normal reservoir, whereas weak coupling to the normal reservoir would allow a sufficiently transparent N-S junction to induce pair correlations, thus creating a proximity affected region. In the model, the tuning of θ was accomplished either by varying the transparency of the N-S interface or by adjusting the resistance of the diffusive link.

Usadel's quasiclassical theory of the proximity effect [3], and Nazarov's [2] application of it to an N-S interface region in electrical contact with normal and superconducting reservoirs provide us a theory for interpreting our experimental results. We outline our results here. Instead of having two distinct reservoirs coupled by diffusive wire, we instead have two thick slabs of superconducting and normal material. If the normal slab is thick enough, the part of the normal slab farthest from the interface is too far away to be affected by the superconductor. Since it remains in the normal-state

for all energies, this region acts as an effective normal reservoir. The normal slab is thus effectively divided into a potentially proximity affected region near the interface and a normal reservoir at large distance from the N-S interface. The interface region where the proximity effect leads to some degree of pair correlations couples with the superconducting reservoir through the N-S contact, and also couples to the normal reservoir beneath it. Therefore, the proximity affected region is coupled to both the superconducting and normal reservoirs in the same manner as the Nazarov model, and we expect its predictions to at least qualitatively describe our findings.

While the superconductor to semiconductor conductance is tunable by choosing different materials and growth architectures, it also depends on the quality of the N-S interface. On the other hand, the resistance between the two normal regions is small, fixed by the properties of the semiconductor, and cannot be as easily adjusted. While we cannot adjust the strength of the coupling of the proximity affected region to the normal reservoir independently, the thickness of the semiconducting layer can be adjusted. In the limit that the sample is made thin enough, the effective normal reservoir no longer exists. In our experiment we observe that devices with semiconducting layers that are only 200 Angstroms thick exhibit the presence of pair correlations; devices with thicker semiconducting layers do not. Additionally in another series of samples, by using InAs as the semiconductor, we were able to increase the junction transparency to very near its theoretical limit while keeping the thickness of the normal layer constant. In this situation we are also able to experimentally observe the presence of pair correlations. Despite the different experimental geometry from Nazarov's model presented above, these results are consistent with Nazarov's theory. As predicted, we are able to tune the strength of the

pair correlations in the normal metal by adjusting either the N-S junction conductance directly or the coupling of the interface region to a normal reservoir, in our case by varying the thickness of the normal film.

Chapter 3 Experimental Background

3.1 Introduction and Summary

The experimental study of the coupling between superconductors and semiconductors has attracted considerable interest in recent years, but has been unable to separately measure changes of transport in the proximity coupled semiconductor and through the semiconductor to superconductor junction until recently. The effectiveness of experimental studies in this field strongly depends on the device topology and geometry, and it was not until a new device structure was devised and analyzed by our group that these two manifestations of the proximity effect could be separately determined. Specifically, the superconducting proximity effect alters both the junction conductance across the N-S interface, G_c, and the sheet resistance in the proximity affected region, R_s. In order to fully understand the nature of the proximity effect it is necessary to measure both of these quantities - they are the fundamental quantities of interest. Earlier work by other groups did not do this.

The first study of superconductor to semiconductor transport devices was made by Kastalsky *et al.*[1] who observed a zero bias conductance peak in a device that contained a junction between niobium and the semiconductor, $In_{0.53}Ga_{0.47}As$. This result is in qualitative agreement with the Thuneberg's calculation [8] in that he (Thuneberg) postulated a finite if small order parameter in a normal layer in good contact with a superconductor. Based on that physical picture, it is natural to expect a high sensitivity of a nascent supercurrent on the the N-S junction conductance. It should be pointed out,

though, that the conductance measured by Kastalsky, as well as in all of the other research summarized here, contained not only the actual junction but transport through some normal semiconductor in series with the junction as well, it was a zero bias *device* conductance, not a zero bias junction conductance. In principle it is possible that the zero bias conductance peak observed was due to a reduced normal resistance of the semiconductor, since in Kastalsky's devices this was in series with the actual junction. None of the experiments done to date was able to unambiguously separate the zero bias *device* conductance enhancement into the junction transport and bulk transport components that compose it. Nevertheless, Kastalsky's experimental result was confirmed by the work of Giazotto *et al*. [18], and Taboryski *et al*. [19] both of whom measured superconducting contacts to GaAs, similarly configured. Both experiments observed an enhanced zero bias *device* conductance at low temperatures. Nguyen [20] examined a different device geometry using the low Schottky barrier material InAs, but his overall results were similar. As the device conductance was increased, the size of the temperature dependent transport enhancement increased and this was claimed in all cases to indicate an increased strength of pair correlations in the semiconductor.

All of these experiments only consisted of a single measurement and therefore are unable to separate out a change in the sheet resistance in the proximity affected region, R_s, from a change in the N-S junction conductance, G_c. We can estimate the relative contribution of these two device resistances. For example, using the device theory developed in Appendix B the measured resistance of a large 4 point contact similar to the ones used by Taboryski and Nguyen is $\frac{1}{w}\sqrt{\frac{R_s}{G_c}}$ where *w* is the transverse width of the

contact and G_c and R_s are the N-S junction conductance and sheet resistance in the proximity affected region respectively. A change in either of these quantities results in a change of the measured resistance, and these intrinsic quantities are unable to be separated if only a single measurement is made. Without the ability to extract out the intrinsic properties G_c and R_s it is impossible to understand the proximity effect.

To fix this a new device architecture was devised by Flexner [4]. The device structure provides electrodes to sample the voltage profile underneath an injector finger at two points. In that device, the shape of the voltage profile underneath the injector finger depends upon the transfer length, $\lambda = \sqrt{\frac{1}{G_c R_s}}$, which is a function of G_c and R_s. Since the voltage profile under the injector can be solved for, measuring the voltage values at two different points is enough to fully determine both G_c and R_s. The measurements in this project use a second generation version of this device.

3.2 Previous Experimental Work

The first study of the proximity effect in the superconductor semiconductor system was made by Kastalsky *et al.* [1] who studied the N-S interface between Nb and $In_{0.53}Ga_{0.47}As$ grown without strain on an Indium Phosphide substrate. As will be discussed further in section 5.1.3, the high Indium content of the semiconductor causes the native Schottky barrier to the semiconductor to be small, which should strengthen the proximity effect. Unfortunately in their experiment they had to remove the wafer from the MBE growth system and load it into another chamber to deposit the Niobium. They employed use of an Arsenic cap to attempt to protect the surface. After the

semiconducting layer was deposited, the sample was cooled and an Arsenic cap layer deposited on the surface. The purpose of the cap layer is to protect the interface when vacuum is broken and the sample taken to the Nb chamber for the deposition of the superconducting electrode. Devices were then fabricated by the creation of 20μm x 20μm mesas which could be measured with 4 point contacts to either another mesa or to the back side of the substrate. Data was only taken in a single measurement configuration which included contributions from both the N-S junction and the series resistance in the semiconductor. However, the series resistance was claimed to only be 0.1 Ohm and was much less than the remaining junction resistance.

When measured, this structure exhibited a decrease in the zero-bias conductance just below the critical temperature of the Niobium. The magnitude of this decrease in the conductance was strongly related to the doping in the semiconductor and the junctions became 100 times more conductive when the charge density was increased from $1x10^{18}$ cm^{-3} to $2.5x10^{19}$ cm^{-3}. This change in conductance was attributed to the reduction of the depth of the Schottky barrier at the interface due to the increased number of carriers in the semiconductor. This barrier and solutions to it will be discussed in further detail in Section 4.2.2. Furthermore, when the more conductive samples were taken to sufficiently low enough temperatures the devices exhibited a small increase in the zero bias conductance. This increase was magnified as the temperature was decreased further below 1.7K, but remained a relatively small fraction of the total conductance of the device as seen in Figure 3.1. This small increase in the zero bias conductance was ascribed to being the precursor of a supercurrent across the InGaAs-Niobium junction and was claimed to be the first observation of a supercurrent in a device containing just

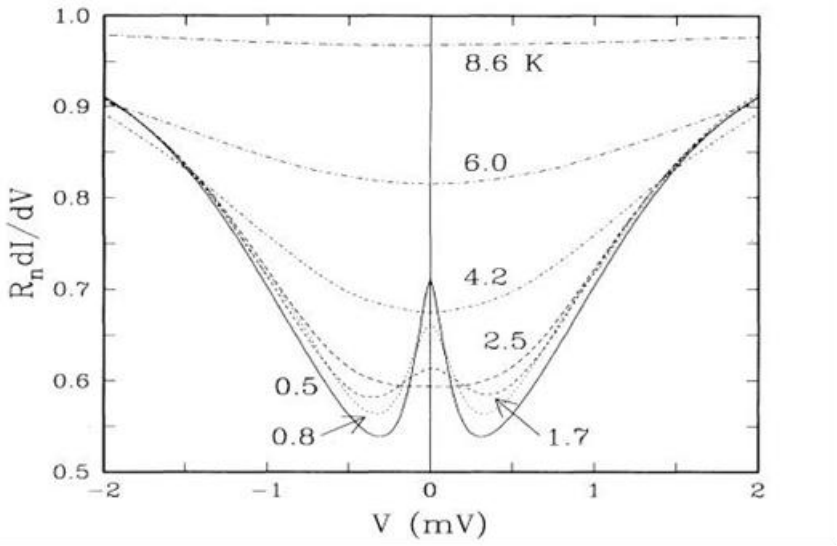

Figure 3.1: Kastalsky et al.'s [1] measurements of the normalized conductance versus voltage for their most transparent Nb-InGaAs structure. If the temperature is decreased below 2.5K the conductance at low bias exhibits a local maximum. Taken from [1].

one superconducting electrode. This small zero bias conductance peak was extremely sensitive to an applied magnetic field further supporting this hypothesis.

Other investigators also have studied superconductor-semiconductor systems, Taboryski *et al.* [19] coupled aluminum superconducting contacts to a heavily doped GaAs epitaxial structure deposited on a GaAs substrate. While this epitaxial structure and device fabrication are quite similar to the process used in this project, the results obtained are quite different. The epitaxial structure consisted of 2000 Angstroms of Aluminum grown on a heavily Si delta doped GaAs cap. The purpose of this cap is to minimize the Schottky barrier between the superconductor and the semiconductor. Beneath the cap a thick 200nm layer of doped GaAs was grown to provide a transport channel. The devices fabricated were quite similar to our thin trench device design and consisted of first defining 17 micron wide mesas, then using e-beam lithography to etch 1 micron wide trenches in the Al, and finally lifting off Ti/Au contact pads to make 4 point

measurements. The two terminal nature of their device design meant that they were also limited to a single resistance measurement that mixed G_c and R_s. Because of this limitation, they were unable to distinguish between effects caused by changes in the contact conductance across the two N-S interfaces and changes of the transport inside the semiconductor. In spite of this, they claimed that they were able to measure the junction resistance, but we point out here that their argument is not valid. They supposed that the transfer length between the semiconductor and the superconductor is just given by the normal state values of G_c and R_s. As our analysis in the appendix shows, this is clearly

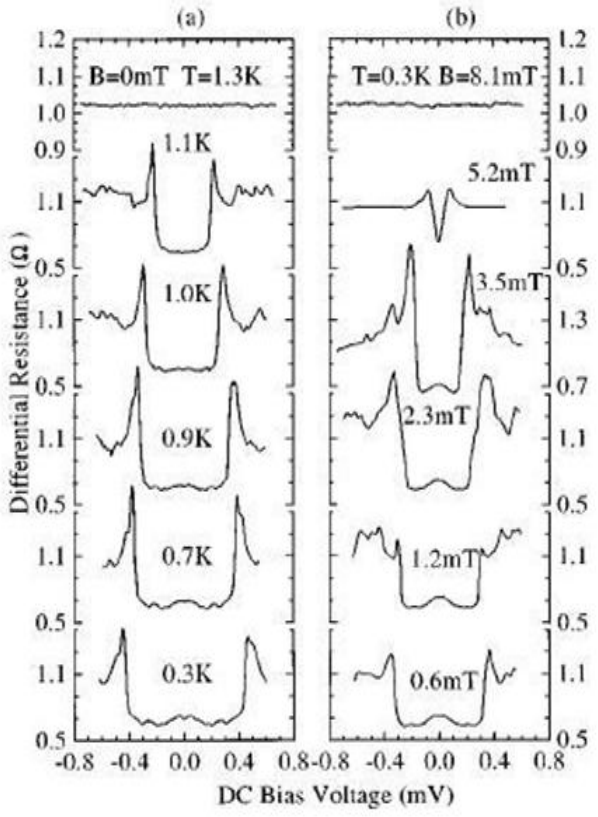

Figure 3.2: Differential resistance versus voltage curves of two-terminal Al-GaAs devices measured by Taboryski *et al.* [19]. In contrast to the work of Kastalsky [2], the resistance of the entire structure decreases immediately below T_c.

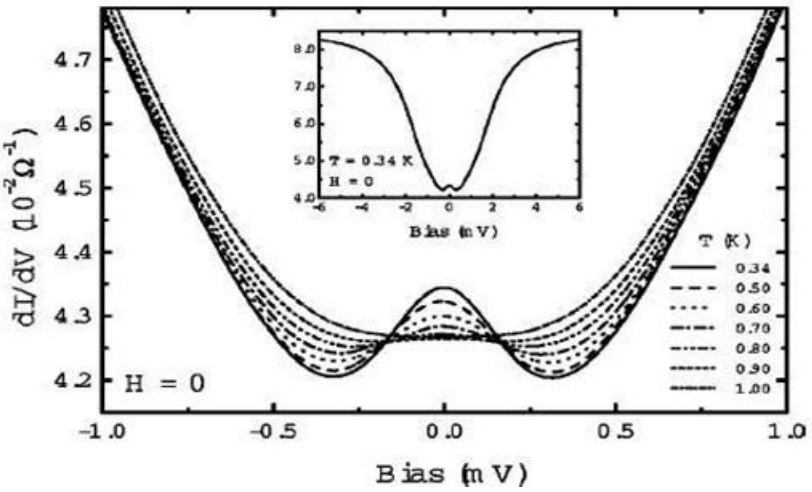

Figure 3.3: Conductance versus voltage plot for the Nb-GaAs devices fabricated by Giazotto [18]. Note the similarity to Kastalsky's results with the small peak in the differential conductance. Taken from [18].

not the case. This quantity has to be independently determined at each temperature. Basically, when the proximity effect is important, it makes a large difference to both of these quantities and claiming that the normal state values determine the transfer length is simply not true.

Figure 3.2 shows the results of Taboryski's experiments. In contrast to the data shown by Kastalsky who had to decrease his samples far below the T_c of the Nb to see an increase in the zero bias conductance, here there is an immediate increase below T_c which persists for all temperatures. However, as the temperature is lowered further a second effect begins to become apparent. In some samples a region at zero bias begins to exhibit a dip in the conductance which becomes more pronounced as the temperature continues to decrease. As Kastalsky concluded, Taboryski claimed that the zero bias peak is due to a precursor to a supercurrent. However, since their device geometry did not allow the separation of the contact conductance from any proximity induced enhancement to the normal transport inside the semiconductor, that conclusion must be questioned.

Giazotto *et al.* [18] also studied superconductor-semiconductor junctions which combined the epitaxial structure of Taboryski and the *ex situ* transferring of Kastalsky. Giazotto's epitaxial structure was very similar to that of Taboryski, in particular it contains the same delta doped GaAs cap. However, unlike Taboryski's completely *in situ* growth process, an Arsenic cap was deposited to protect the semiconducting surface while it is moved from the MBE chamber to a sputtering chamber for the deposition of the Nb superconducting layer. Devices were fabricated consisting of three 100μm x 160μm mesas connected through the thick semiconducting channel. In their devices, current was injected into the center electrode and a measurement is made on the upstream electrode to remove contributions of parasitic resistance in the semiconductor. While this electrode design is similar to the 3 terminal device structure used in our project, Giazotto did not simultaneously measure the downstream voltage. Without this information he was unable to extract both G_c and R_s. Despite the shared epitaxial structure, Giazotto's results are more similar to Kastalsky's than that of Taboryski. As can be seen in Figure 3.3, there is a small increase in the zero bias conductance, but Giazotto was forced to cool the device to 1K, far below the T_c of the Nb.

From these three results we can see that the strength of the proximity effect is not controlled by the epitaxial structure but rather by the quality of the interface between the superconductor and the semiconductor. This means that our ability to grow the entire device structure *in situ* should lead to a more intrinsic measure of the impact of the proximity effect on junction transport because for a given semiconductor, our interfaces should be as transparent as possible. All of the theoretical work on proximity effect, BTK [5], McMillan [21], Thuneberg[8] and Nazarov [2] agrees with the common sense

notion that reducing any unintended interface barrier, for example caused by oxidation of the semiconductor surface or by disorder, should lead to a stronger proximity effect.

Nguyen [20] also studied the superconductor-semiconductor system, but used InAs instead of GaAs as the semiconductor. InAs does not form a Schottky barrier to Nb, so the manifestation of the proximity effect should be enhanced relative to an equivalently doped GaAs junctions. In that work, Nguyen used a highly conductive InAs-AlSb two dimensional electron gas(2DEG) with a mobility of 81000 $cm^2/V\ s$ as the conduction channel linking the Nb electrodes. This channel was used not only to make the mean free path in the 2DEG, 2.2μm, greater than the 1-2 μm distance separating the electrodes, but also to reduce the measured resistance of the device to emphasize the junction resistance over the transport channel resistance. Though their devices were fundamentally two terminal in nature, and only a single voltage measurement was taken, Nguyen claimed from transmission line measurements that only 0.2 Ohms of the 3.2 Ohm device resistance, directly below T_c, is attributable to the conducting channel. The remaining 95 percent they claimed was due to the junction resistance. While this may be true at T_c, as in the work described above, it is fundamentally impossible to determine how both R_s and G_c are changed by the proximity effect if only a two terminal measurement is made.

An example of their data can be seen in Figure 3.4, which shows a large spike in the differential conductance at zero bias. While the enhancement is less than the maximal factor of two allowed by BTK theory, in order to obtain such a peak they argued that their N-S junctions would have to have been far more transparent than their device structure and measured normal state resistance implied. To understand their result, they proposed that the enhancement was due to multiple attempts at Andreev reflection. The very long

mean free path in the channel as compared to the depth of the well, 2.2µm versus 150nm, means that the electrons can coherently rebound off the bottom of the quantum well many times before suffering an inelastic scattering event in the InAs. Thus, they would have multiple chances to enter the condensate, greatly enhancing an otherwise small Andreev probability. This higher cumulative Andreev probability is what is evident in the measurement, masking the poorly transparent contacts. A similar model for multiple attempts at Andreev reflection was proposed by van Wees [22] that did not rely on an

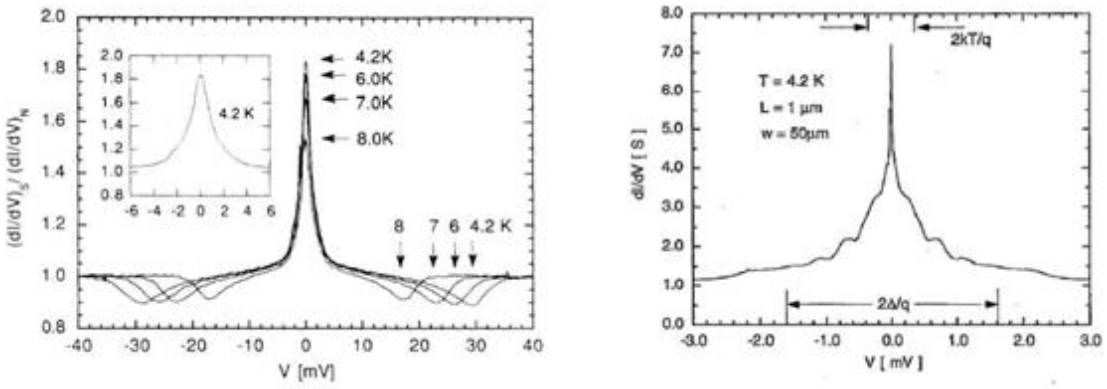

Figure 3.4: (Left) Differential conductance versus voltage for the Nb-InAs-Nb devices created by Nguyen et al. As the temperature decreases the magnitude of the conductance bias peak increases. Taken from [20]. (Right) Differential conductance of a Nb-InAs-Nb device created by Nguyen with more conductive contacts than the earlier work of Nguyen shown on left. Note that the increase in differential conductance has exceeded that of the factor of two allowed in Andreev reflection. Taken from [23].

electronic barrier for coherent reflection but predicted similar effects in diffusive conductors.

In later experiments, Nguyen [23] and Thomas [24] improved their sample preparation by sputter cleaning the surface of the InAs prior to depositing the superconducting electrodes. While this method improved the measured contact resistance

by a factor of 10 to 5×10^{-7} Ohm cm^2, the material growth was not performed completely *in situ*. Despite the improvement, the junction transparency is still quite poor. (For example, we obtained a specific contact resistance of less than 10^{-8} Ohm cm^2 by using all *in-situ* multilayer growth of InAs/niobium bilayers. We argue that the per channel transmission coefficient in our devices is nearly one, implying that in Nguyen's case it is no larger than 0.02.) For similar sized devices as in their earlier study, measurements of an even sharper peak in the zero bias conductance were observed as shown in Figure 3.4. This conductance peak grew in size as the temperature was decreased, and the enhancement exceeded the factor of two permissible by Andreev reflection implying that the N-S contacts are no longer in the weak coupling limit described in the BTK theory [5]. Additionally when the distance between the electrodes was reduced below 0.4 microns, the resistance at zero bias vanished for temperatures less than 3.9K, implying the formation of a weak link Josephson junction between the two superconducting contacts. Keeping all other experimental values constant, as the contacts became more transparent the amount of coherent coupling between the two electrodes increased to the point where a pair current between the electrodes is observed. This demonstrates the importance of contact transparency but precludes use of these samples to probe the superconductor-semiconductor junction.

3.3 Previous Experimental Work on this Project

Any discussion of previous experiments would be incomplete without the mention of Soren Flexner [4], who began the project on coupling superconductivity to III-V semiconductors here at the University of Illinois. Flexner and I developed the first

generation of the transparent cap structure, utilizing heavily delta doped graded InGaAs on a thick doped GaAs channel. The sample was transferred completely *in situ* to another MBE chamber where the Nb superconductor was deposited. The wafer was patterned into the 3 terminal device structure shown in Figure 3.5 which allows two independent measurements, V2 and V3, to be made. V2 shares superconducting electrodes with the current and measures the sum of the voltages on the downstream end of the injector finger, across the semiconducting gap separating the injector and the drain, and the voltage of the drain contact. V3 utilizes the upstream voltage contact on the right hand side of the figure. Since the current flows to the drain on the left, there is no contribution to V3 from Ohmic transport in the semiconductor. V3 measures solely the voltage of the semiconductor at the upstream edge of the injector finger. It is well known that for large electrodes connecting metals and semiconductors the injection current follows an exponentially decreasing profile with a length scale equal to the transfer length $\lambda = \sqrt{\frac{1}{G_c R_s}}$. The two parameters, G_c and R_s, are the intrinsic properties of the device that are affected by the proximity effect. All previous workers have been unable to measure them independently. Since the center injector finger is typically around 3 microns long in the direction of current flow in the semiconductor and this is comparable to the transfer length, the two voltages effectively measure the profile at different points. This knowledge, coupled with a simple model based on Ohmic conduction and fully explained in Appendix B, is used to rewrite the intrinsic quantities R_s and G_c in terms of the measured resistances, R2 and R3. With the intrinsic properties of the known, an analysis can be made regarding the effect of the superconducting proximity effect as a function of temperature on the semiconductor. Unfortunately, while the geometry shown

in Figure 3.5 did allow for two independent measurements, those measurements were not truly four point in nature at all temperatures. The lack of a true four point measurement lead to an unexpected series resistance which were not accounted for in the model. In Flexner's work, this lead to a systematic error in the quoted values of G_c and R_s. The new fully four point device structure used in the current project and shown in Figure 5.5 remedies this uncertainty and is used to make accurate measurements of G_c and R_s at all temperatures.

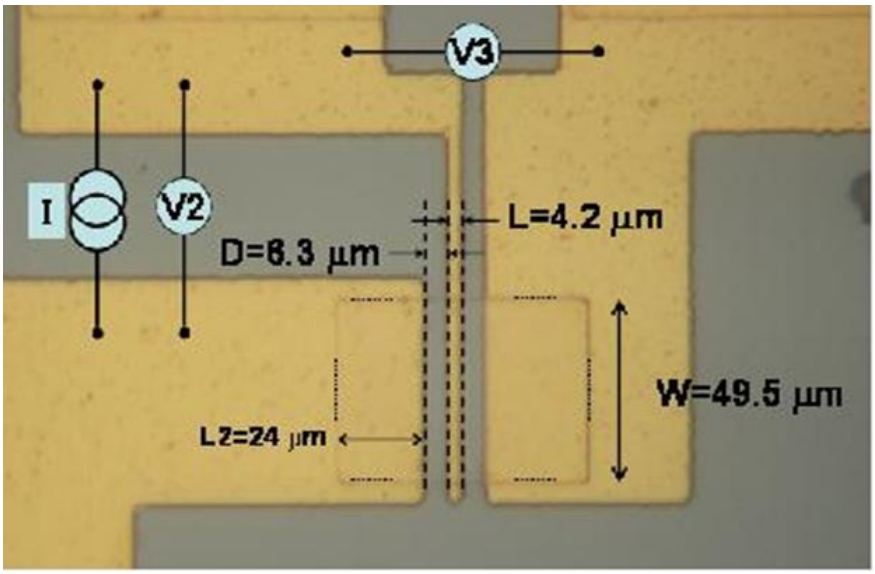

Figure 3.5: 3 terminal device used by Flexner [4] in his investigation of the proximity effect. While it does provide for 2 independent measurements, due to the shared current path and step edge the measurements are not true 4 point measurements at all temperatures.

Chapter 4 Theory of Contacts

As has been seen in the previous chapters, there is a firm theoretical and experimental basis for the prediction that the strength of the barrier at the normal-superconducting interface determines the strength of the coupling of the proximity affected region to the superconductor. While the quality of the contacts between the semiconductor and the electrodes is typically measured, quoted, and discussed in terms of either the specific contact resistance or conductance, the important quantity that controls the strength of the coupling is the transmission coefficient across the interface, $|T|^2$. While we can determine the resistance of the device trivially, $|T|^2$ depends not only on the strength of the interface barrier, but also the carrier density of the semiconductor, the materials used to make the contact, and other factors that are not easy to separate out from the measurement. Landauer created a formalism that describes the measured resistance in terms of the number of transverse quantum modes and the transmission coefficient which we can use to determine $|T|^2$. Once $|T|^2$ is established, efforts can be made to reduce the strength of the interface barrier. In this project, barriers due to Schmütz, Schottky barriers, and Fermi velocity mismatches were identified. Schmütz can be minimized by carefully crafting *in situ* growth methods, and the Schottky barrier can be reduced by creating heavily doped Indium based capping layers. These remedies will result in the transmission coefficient of the N-S interface being greatly increased for the InGaAs-Nb interfaces and almost reaching the theoretical limit for the InAs-Nb interfaces.

4.1 Landauer Method

What is the resistance of a perfect, yet normal, wire connecting two reservoirs? While naively it might be thought that the resistance would be zero, experimentally this was determined not to be the case. Landauer [25] studied this question and helped create a formalism to describe why the resistance had a limiting value. A nice discussion of this methodology is available from a book by Datta [26] which we will briefly summarize here.

In the Ohmic limit, the conductance of a 2D resistive link will be $G = \frac{\sigma W}{L}$ where σ is the conductivity and W and L are the geometric width and length of the material respectively. According to this formulation, if the length of the wire is decreased the conductance would increase without limit. However, experimentally it has been determined that once the length becomes comparable to the mean free path in the material a limiting value in the measured resistance is reached. This limit will be present even in the ideal limit where despite perfectly ballistic transport and perfectly transparent contacts an applied voltage will result in a finite current through the wire. This limiting value is called the contact conductance, which is merely the specific contact conductance times the area of the contact $G_{contact} = G_c A$. The limiting case arises from the finite number of states that exist on each side of the interface that couples the reservoir and the conductor and is not due to imperfections in the conductor. If we wish to understand the source of this excess resistance let us first assume that the contacts have perfect transmission, $|T|^2 = 1$.

Inside the conductor there exist a distinct number of energy states or transverse modes. If we then assume that the number of modes, M, does not depend on energy over the relevant range in energy, the current across a wire with differing chemical potentials, μ_1 and μ_2, at its ends is equal to [26]

$$I = \frac{2e}{h} M \frac{\mu_1 - \mu_2}{e} \Rightarrow G_c = \frac{2e^2}{h} M \ . \tag{4.1}$$

This formulation certainly shows that the resistance does not reduce to zero for perfectly ballistic materials. It instead indicates that the resistance of an ideal single moded conductor will be limited at $\frac{2e^2}{h}$ or roughly 13 kOhm. As the number of modes in the conductor increases, the result will approach the zero resistance measurement of an ideal Ohmic conductor. However, contacts of mesoscopic size are small enough that their number of modes can be small and their contact resistance can be far from the Ohmic limit.

In order to accurately determine the ideal contact conductance, we must know the number of modes in the conductor. While in principle this is a very difficult problem requiring knowledge of the confining potential and the magnetic field, according to Datta [26] in zero magnetic field this requirement can be neglected for the sufficiently wide contacts present in this project. In this case we can assume periodic boundary conditions and are in the situation depicted in Figure 4.1 where a pair of 2 dimensional conductors meets at a shared 1 dimensional boundary. In order for an electron to travel between the left hand conductor to the right hand one it must have a positive component of its x-momentum. However, its transverse or y momentum can still range between $+k_f$ to $-k_f$.

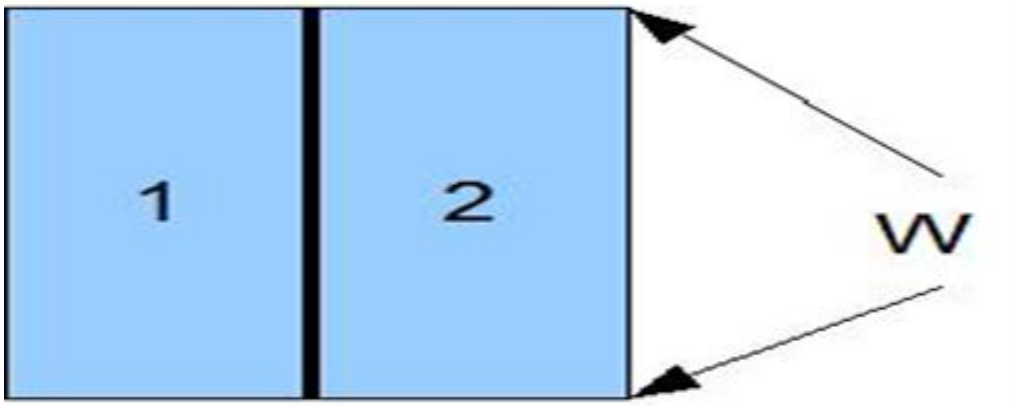

Figure 4.1: Idealized 1 dimensional contact of width W between two identical two dimensional conductors

As is usual for reciprocal space, when the physical size of the contact is W, the allowable k-states are spaced by 2π/W. Since we know the number of available k-states and their density, we can merely divide the two and arrive at the total number of available modes

$$M = Int\left[\frac{k_f W}{\pi}\right] = Int\left[\frac{W}{\lambda_f/2}\right]. \qquad (4.2)$$

In this equation, *Int* means the largest integer less than the quotient in brackets to eliminate fractional modes. While this expression is only true for a 1 dimensional contact, if you instead have a two dimensional contact of size $A = W^2$ between two bulk 3D materials the two transverse momentums, k_y and k_z, can both vary from $-k_f$ to k_f and the allowed states will be spaced by $\left(\frac{2\pi}{W}\right)^2$. Therefore the number of modes would go as

$$M = Int\left[\frac{k_f^2 A}{\pi^2}\right] = Int\left[\frac{A}{\left(\lambda_f/2\right)^2}\right]. \tag{4.3}$$

In order to find the number of modes we need to find the magnitude of the Fermi wavevector. In an electron gas this can be related to the electronic density, $k_f = 3n^{1/3}$. Therefore, we can rewrite the number of modes in terms of only measurable quantities,

$$M = Int\left[\frac{3An^{2/3}}{\pi^2}\right], \tag{4.4}$$

and can place the number of modes back into equation 4.1 which defines the contact conductance. Dividing by the area, we have found an expression for the specific contact conductance,

$$G_c = \frac{18e^2}{h} Int\left[\frac{n^{2/3}}{\pi^2}\right]|T|^2. \tag{4.5}$$

Here $|T|^2$ is the transmission coefficient. While explicitly the transmission coefficient is different for each mode, in this project we will assume that either $|T|^2$ is constant due to the uniformity of our junctions or that an appropriately averaged value can be substituted. As the transmission coefficient drops, the effectiveness of each mode also decreases and the contact conductance will correspondingly decrease as well.

Assuming a transmission coefficient of 1 allows us to establish an upper limit on the junction conductance for our devices. This case sets a metric to measure our efforts against, and by comparing our measured conductance to the ideal case we therefore can

estimate the strength of the barrier at the interface. For our typical doping of roughly $1x10^{19}$ cm^{-3}, equation 4.5 tells us that we should expect to have a contact conductance no greater than $5x10^{8}$ Scm^{-2}. For example, this means that the most transparent InGaAs cap with a measured G_c equal to $2x10^{7}$ Scm^{-2} has a transmission coefficient, $|T|^2$, equal to 0.04.

4.2 Obstacles to Transparent Contacts

The potential obstacles to having a transparent barrier at the interface are numerous, but in this project they can be grouped into 3 major themes. The presence of oxides, impurities, and any other defects at the interface will be referred to as Schmütz. This source can be minimized by following proper UHV practices and by growing the entire device structure *in situ*. The Schottky barrier is the electronic barrier native to any semiconductor-normal metal surface. Unlike Schmütz, this barrier cannot always be effectively eliminated in our system, but it can be minimized by incorporating heavily doped Indium based capping layers. Indium is used because the Schottky barrier, Φ_B, reduces linearly as a function of increasing Indium concentration. Finally, the fundamental materials issues that result in an effective barrier despite ideal contacts will be discussed, and the ideal maximum conductance for our Nb-GaAs system will be discovered. Despite what initially appears to be formidable materials issues, the maximal transmission coefficient based on these limitations is $|T|^2$ =0.92.

4.2.1 Schmütz

Many previous attempts at probing the effect of the superconducting proximity effect in a semiconductor have been confounded by the inability to grow all components of the

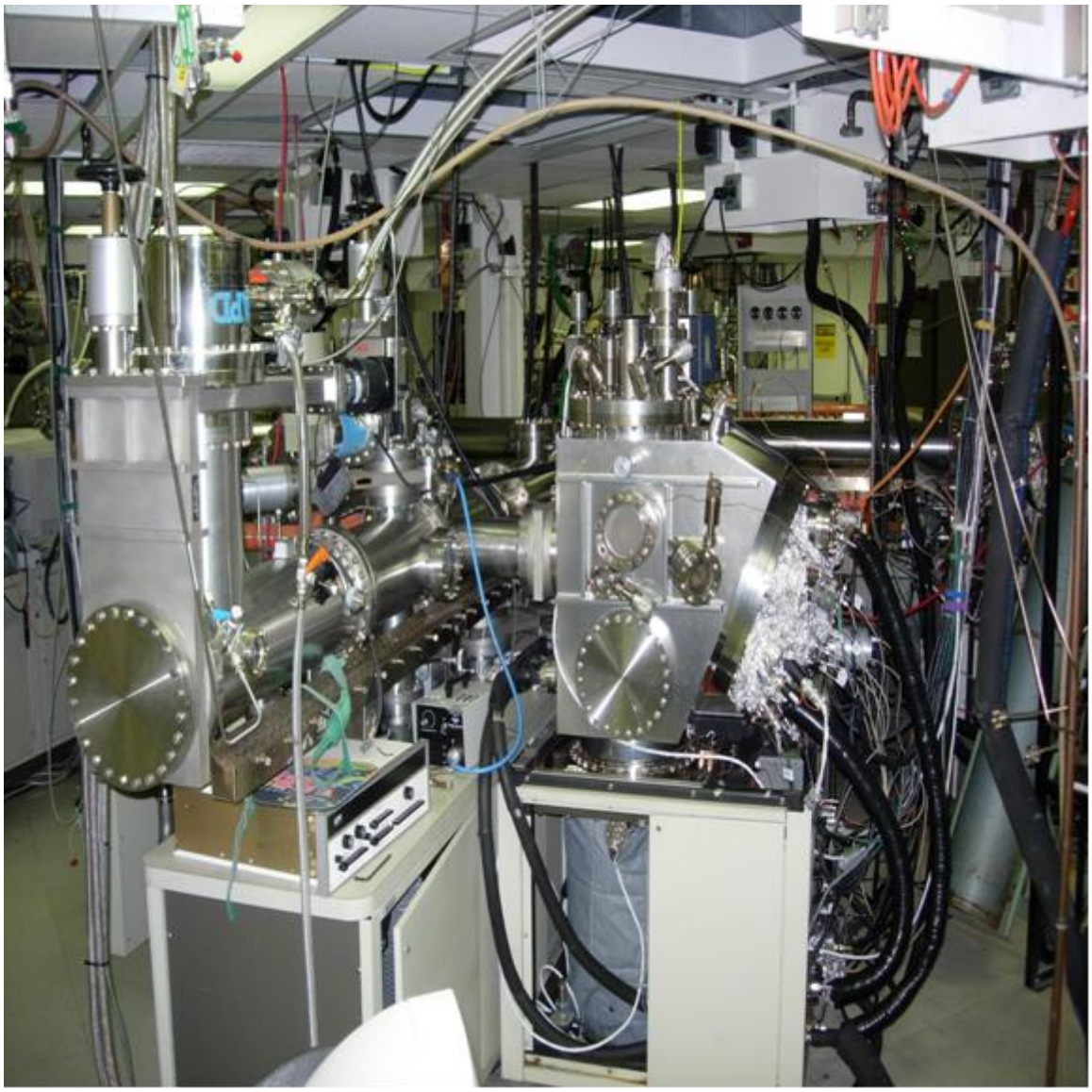

Figure 4.2: The MBE chamber that was used in this project to grow semiconducting heterostructures coupled to its associated UHV transfer tube to the left side of the picture.

structure *in situ*. The inability to do so will always introduce impurities and oxide layers at the interface. The presence of this Schmütz will greatly add to any barrier that is already present in the system, and as was seen in the discussion on the BTK theory, even small barriers reduce the probability of Andreev reflections and correspondingly reduce the coupling of superconductivity to the semiconductor. Kastalsky [1] and Giazotto [18]

both attempted to evaporate Arsenic buffer layers designed to protect the semiconducting surface during transfer to the metallization chamber. This buffer layer was then re-evaporated off the interface by raising the sample to an elevated temperature prior to the deposition of the superconductor. Nguyen [23] gently sputter cleaned the surface of the semiconductor with the intention of reducing any oxide barriers; this resulted in an increased contact conductance compared to his earlier attempts. In all cases it was reasoned that the surface would be quite clean and would not pose a problem to the formation of transparent contacts. However, our advantage is that the entire growth process can be done completely *in situ*.

Figure 4.2 shows the MBE chamber with its associated UHV transfer tube attached to it. While the importance of the cleanliness of the MBE chambers cannot be overstated, the vacuum of the transfer tube is of equal or greater importance. The UHV transfer tube allows the transfer of the completed GaAs wafer down to the Nb system without having to break ultra high vacuum. Since the pressure in the transfer tube was typically $1x10^{-9}$ torr and transfer times between chambers were 500 seconds or fewer, less than one Langmuir of gas was exposed on the N-S interface. Furthermore, the majority of the remaining gas in the transfer system is hydrogen which is not reactive with the semiconducting surface. As a result we have an exceptionally clean interface between the semiconducting and superconducting regions.

4.2.2 Schottky Barrier

If GaAs is in electrical contact with a metal, an electronic barrier known as a Schottky barrier will result. This barrier occurs due to Fermi level pinning by surface states in the

GaAs that arise from dangling bonds. They reside midgap in GaAs and pin the Fermi energy at or near the center of the bandgap. As the Fermi levels must align in equilibrium, this mismatch will require the bands to bend. The band bending requires an electric field, which in turn is terminated by the free electrons inside the semiconductor. The resulting depletion region is insulating and electrons will have to tunnel through it. Though the size of this barrier is unique to each pair of materials and is difficult to predict via theory, it is simple to measure experimentally, and Schottky barriers have been tabulated for a wide variety of systems. For the system in this project, Niobium coupled to GaAs, the Schottky barrier will be 0.7 Volts. Given this voltage at the interface we can compute the depletion region by using Poisson's equation,

$$\frac{\partial^2 V}{\partial x^2} = \frac{\rho}{\varepsilon_r \varepsilon_0}, \tag{4.6}$$

where ρ is the electronic density in the semiconductor. In the case where the electronic density is homogeneous, we can easily integrate both sides and find that

$$\Phi_B = \frac{ned^2}{2\varepsilon_r \varepsilon_0}. \tag{4.7}$$

Φ_B is the Schottky barrier voltage and *n* is the number density of electronic charge. Rearranging, we find the depth of the depletion region

$$d = \sqrt{\frac{2\Phi_B \varepsilon_r \varepsilon_0}{ne}}. \tag{4.8}$$

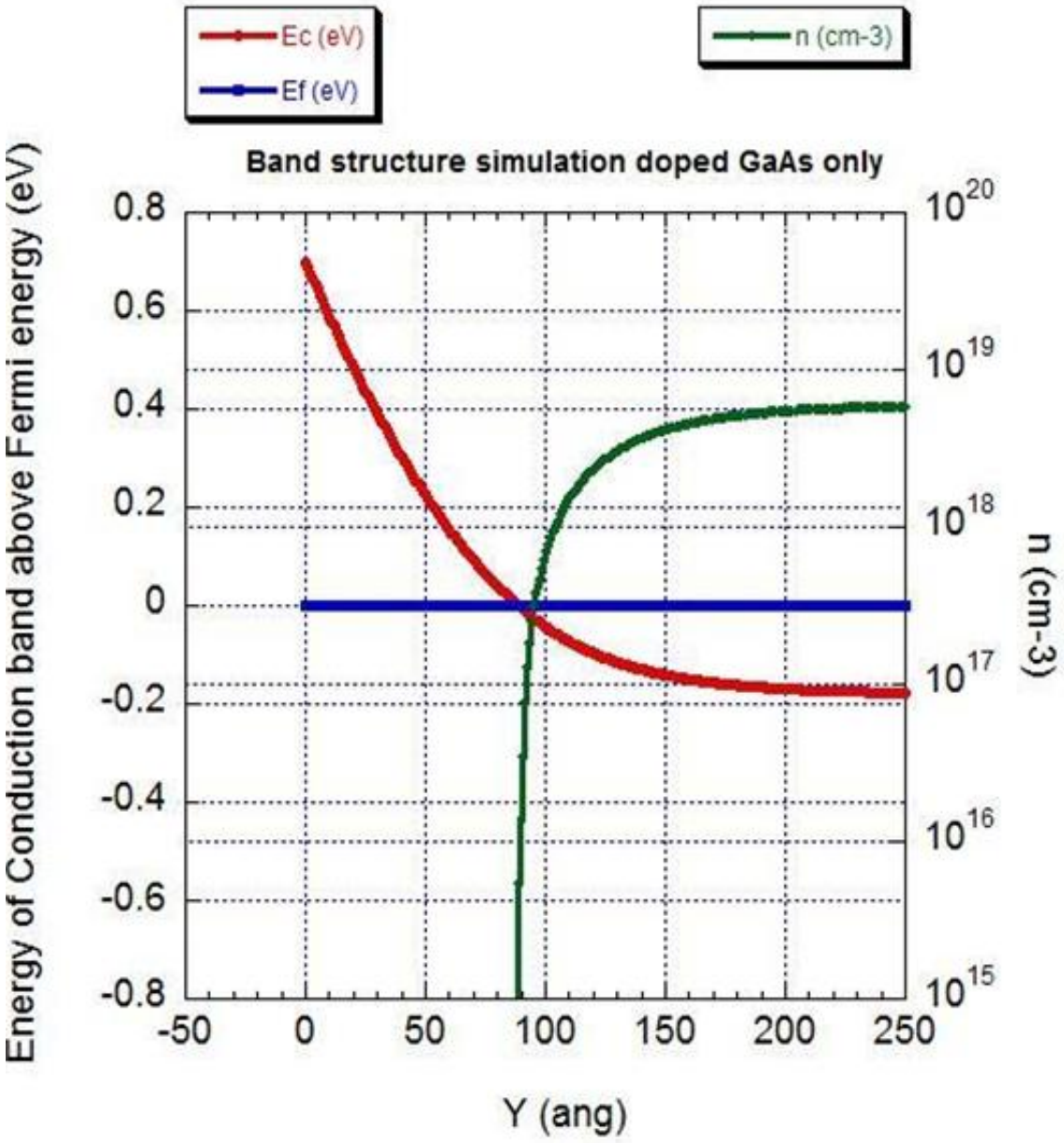

Figure 4.3: Without the InGaAs cap, a very large Schottky Barrier develops at the surface of the semiconductor. The conduction band (red) is pinned at 0.7V above the Fermi level at the N-S interface on the left had side. Whenever the conduction band is above the Fermi level the GaAs is insulating. This is represented by the carrier density (green) rapidly going to zero. Simulation courtesy of Snider [27].

If we plug in values of the charge density corresponding to the amphoteric limit of Si in GaAs, 6×10^{18} cm^{-3}, we find that there exists a depletion depth of 90 Angstroms in the semiconductor. While this result will tell us the depth of the depletion region, the

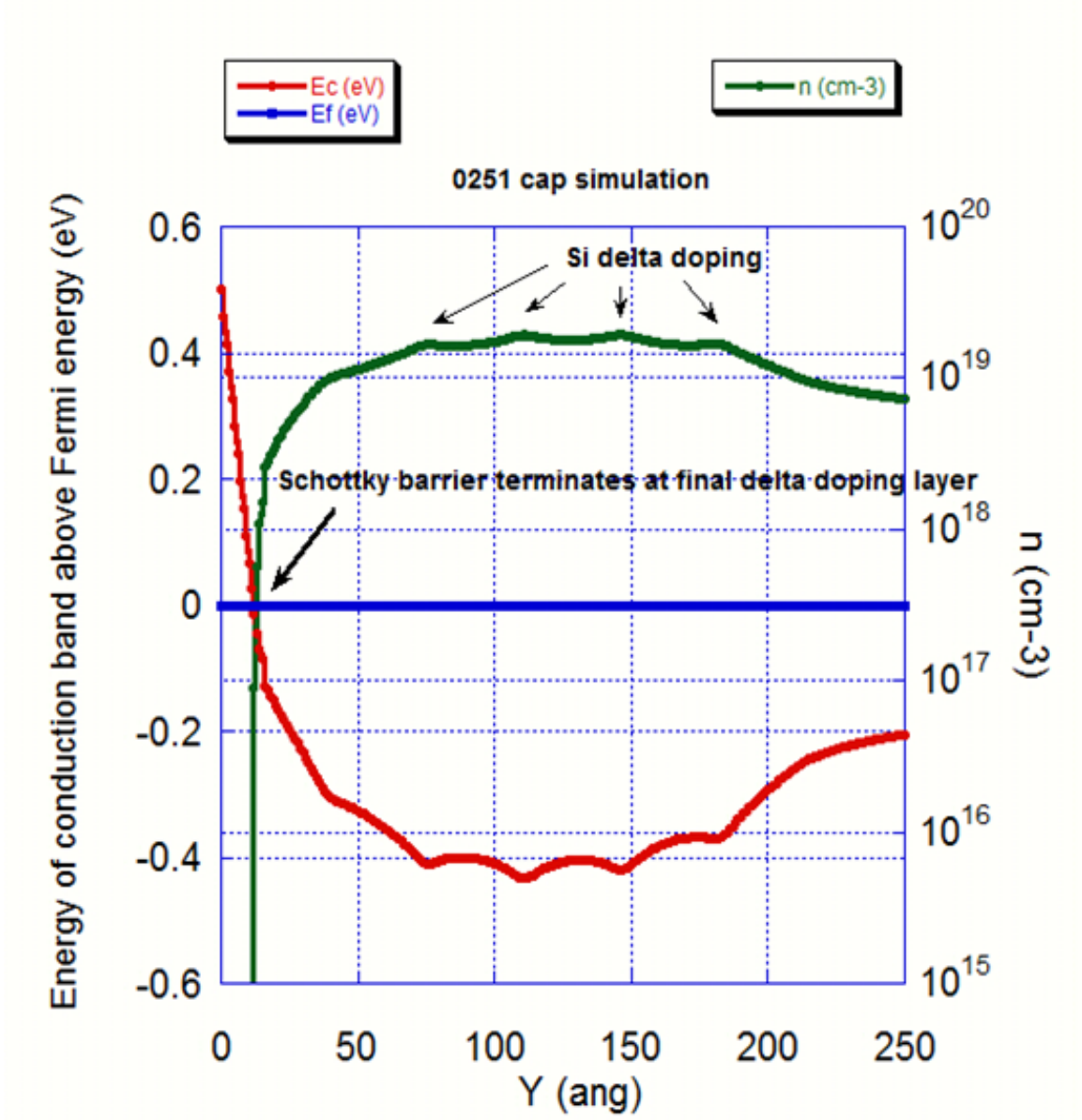

Figure 4.4: Band structure simulation of the highest transmission InGaAs cap, note the decrease in height and depth of the Schottky barrier from the doped GaAs heterostructure in Figure 4.3. Simulation courtesy of Snider [27].

transparency of the barrier will depend upon the actual conduction band profile inside the semiconductor. Fortunately the conduction band profile can be solved numerically by using a finite element Poisson solver courtesy of Dr. Snider at Notre Dame [27]. Figure 4.3 represents both the conduction band and the density of electrons as a function of depth for GaAs doped at 6×10^{18} cm^{-3} coupled to Nb. The depletion depth is 90 Angstroms,

but the numerical solution also allows us to see the shape of the conduction band and use its value to compute the transmission coefficient through the depletion region. Using the WKB approximation for a barrier of this size and shape, the transmission coefficient will be $1x10^{-8}$ corresponding to a Z value of 10000, a barrier far too opaque for Andreev reflection. In reality the transmission coefficient will be somewhat higher due to any imperfections in the barrier having a dominating effect on the transport, but clearly doped GaAs is insufficient to create properly transparent contacts.

If we wish to reduce the effect of the Schottky barrier, we must reduce its height or width. The height can be reduced by alloying Indium into the GaAs. InAs does not form a Schottky barrier to Niobium, and the alloy InGaAs has a barrier height that linearly reduces with In concentration. Unfortunately, InAs and InGaAs have a lattice mismatch with the GaAs, and cannot be grown on GaAs without strain. As will be discussed in section 5.1.2, the greatest percentage of InAs that can be alloyed with the GaAs in our devices is 30 percent. This In concentration reduces the value of the Schottky barrier to about 0.5 Volts. While this decrease might not seem to have much of an effect, since it enters exponentially into the transmission expression it will greatly decrease the strength of the barrier. In order to reduce the depth of the barrier the doping must be increased. As the bulk doping is already at the amphoteric limit, delta doping must be employed. Instead of uniformly doping throughout the semiconductor, delta doping is created by restricting the Si ionic cores to narrow regions in depth, ideally a single monolayer. Returning to Poisson's equation, in order to completely cancel a Schottky barrier of height Φ_B at a particular depth d a sheet density of

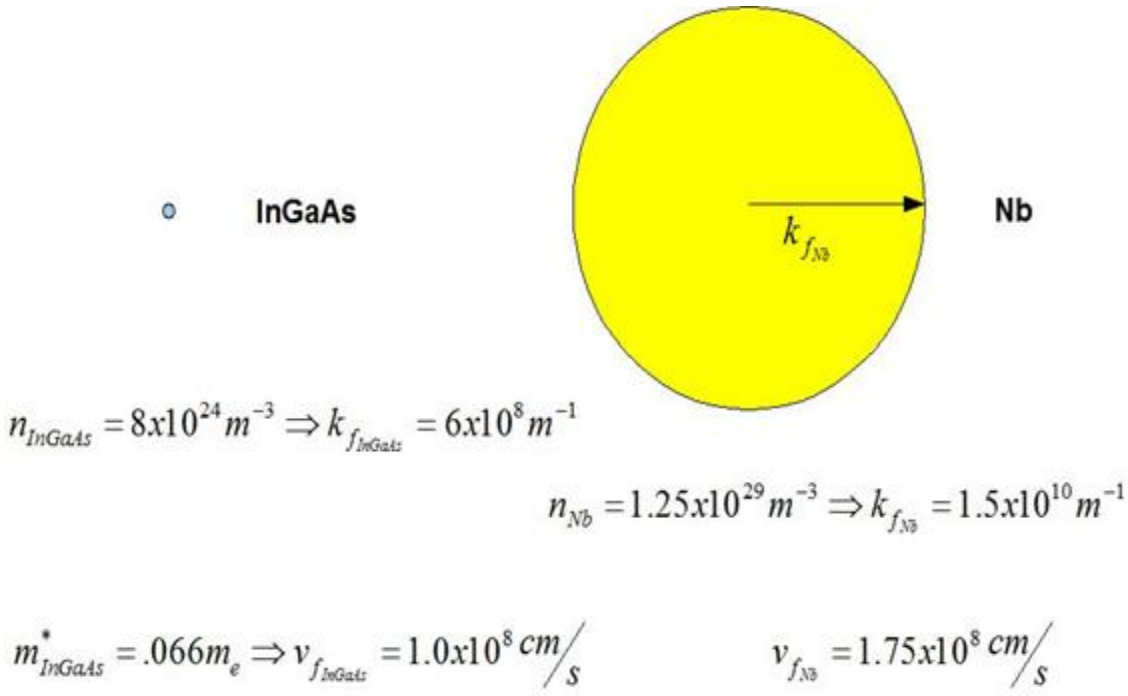

Figure 4.5: Scale drawing of relative sizes of the Fermi surfaces of the InGaAs cap and Nb used in this project. The larger electronic density in the Nb results in the Fermi sphere being 25 times larger in diameter than the InGaAs.

$$n_s = \frac{\Phi_B \varepsilon_r \varepsilon_0}{de} \tag{4.9}$$

is required. Figure 4.4 shows the simulation of the band structure using the the highest transmission coefficient InGaAs cap described in section 5.1.2. The height of the Schottky barrier has been reduced to 0.5V and the depth has dropped from 90 Angstroms to just 11 Angstroms. Unfortunately 11 Angstroms is the minimum depth that can be achieved using this method, as higher doping at a shallower depth destroys the epitaxy and has a negative net effect on the interface transparency. If the WKB approach is used on this band structure the expected transmission coefficient has now been increased to .04. While this still represents a Z of 5, limiting the likelihood of Andreev reflections, $|T|^2$ is far greater than an interface composed of just bulk doped GaAs.

4.2.3 N-S Impedance Mismatch

Even if all of the previously discussed barriers are eliminated, there will still be an effective barrier at the interface. This effective barrier is due to an impedance mismatch, caused by differences in the intrinsic materials parameters. Just as a pane of glass, no matter how clean, will have a finite reflection due to the mismatches in the index of refraction, various materials parameters in the Nb-GaAs system will have an equivalent effect due mismatches in the Fermi velocity. However, at first glance it is not immediately obvious which of the material's parameters will be the most important in determining the strength of the barrier at the interface. If we consider the system we have at hand, the potential for minimizing an effective barrier seems daunting. Figure 4.5 shows a representation of the different Fermi surfaces. As one might expect, the difference in doping between a metal and a semiconductor, no matter how heavily doped, is large. The extremely heavily doped semiconducting material only has a charge density of $8x10^{24}$ m^{-3} while bulk Niobium has a density of more than $1.2x10^{29}$ m^{-3} [28]. This disparity is reduced since the Fermi wavevector is related to the cube root of the electronic density, $k_f = 3n^{1/3}$, though as the figure attests, the wavevectors differing by a factor of 25 causes a large difference in the size of Fermi spheres. The one other transport quantity that could be involved is the Fermi velocity. Fortunately while the effective mass of electrons in Niobium is essentially the bare mass, in GaAs it is $.066m_e$. This means that the Fermi velocities will be very comparable, differing by less than a factor of two with $v_{f_{Nb}} = 1.75x10^8$ cm/s and $v_{f_{GaAs}} = 1.0x10^8$ cm/s. This ratio of near unity is quite remarkable given that the charge densities differ by practically a factor of 2000.

However, which of these is the appropriate quantity to compare in order to understand how to parameterize an effective barrier? In order to determine how to quantify the effect of the material on the barrier let us consider the situation in Figure 4.6. A pair of three dimensional materials with differing Fermi surfaces and effective masses are connected at a two dimensional interface with a generalized barrier consisting of a delta function with strength α. The wave functions of the two materials are

$$\Psi_1 = Ae^{i\left[k_f \cos\theta_1 x + k_f \sin\theta_1 y\right]} + Be^{i\left[-k_f \cos\theta_1 x + k_f \sin\theta_1 y\right]}, \tag{4.10}$$

and

$$\Psi_2 = Ce^{i\left[q_f \cos\theta_2 x + q_f \sin\theta_2 y\right]}. \tag{4.11}$$

Schematically these wave functions consist of three parts, the incident wave with amplitude A, the reflected wave with amplitude B, and the transmitted wave with amplitude C. As usual, the two boundary conditions are that Ψ(0) is continuous implying

$$A + B = C, \tag{4.12}$$

and the discontinuity in the derivative at a delta function

$$\Delta \frac{\partial \Psi}{\partial x}(0) = \alpha \Psi(0). \tag{4.13}$$

These boundary conditions imply that

$$-\frac{\hbar^2}{2m_1}\left[-Aik_f \cos\theta_1 + Bik_f \cos\theta_1\right] + \frac{-\hbar^2}{2m_2} Ciq_f \cos\theta_2 = \alpha(A + B). \tag{4.14}$$

Using equations 4.12 and 4.14 it can then be shown that

$$B = \begin{bmatrix} \dfrac{iq_f \cos\theta_2}{m_2} - \dfrac{ik_f \cos\theta_1}{m_1} + \dfrac{2\alpha}{\hbar^2} \\ \hline -\dfrac{ik_f \cos\theta_1}{m_1} - \dfrac{iq_f \cos\theta_2}{m_2} - \dfrac{2\alpha}{\hbar^2} \end{bmatrix} A, \tag{4.15}$$

and that

$$C = \frac{2m_2}{iq_f \cos\theta_2} \begin{bmatrix} \dfrac{k_f q_f \cos\theta_1 \cos\theta_2}{m_1 m_2} \\ \hline -\dfrac{ik_f \cos\theta_1}{m_1} - \dfrac{iq_f \cos\theta_2}{m_2} - \dfrac{2\alpha}{\hbar^2} \end{bmatrix} A. \tag{4.16}$$

As usual the relevant probabilities of reflection and transmission can be found taking the ratio of these coefficients and are

$$|R|^2 = \frac{|B|^2}{|A|^2} = \frac{\left(\dfrac{k_f \cos\theta_1}{m_1} - \dfrac{q_f \cos\theta_2}{m_2}\right)^2 + \dfrac{4\alpha^2}{\hbar^4}}{\left(\dfrac{k_f \cos\theta_1}{m_1} + \dfrac{q_f \cos\theta_2}{m_2}\right)^2 + \dfrac{4\alpha^2}{\hbar^4}}, \tag{4.17}$$

and

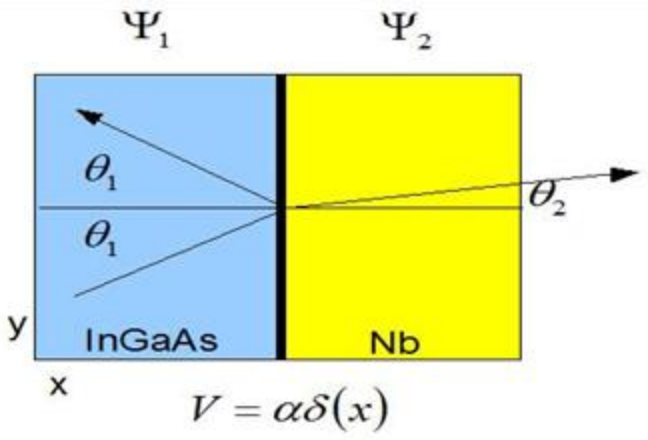

Figure 4.6: Diagram depicting the generalized transmission situation.

$$|T|^2 = \frac{|C|^2}{|A|^2} = \frac{\dfrac{4k_f^2 \cos^2\theta_1}{m_1^2}}{\left(\dfrac{k_f \cos\theta_1}{m_1} + \dfrac{q_f \cos\theta_2}{m_2}\right)^2 + \dfrac{4\alpha^2}{\hbar^4}}. \tag{4.18}$$

Notice that in each case if a Fermi wavevector appears it is always divided by the appropriate effective mass. This implies that these probabilities can be rewritten as a function of the Fermi velocities, $v_f = \dfrac{\hbar k_f}{m}$, and are

$$|T|^2 = \frac{4v_1^2 \cos^2\theta_1}{\left(v_1 \cos\theta_1 + v_2 \cos\theta_2\right)^2 + \dfrac{4\alpha^2}{\hbar^2}}, \tag{4.19}$$

and

$$|R|^2 = \frac{\left(v_1 \cos\theta_1 - v_2 \cos\theta_2\right)^2 + \dfrac{4\alpha^2}{\hbar^2}}{\left(v_1 \cos\theta_1 + v_2 \cos\theta_2\right)^2 + \dfrac{4\alpha^2}{\hbar^2}}. \tag{4.20}$$

Due to current continuity, we are under the requirement that flux must be conserved instead of number density. This requirement implies that the reflection and transmission coefficients must be multiplied by the ratio of the velocities in their incoming and outgoing cases. While the reflected wave remains on the left side of the interface and its velocity will remain unchanged, since the transmitted wave is changing velocities the correct transmission coefficient will be

$$|T_{flux}|^2 = \frac{v_2}{v_1}|T|^2 = \frac{4v_1 v_2 \cos^2\theta_1}{\left(v_1 \cos\theta_1 + v_2 \cos\theta_2\right)^2 + \dfrac{4\alpha^2}{\hbar^2}}. \tag{4.21}$$

This expression tells us that the only material dependent property of the zero-barrier transmission coefficient is the Fermi velocity. If we are interested in determining the maximal transmission coefficient for Nb and GaAs, we should consider this case with no barrier. To further simplify we can also use the reduction shown in Blonder [29] where the incident angle is zero. Using this simplification the transmission coefficient is equal to

$$|T|^2 = \frac{4v_1v_2}{(v_1+v_2)^2}. \tag{4.22}$$

Using the substitution of $r = \frac{v_1}{v_2}$ this can further be rewritten as

$$|T|^2 = \frac{1}{1+\frac{(1-r)^2}{4r}}. \tag{4.23}$$

This equation implies that an effective barrier of size $\frac{(1-r)^2}{4r}$ exists even with perfect contacts. Entering the values of the Fermi velocities for Niobium, 1.75x10^8 cm/s and GaAs, 1.0x10^8 cm/s, the largest possible transmission coefficient that can be created between these materials is 0.92. In the language of BTK, this interface would have a Z of 0.29. This is still a non-zero barrier, but it is one which will have a high probability of Andreev reflection. We will see later that our highly transparent InAs-Nb interfaces have a $|T|^2 = 0.73$, very close to this theoretical limit.

Chapter 5 Experimental Procedures

In order to experimentally probe the proximity effect, samples need to be grown and processed into testable devices. The conclusions of the previous chapters have been integrated into our sample growth and device design in order to increase our ability to induce and measure pair correlations in the semiconductor. After a fresh substrate has been loaded and placed into a fully prepared chamber, a series of initial procedures are performed to make the surface as smooth as possible. These procedures have been empirically shown to maximize the growth quality. Once the surface has been suitably prepared, the substrate is ready for the device section of the semiconducting growth to begin. The device section is composed of a conduction channel and, when GaAs is used, a capping layer to increase the transparency of the N-S interface. The conduction channel is designed to aid the conduction between the superconducting electrodes and to ensure that the measured device resistance is not dominated by the resistance of the semiconducting transport. It can take the form of a doped diffusive GaAs layer ranging in size from 0 to 4000 Angstroms thick, or a thick InAs film. The capping layer is designed to minimize the native Nb-GaAs Schottky barrier at the interface and consists of heavily delta doped graded InGaAs. After the semiconducting portion of the growth is completed, the wafer is allowed to cool and is then transferred along the UHV transfer tube to a separate MBE chamber where polycrystalline Nb is deposited. The wafer is then removed and processed using standard photolithography techniques into three terminal and two terminal devices structures.

The process to go from a blank GaAs substrate to a completed device requires a combination of persistence and precision that is based upon decades of research and engineering. Since the growth and processing of III-V semiconductors is a mature field, this general knowledge is well known and can be found in a number of books [30, 31, 32] and review articles [33, 34]. Despite having this large general knowledge base, every experimental system is different and has its own unique quirks. While these quirks are interesting and understanding them is necessary to create the Nb-GaAs experimental system, they do not directly relate to the issue of how to increase the number of pair correlations in the semiconductor and as such are located in Appendix A.

5.1 Device Film Growth

A fresh wafer is cleaned and placed into the vacuum system. Subsequently, a considerable amount of outgassing and other procedures designed to maximize the cleanliness of the chamber and flatness of the substrate are performed. Once these have been completed and the surface is suitably flat, the actual device portion of the growth could begin. The devices took a variety of different forms, but typically fell into two broad categories: diffusive Si:GaAs films with InGaAs caps, and diffusive InAs films. Each of these shared the same initial growth preparation, disclosed in Appendix A, but the different structures now begin to diverge at this point in the growth process.

5.1.1 Diffusive GaAs

The simplest of the two device structures is simply a diffusive layer of Si doped GaAs ranging from 200 to 4000 Angstroms in thickness. These films were electron doped at a

level that varied from $1x10^{18}$ cm^{-3} to as much as the $6x10^{18}$ cm^{-3} amphoteric limit. In order to achieve higher doping levels, the flux and hence the temperature of the Si source had to be increased. However, it was noted experimentally that Si furnace temperatures in excess of 1250C resulted in decreased epitaxy of the Si:GaAs films. The reduced epitaxy is due to the very high radiative heating from the Si source causing the temperature of the surface of the GaAs to be higher than expected. This adversely adjusted the effective III-V flux ratio and scorched the surface. The upper limit on the furnace temperature gave a maximum value for the Si flux of roughly $6x10^{10}$ cm^{-2} s^{-1} and meant that the growth rate for the heaviest doped GaAs could not exceed 1 Angstrom per second. The presence of the Silicon atoms decreased the long range order in the semiconductor and degraded the RHEED oscillations as compared to the undoped GaAs, but oscillations would still persist for growths segments exceeding 200 Angstroms between anneals implying a high quality layer by layer epitaxial growth mode. The mean free path of these films is roughly 500 Angstroms.

5.1.2 InGaAs Cap

As was discussed in section 4.2.2, GaAs forms a Schottky barrier with Nb of height 0.7V. This barrier is a significant impediment to conduction across the N-S interface, and in order to create transparent interfaces it is vital that the barrier be minimized. The effectiveness of this barrier will be reduced in two ways. First, as InAs does not form a Schottky barrier to Niobium it will be graded into the semiconducting structure in order to reduce the height of the barrier. Secondly, delta doping will be employed to add additional carriers to the region near the interface causing the depth of the barrier to be

reduced. While the addition of InAs reduces the height of the Schottky barrier it also introduces a number of potential difficulties. First, in order to be effectively employed the temperature of the substrate must be reduced to 450C. As shown in Figure A.1, the vapor pressure of In is too high at the earlier growth temperature of 600 C. At this elevated temperature not only will there be a significant probability that the Indium re-evaporates prior to being incorporated into the lattice, but there will be significant amounts of Indium decomposing out of the InGaAs lattice during the delta doping [38]. Operating at this reduced temperature unfortunately means that RHEED oscillations become difficult to utilize due to the reduced surface mobility, but diffraction patterns can still be observed to monitor the quality of the epitaxy.

Further complicating matters is the large mismatch in lattice constants between GaAs, 5.65 Angstroms, and InAs, 6.18 Angstroms. The large mismatch implies that the ideal scenario, a thin cap of InAs directly on the GaAs heterostructure, is unfeasible. The surface will immediately fracture and all epitaxy would be lost. While the very first monolayer will bond to the underlying surface, strain will rapidly build and above 1.6 monolayers the surface will completely fracture [39]. When this experiment was attempted, the fractured surface greatly reduced the N-S junction conductance and increased the normal state sheet resistance of the semiconducting layer. In order to reduce the strain, the InAs is graded in forming the ternary alloy InGaAs as shown in Figure 5.1. The InGaAs-Nb interface exhibits a reduced Schottky barrier that is roughly linear in the percentage of Indium. Each 11 monolayer section has its In concentration increased by 5 percent. Although grading in the In reduces the strain and number of dislocations, the large amount of lattice mismatch restricts the maximum Indium concentration from

exceeding 30 percent. Above this level, RHEED showed that the two dimensionality decreases substantially. The sub order streaks vanish, and the streaks that remain transform into three dimensional spots demonstrating that the surface has broken under the strain. An upper limit of 30 percent substitution of Indium only reduces the Schottky barrier to 0.5V in height, but it will have a substantial improvement due to the

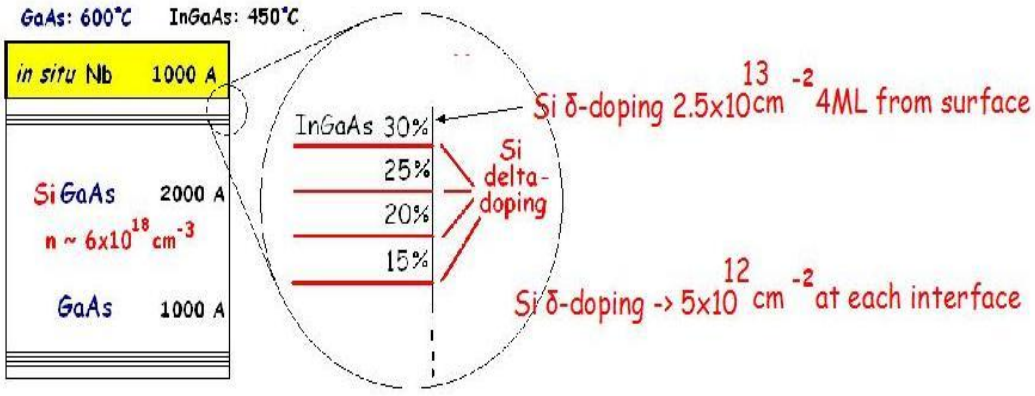

Figure 5.1: Diagram of the highly transparent InGaAs cap structure used in this project. Each segment of the InGaAs grading consists of a layer 11 monolayers thick ≈ 28 Angstroms.

transmission coefficient depending exponentially on the barrier height.

Next, in order to reduce the thickness of the barrier, the film needs to be heavily doped. As the amphoteric nature of Si in GaAs begins to activate for densities above $6x10^{18}$ cm^{-3}, this requires delta doping in the semiconductor. As discussed in the previous section, delta doping is just the restriction of the doping atoms to single layer in the semiconductor. Functionally delta doping is accomplished by leaving the Arsenic and Silicon shutters open for a fixed period of time with the Gallium and Indium shutters closed. Delta doping allows doping levels to be attained that would require Si furnace temperatures far above what could safely be achieved. It also restricts the ionic core

impurities to thin sheets in the semiconductor, since while Si atoms diffuse tens of Angstroms at 640C [40], they are much more confined at the cap growth temperature of 450C. Confining the ionic cores leads to a higher normal state conductance and mobility. After much optimization, it was found that $|T|^2$ was optimized by having two types of delta doping, the doping at the InGaAs segment boundaries of 5.4×10^{12} cm^{-2} which contributes to the background intentional doping of the cap, and the final delta doping layer that is designed to completely cancel the Schottky barrier. As was discussed in Section 4.2.2, by solving Poisson's equation we can define a sheet charge density that will completely cancel the Schottky barrier Φ_B at a particular depth *d*,

$$n_s = \frac{\Phi_B \varepsilon_r \varepsilon_0}{d}. \tag{5.1}$$

The closer this final delta doping layer is made to the surface, the thinner the barrier will be and hence the higher the transmission coefficient. However, since the required sheet density diverges as the depth is reduced; at small enough depths the necessary number of Si atoms exceeds a critical density. Beyond this value, the surface epitaxy breaks as soon as the Indium and Gallium shutters are opened. After many samples it was experimentally determined that the highest junction conductance occurred when the final delta doping layer was four monolayers beneath the surface. A simulation of the band structure for this growth can be seen in Figure 5.2. The Schottky barrier terminates on the final delta doping layer and the depth of the barrier has been reduced to 11 Angstroms.

While Figure 5.2 represents a simulation and as expected yields the self consistent answer we sought, this band structure has been confirmed by Hall measurements. If just this heavily doped cap is grown on an undoped substrate, a Hall measurement of the

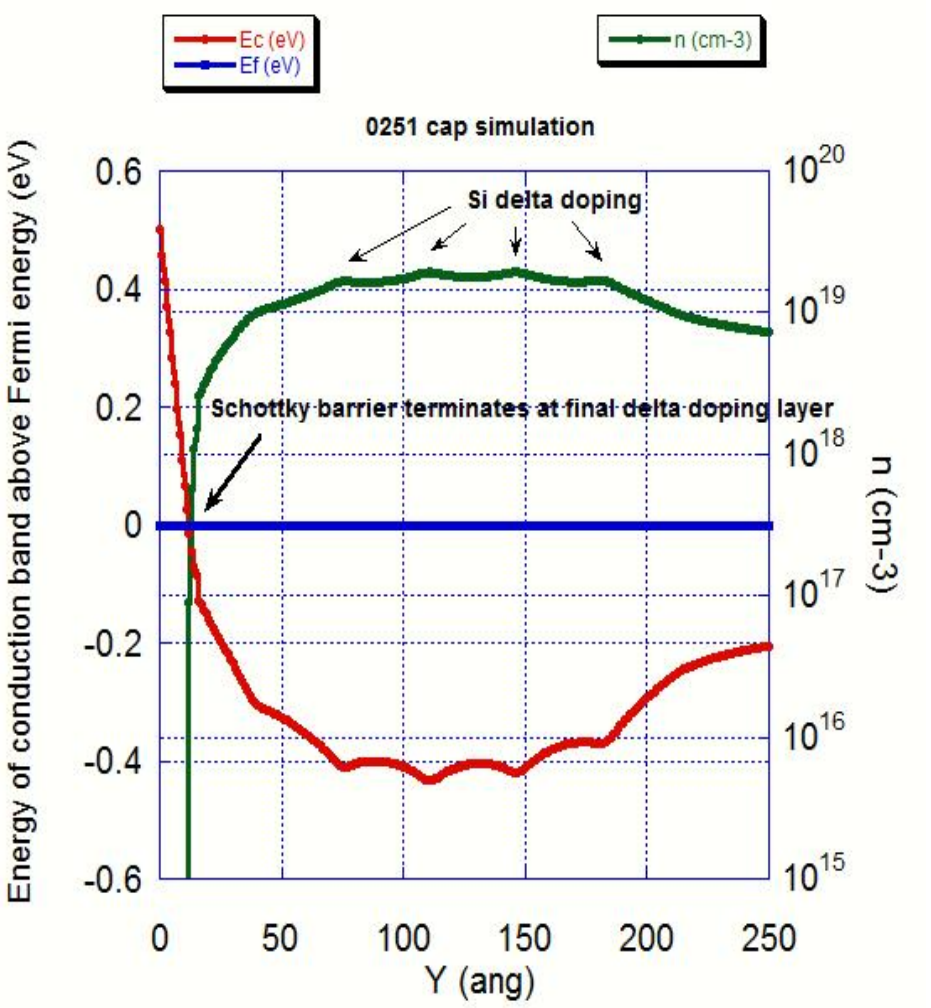

Figure 5.2: Band structure simulation of the interface region of the highest transparency InGaAs cap. The red curve represents the conduction band in the semiconductor, and the green curve is the electronic density of free carriers. Note the placement of the small delta doping layers at the InGaAs segment boundaries and that the large delta doping layer terminates the Schottky barrier 11 Angstroms from the N-S interface. Band structure simulation courtesy of Snider [27].

number of carriers yields an answer that is greater than 95 percent of the donors placed beneath the heavily doped cap. This implies that the final delta doping layer and only the final delta doping layer is sufficient to terminate the Schottky barrier.

5.1.3 Indium Arsenide

In contrast to the InGaAs based interfaces, we can also grow films that are solely InAs. These films do not form Schottky barriers to the Niobium, but unfortunately with the materials on hand we can only grow diffusive structures. Since large InAs buffer layer must be grown to smooth out the surface of an InAs film grown on GaAs, an InAs interface cannot be used in close proximity to any 5.65 Angstrom based semiconducting structure. This mismatch means that despite its high transparency InAs cannot be used in conjunction with any efforts to couple superconductivity with quantum hall edge states in the GaAs/AlGaAs heterostructures. Despite these difficulties, InAs-Nb contacts provide access to extremely transparent contacts that approach the theoretical limit. It will be seen later that the transmission coefficient of our best films are $|T|^2=0.73$, almost the upper limit of $|T|^2=0.92$ set by the Fermi velocity mismatch between Nb and InAs..

The substrates are prepared identically as in the earlier cases, and are cooled to 450 degrees Celsius for the deposition of the InAs. While the technique of reducing strain and maintaining surface epitaxy by grading in the In worked for the 30 percent substitution used in the InGaAs caps, this method cannot be extended to growing fully 100 percent InAs. Strain builds in the lattice and eventually dislocations begin to form. Once formed, these dislocations can only be healed through growing a substantial amount of material. Over distance the dislocations either annihilate each other or turn 90 degrees and confine themselves within a particular growth plane. While grading in the Indium still aids the epitaxy [41], the growth mode of the InAs will be completely three dimensional after the end of the graded InGaAs section. As it is undesirable to have excess amounts of disorder at the interface, these samples require several thousand

Angstroms of InAs to be grown prior to the surface becoming sufficiently two dimensional for the conducting channel to be grown. Fortunately we can observe the flatness of the surface improve in real time using the RHEED analysis system. Once sub-order RHEED patterns have been observed and it has been determined that the surface is sufficiently flat, the actual doped section of the sample can be grown. The amphoteric limit of InAs is lower, roughly $2x10^{18}$ cm^{-3}, but otherwise the transport of these doped diffusive InAs films will be identical to the doped diffusive GaAs films and experimentally the only difference will be the transmission coefficient to the Nb.

One other difference to take note of in InAs is the higher number of unintentional dopants. While high quality GaAs films have unintentional doping ranges of less than $1x10^{15}$ cm^{-3}, InAs is limited to the low $1x10^{17}$ cm^{-3} range. While the inability to create semi-insulating layers complicates device processing, since the InAs is grown on an undoped GaAs substrate device isolation is still possible.

5.2 Niobium

After the semiconductor section of the growth is complete, the sample is allowed to cool slightly, is removed from the As beam, and is transferred out of the semiconductor growth chamber. It is then sent through the UHV transfer tube to the Niobium system. Since the typical pressure in the tube is in the range of $1x10^{-9}$ Torr, this low pressure coupled with a transferring time of 500 seconds implies that less than 1 Langmuir of gas exposure is incident on the sample. Furthermore since the majority of the gas species remaining in the tube are hydrogen and helium which do not react with the

semiconductor, the sample surface remains extremely clean. Once inside the Nb chamber the cryoshrouds are cooled, and the sample is ready for deposition of the superconductor.

When growing a thin film, the correct growth temperature and rate must be selected to optimize the formation of the crystal. Through extensive testing [42] it was determined that single crystal Nb forms optimally at around a growth rate of 0.3 Angstroms per second. Unfortunately, difficulties are discovered when picking the growth temperature. Single crystal Nb is best grown at 850C, a temperature far above where significant amounts of Arsenic vapor sublimates out of the GaAs lattice. Attempts as growing at a slightly elevated temperature also failed due to the combination of increased temperature

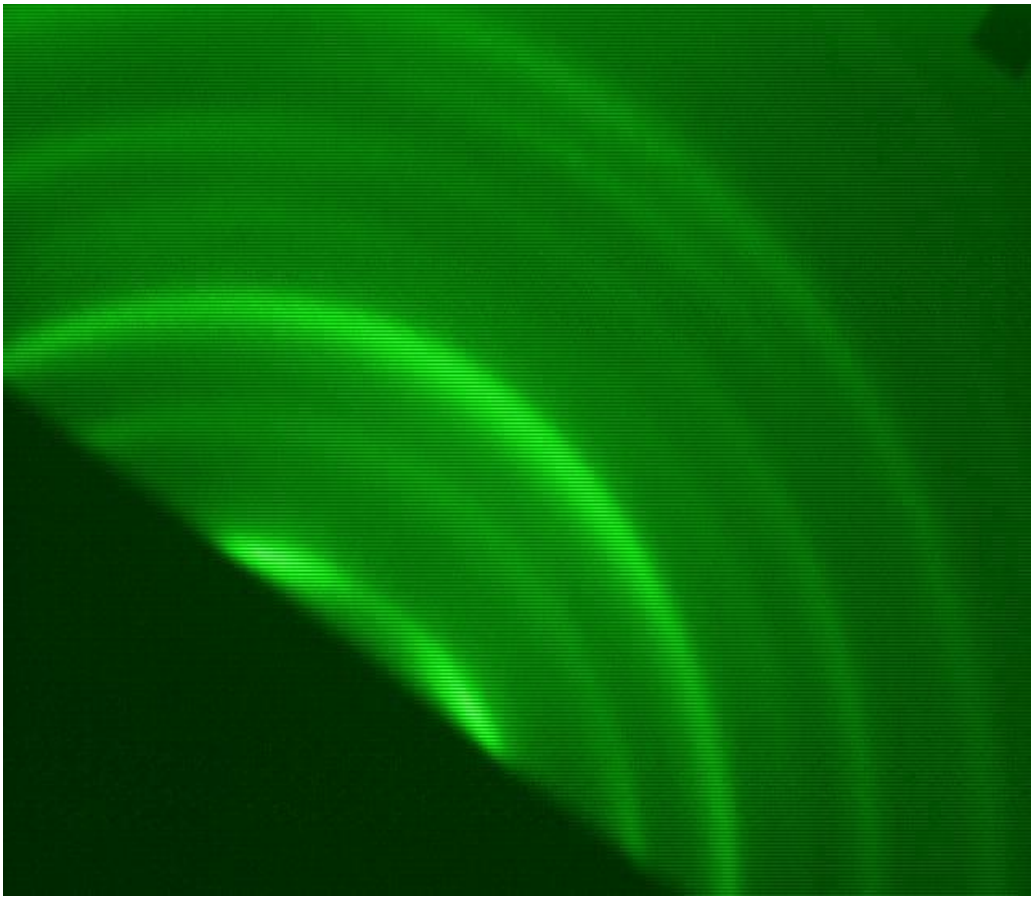

Figure 5.3: RHEED image of polycrystalline Nb deposited on the semiconducting surface. The rings in RHEED imply a polycrystalline surface.

and lattice strain of the InGaAs. After growth was completed, in the regions Nb was removed during processing the exposed semiconducting surface would be covered by many cracks due to the fracturing of the InGaAs surface. Experimentally it was determined that the optimal situation is to have no applied heat during the Nb deposition. Since the surface of the film is exposed to radiative heating of the evaporator, it is certainly no longer at room temperature. However, thermocouple measurements on the rear side of the sample on showed the substrate temperature rising by less than 50 degrees Centigrade. The Nb growth is still polycrystalline; the RHEED patterns of the completed film exhibit rings as is seen in Figure 5.3. While the thickness of the Niobium was variable, the only effect it has is on the superconducting critical temperature of the Nb film. While single crystal Nb films have critical temperatures exceeding 7K for thicknesses less than 200 Angstroms, the polycrystalline films need to be thicker than 500 Angstroms if critical temperatures above 7K are required. Once above 750 Angstroms the critical temperature stabilized in the 8.5-9K range. This thickness has applications in the processing of devices, but in typically in this project the films were between 500 and 1000 Angstroms thick. After the growth was finished the puck was allowed to cool, removed from the vacuum system, and was ready to be processed into devices.

5.3 Processing

Processing the films into devices was achieved using standard clean room photolithography and fabrication techniques. Since the quarter of a two inch wafer contains plenty of real estate, once the film was removed from the vacuum chamber it was cleaved into several different pieces. Each of these pieces could have different purposes. Van der Pauw and Hall devices measured the transport properties of the

semiconducting films, 3 terminal devices were used to determine the intrinsic properties of the proximity effect G_c and R_s, and 2 terminal thin trench devices studied if the N-S coupling depended upon the distance separating the superconducting electrodes.

5.3.1 Transport Measurements: Van der Pauw and Hall

It is important to understand the transport properties of the grown semiconducting films. Not only do transport measurements allow us to enter measured quantities into our models that are described below, but it also allows us to check the quality of the films that are grown without having to be concerned with any uncertainty introduced by the processing. Samples are prepared by cleaving the grown film such that a small square of roughly $1cm^2$ is fabricated out of the center of the film. Then molten In contacts are formed on the corners of the sample using a soldering iron. Molten In diffuses into the sample creating good Ohmic contact to even the most lightly doped GaAs and allowing for high fidelity measurements to be made. The first type of film transport measurement uses the Van der Pauw technique [43] to analyze the resistivity of the films. Knowing the resistivity allows us to subtract out the proper resistance as a function of temperature in our device model. The second measurement is the classical Hall effect [44]. This utilizes the Hall resistance to determine the number of carriers in the film. Not only is the Hall measurement a method to calibrate the flux of the Si source, and to determine the unintentional doping of the chamber, since the total number of quantum mechanical modes is related to the number of electrons in the semiconductor this measurement allows us to predict the maximum junction conductance of our devices and determine the transmission coefficient of the N-S interface.

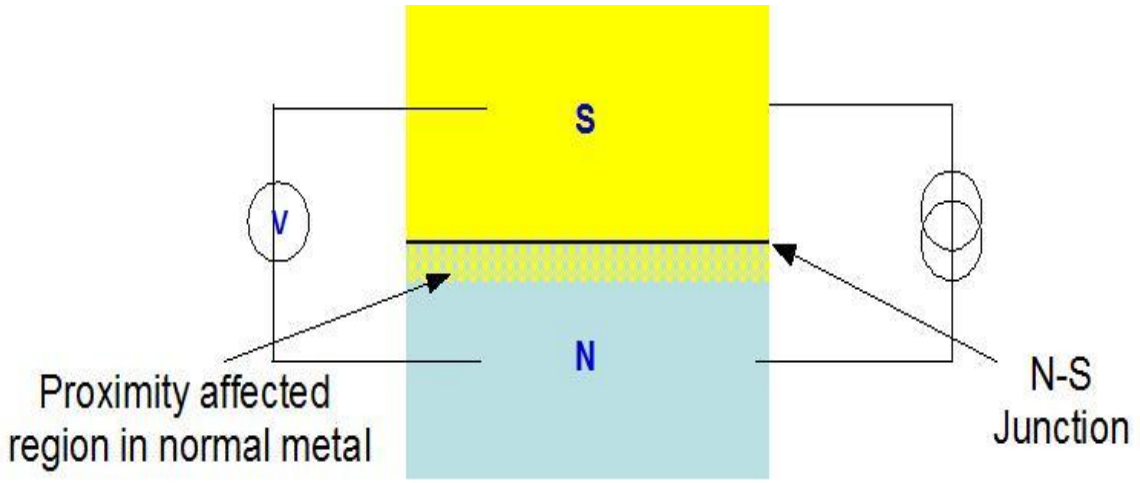

Figure 5.4: Generalized form of N-S junction. In any single measurement the junction conductance and the sheet resistance of the proximity affected region are in series and cannot be distinguished

5.3.2 Three Terminal Devices

If we are interested in understanding the superconducting proximity effect it is vital that we can distinguish between the affect on the N-S junction conductance G_c, and the transport in the semiconductor R_s. When making measurements on these devices, it is important to remember the fundamental problem that the N-S junction and the proximity affected region are in series and are impossible to separate with a single 4 point measurement. An illustration of how a single 4 point measurement is insufficient is shown in Figure 5.4. However just as one might expect, if you can make two independent measurements, then you can separate out the two unknowns of the measurement.

Our solution to this problem is to create a 3 terminal device to make the two independent measurements. An illustration of a completed 3 terminal device is shown in Figure 5.5. This device geometry allows for the measurement of two independent 4 point resistances. The measurement including the electrode in the direction of the current flow

is called V_2, and the measurement involving the upstream electrode V_3. Since the current will flow to the drain on the left hand side of the figure, there will be no current flow between the injector finger and the upstream electrode and hence no contribution to the measured voltages. The measured voltage difference is only due to the voltage drop across the N-S interface on the upstream edge of the injector finger. The downstream voltage measurement, V_2, gives information about the other end of the voltage profile. As is explained in Appendix B, the voltage profile is scaled by the transfer length, $\lambda = \frac{1}{\sqrt{G_c R_s}}$. Sampling both ends of the injector finger simultaneously unambiguously pins this voltage profile and the device model extracts the intrinsic values of the proximity effect: the N-S junction conductance, G_c and sheet resistance in the proximity affected region, R_s. The full implications of this device model are explained in Appendix B.

These 3 terminal devices were fabricated using standard photolithography techniques. First the devices must be isolated from one another to ensure the current flows through the device and not bypass it and be shunted directly to ground. After a photoresist mask is spun, exposed, and developed, Niobium is etched away using a fluorine based reactive ion etch. Then the InGaAs cap and doped GaAs are etched using a wet chemical etch consisting of 50 H_2O:1 H_2O_2:1 HCl. This etched the semiconducting surface at a slow consistent rate of 300 Angstroms per minute. While it is necessary that the various leads be isolated from one another, device yield is increased by minimizing the height of the step edge along the mesa that the link-up metallization must traverse. Therefore it was important to etch just enough such that the conducting GaAs was removed, but not so

much as to create excessive step edges. The resistance between isolated pads is checked after etching to ensure that there are no links between them. The resistance between them is at least hundreds of kilo-Ohms in magnitude. It is also important that the crystallographic orientation of the wafer be such that the (011) direction be along the direction of the fingers. Otherwise the wet chemical etch will undercut the mesa making linkup across that step edge very difficult to have a continuous metal link [31].

Following the device isolation step, a liftoff must be performed in order to link the injector finger electrodes to the mesa. The liftoff is performed by first exposing another photoresist layer, followed by developing out a liftoff photoresist profile. In order for a high device yield, it is important that the photoresist have an undercut. This profile prevents the material in the developed region from contacting the material along the top of the undeveloped resists, while also allowing for plenty of space for solvents to enter into the resist stack. The solution is well known and can be solved by using a chemical based process of soaking the photoresist in Toluene which removes some of the remaining solvent at the surface of the resist. This process step makes the surface photoresist less soluble in the developer as compared to the underlying layer, and the required undercut profile results after development. Alternatively this problem can be solved by utilizing a bi-layer of PMMA and MMA and a Deep-UV exposure. Again the underlying MMA layer is more soluble in the developer and the patterned resist develops an undercut.

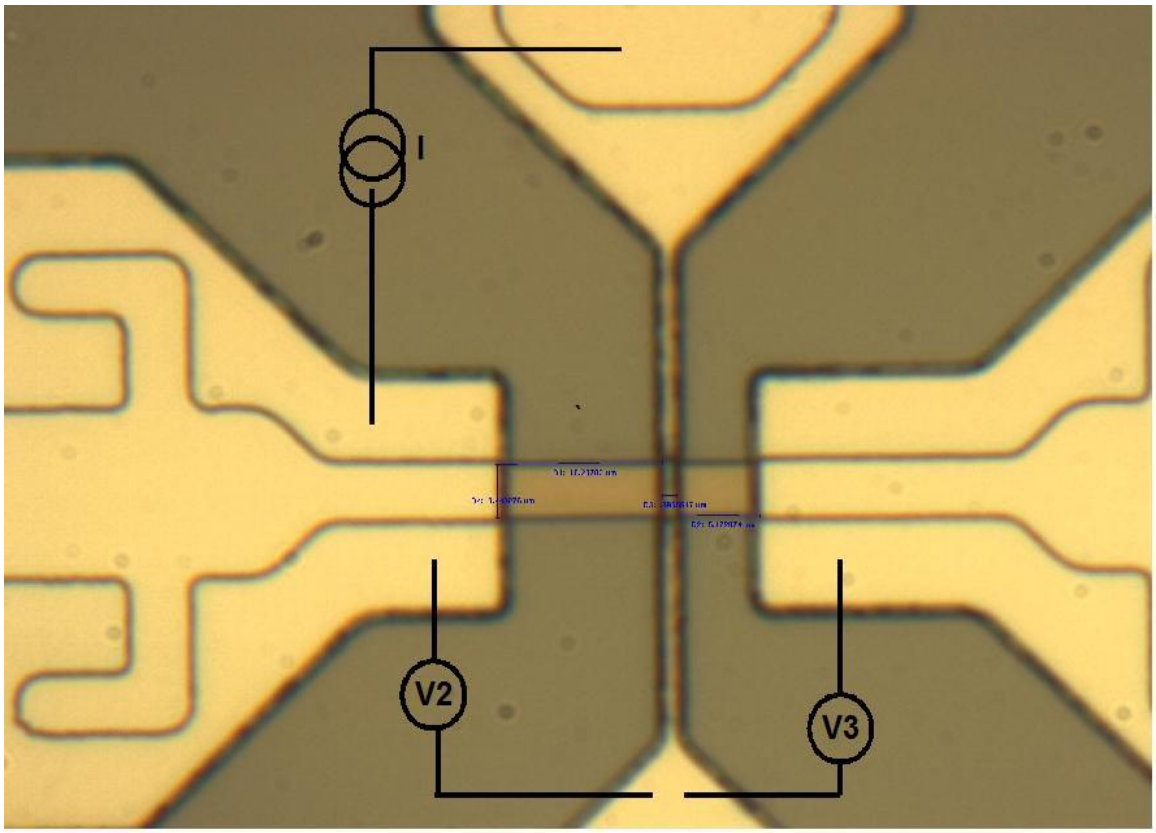

Figure 5.5: An image of a 3 Terminal device used in this project. Note the two independent voltage measurements, V2 and V3, that can be made. These two measurements in conjunction with the device model are used to determine G_c and R_s.

After properly developing out the resist, a combination of NbN and Al was sputtered onto the sample to link the injector finger to the top of the *in situ* Nb. In order for the device model of Appendix B to be valid, it is necessary that the injector finger is at an equipotential. This necessitates a superconducting wire-up material. However due to the high quality of our *in situ* Nb films, this requires an *ex situ* film that has a superconducting critical temperature greater than 9k. Having a higher T_c linkup metal removes any possible confusion about changes in the measurements being due to the affects of superconductivity on the semiconductor versus just the connections becoming truly 4 point measurements. Unfortunately we cannot just use sputtered Nb, since the

maximum T_c is of order 8.5k and would obscure the effects of the initial onset of superconductivity. The solution was to use Niobium Nitride, a higher T_c alloy, which has a critical temperature above 12K for a 1 micron width wire. As the final process step also requires an etch mask for the fluorine etch this implies that not only NbN needs to be lifted off, but also an element which can be used as an etch mask in a fluorine plasma. Though several other options were tried such as evaporated Au, Al, and Cu, it was determined that sputtered Al had additional advantage of a more conformal deposition and enough surface mobility at room temperature to obtain good coverage of the step edges. This step edge coverage ensured that the superconducting links that connected the injector finger with the contact pads were not broken during the final RIE etch.

After the sputtered NbN and Al have been deposited and lifted off, all three contacts are still connected with the Nb. At this point we have the opportunity to measure the critical temperature of the *in situ* Nb. This measurement gives an estimate of the temperature at which superconductivity starts to make inroads into the semiconductor. However once this temperature has been measured, these *in situ* Nb links that connect the contacts need to be etched away. This forces the current to flow through the semiconductor. As was discussed earlier, this process does not require an additional lithography step since the Al overlayer on the linkup material acts as an etch mask for the fluorine RIE. The Aluminium layer protects the link up NbN and the *in situ* Nb. Once this final etch is complete the device is ready to be measured.

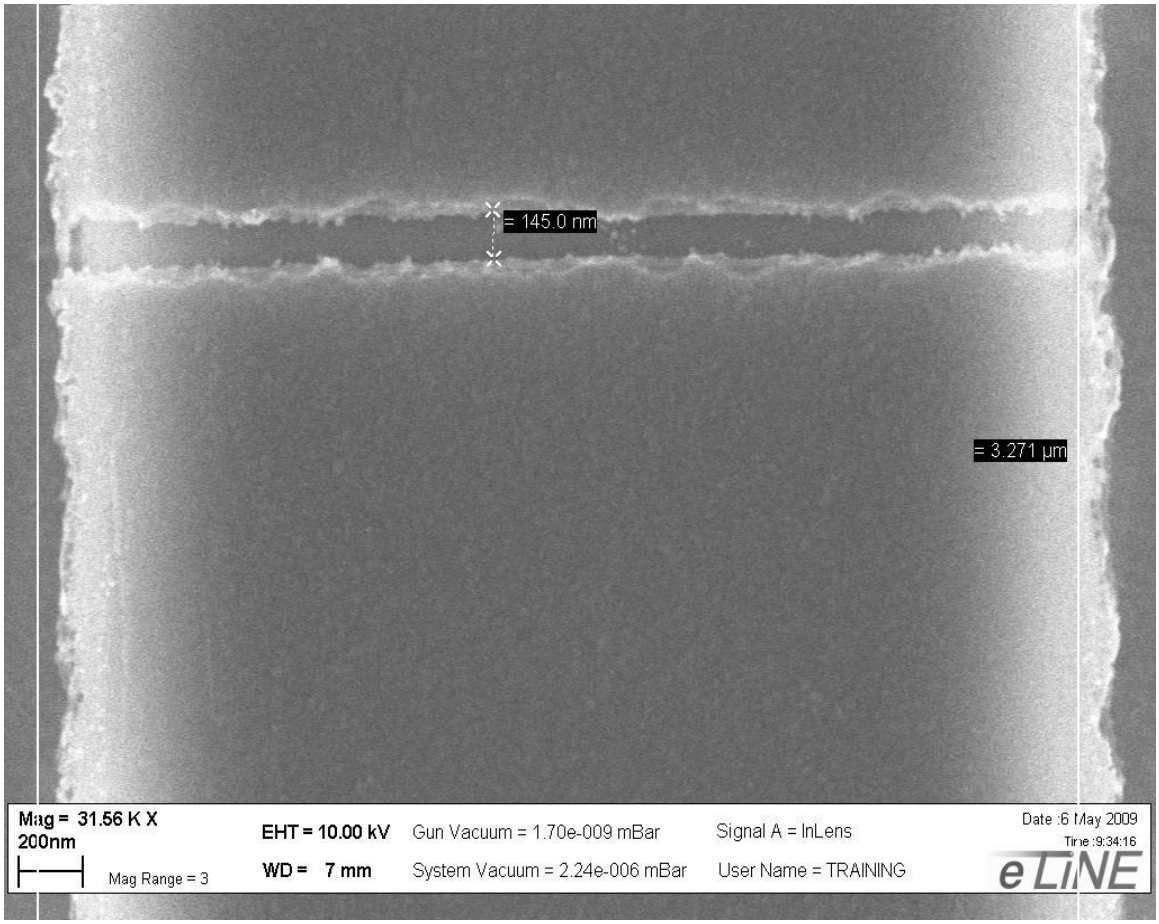

Figure 5.6: A SEM image of a thin trench device fabricated by e-beam lithography. The two electrodes are at the top and bottom with the thin trench of GaAs connecting them in the middle.

5.3.3 Thin Trench Devices

While three terminal devices allow us to create devices with multiple voltage taps and understand the nature of the proximity effect, the difficulty in lifting off material in very close proximity to each other makes it hard to fabricate devices that have very narrow gaps between the injector finger and the drain. However, if we are willing to fabricate different styles of devices on the same wafer it is possible to try to understand how the width of the semiconducting gap between the injector finger and the drain affects the

measurement. The device isolation process is identical to the three terminal devices. However, in this case no contacts are lifted off. Instead, the Raith electron beam writer is used to draw a very narrow line in a PMMA resist layer, exposing a narrow section of Niobium. This trench is then etched in the RIE, with the PMMA acting as an etch mask to prevent the rest of the Nb from being affected. An SEM image of one of these devices is shown in Figure 5.6. Trench widths as small as 75nm have been achieved, but widths less than 100nm success are not very repeatable. The exposure process from creating extremely small line widths make etching the Nb non-uniform and increases the likelihood that a sliver of Nb is not etched as seen in Figure 5.7. Using the double pass exposure techniques developed by McArdle [45] improves the uniformity, but the smaller widths still have a low yield. As PMMA is slowly etched in the SF6 plasma, the resist that shields these tendrils can be removed, but unfortunately the plasma also etches back the walls of the resist increasing the width of the trench.

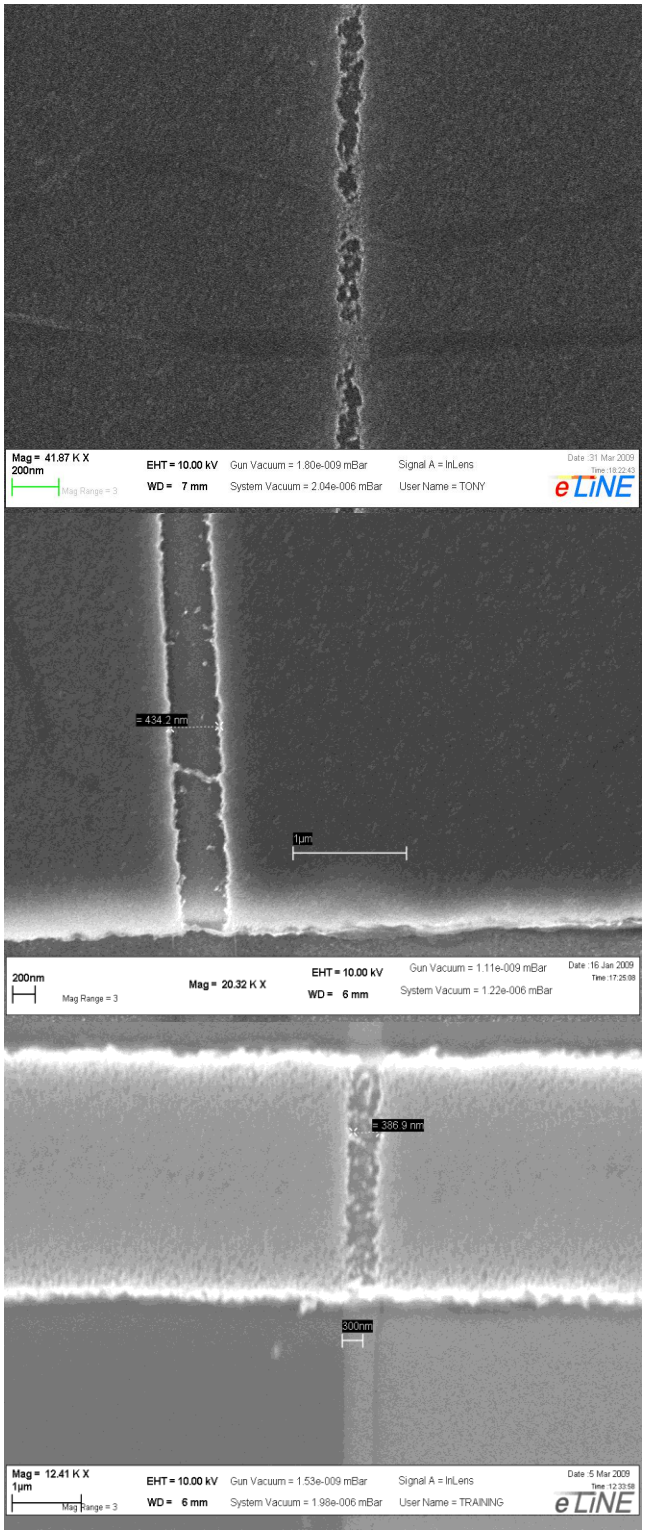

Figure 5.7: Failures in thin trench device processing typically result in the devices being shorted due to underexposure or development, insufficient etching in the RIE, or a tendril of Nb linking the two electrodes.

Chapter 6 Data and Analysis

This chapter describes and discusses the results we obtained studying the proximity effect at superconductor-semiconductor junctions. We examined interfaces between different semiconductors and niobium and quantified the proximity effect as a function of temperature and important junction parameters. To quantify how the proximity effect changes junction transport we measured the specific junction conductance, G_C, which has units of Siemens/cm^2, and the two dimensional sheet resistance of the semiconductor right under the niobium layer, R_S, which has units of Ohms/square.

Among the most important junction parameters is the transmissivity, which even in dirt-free junctions is small if a Schottky barrier is formed at the surface of the semiconductor. For the III-V semiconducting films we used, the concentration of indium at the surface controls the height of the barrier. In GaAs the surface Schottky barrier is 0.7 eV high, while for $In_xGa_{1-x}As$ the barrier is (0.7-x) eV for x<0.7 and zero for x>0.7. We studied interfaces between niobium and $In_{0.3}Ga_{0.7}As$ as well as to pure InAs. In the case of the InGaAs alloy, we obtained a poor single particle transmission coefficient, $|T|^2 = 0.04$ despite extensive optimization of the InGaAs structure. When we studied junctions to InAs, we obtained $|T|^2 = 0.73$, close to the limit of 0.92 set by the mismatch in Fermi velocities between the niobium and InAs layers.

The behavior of G_C and R_S versus temperature was essentially opposite for these two cases. The proximity effect showed up in the junctions to InAs as a R_S that monotonically decreased below T_C, due we suggest to enhanced Ohmic transport due to pair correlations

present in the semiconductor because of proximity to the overlaying niobium film. These samples also showed distinctly different current-voltage characteristics. Junctions with poor transmissivity showed tunnel junction like I-V curves, consistent with predictions of the BTK theory, while junctions with nearly perfect transmissivity showed very large zero bias conductance peaks, approximately a factor of two greater than the normal state value at low temperatures. The shape of the measured I-V curves is not consistent with Andreev reflection. This is also apparently not the precursor to a supercurrent, either, since we found it to be a local effect, occurring right at the interface. Instead we propose that it is a result of how the proximity effect changes the electronic state of the semiconductor adjacent to it.

We also found that coupling the region where the proximity effect should introduce pair correlations to a large normal layer actually reduces pair correlations, even right at the interface to the superconductor. The large normal reservoir acts to remove correlations at the interface that are present in thinner semiconductor layers having the same interface transmissivity. Specifically, we observed this in junctions with poor transmissivity in which the connection of the semiconductor to the superconductor is weak. This "anti-proximity effect" is similar to the theory of coupling to a normal reservoir described by Nazarov. For thin enough layers, the pair correlations appear to persist long enough to build up amplitude at the interface. Such a finding is reminiscent of the interplay of the Thouless length and energy scales describing correlations in a diffusive conductor. In our case, pair correlations extend in some range around the Fermi energy, and we find that for thin enough layers, even with poor junctions the signature of

a proximity effect is observed in both G_C and R_S. On the other hand, when the sample thickness is larger, the effects are not seen.

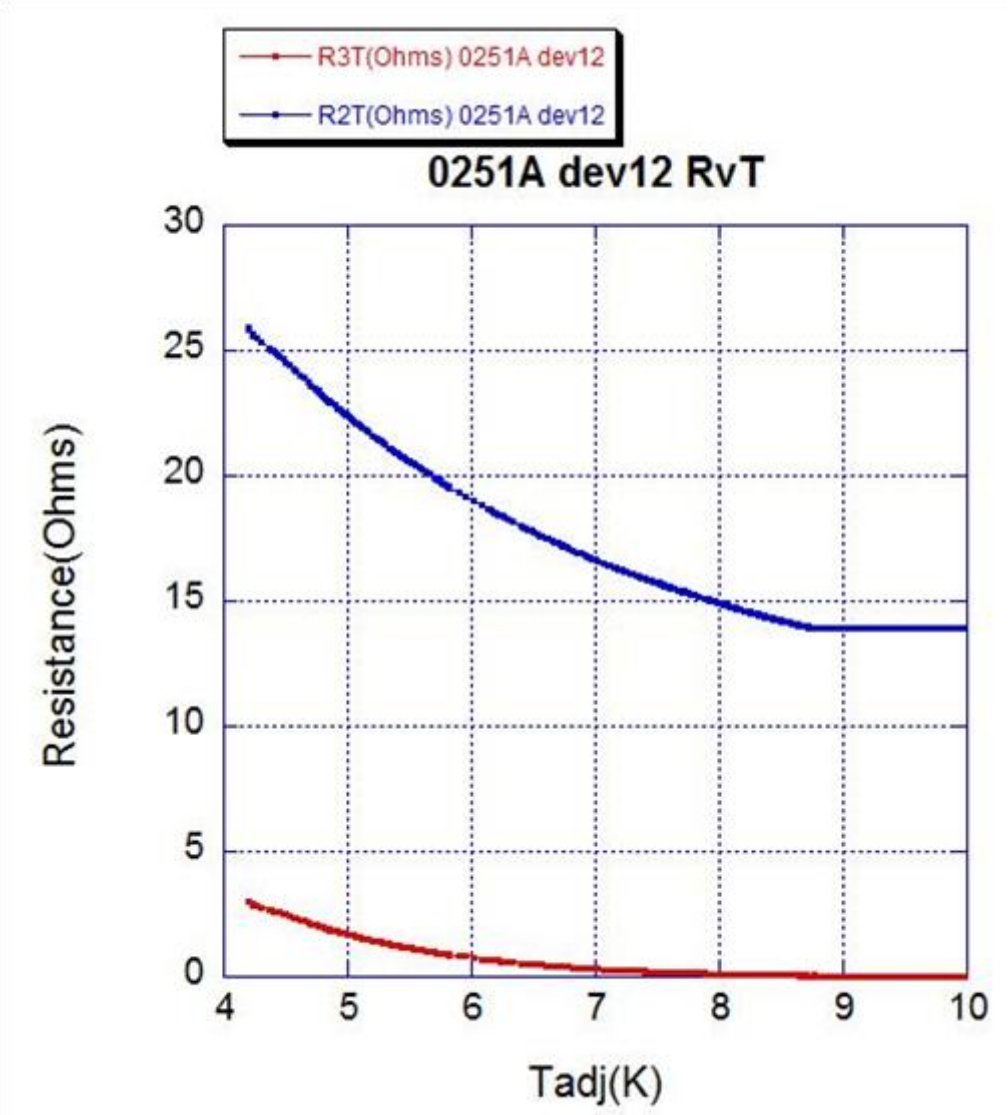

Figure 6.1: Raw data of a typical 3 terminal device fabricated out of an $In_{0.30}Ga_{0.70}As$ cap on a thick GaAs conduction channel

6.1 InGaAs Interfaces

In order to increase the transparency of the N-S interface beyond what is obtained from GaAs, a capping layer was created by grading Indium into the GaAs. InAs does not

form a Schottky barrier to Nb and the Schottky barrier of the alloy InGaAs reduces linearly with In concentration. As discussed in Chapters 4 and 5, the strength of the remaining Schottky barrier depends upon the position of the final delta doping layer, and the Schottky barrier primarily determines the transparency of the InGaAs interface. In order to determine the junction transparency, the novel 3 terminal device structure discussed in the previous chapter is utilized to extract how G_c and R_s are affected by the overlaying Nb.

Using the three terminal device structure we make two independent 4 point voltage readings which are converted into the resistances R_2 and R_3. The dependence of the R_2 and R_3 measurements on temperature from a thick GaAs film capped with $In_{0.30}Ga_{0.70}As$ are shown in Figure 6.1. These raw resistances reach a minimum value just below the 8.75K critical temperature of the *in situ* Niobium, and both resistances increase as the temperature drops. Since an otherwise identical measurement of the semiconductor connected to normal contacts is completely flat in this temperature range, these measurements indicate that there is an effect on both of these resistances due to the presence of superconductivity. However, without a device model nothing quantitative can be said about either superconductivity's effect on the sheet resistance in the proximity coupled region, R_s, or on the junction conductance of the semiconductor-superconductor interface, G_c. These are the two fundamental quantities that measure the manifestation of the proximity effect. In order to understand these phenomena, it is necessary to understand how the upstream and downstream resistances, R3 and R2, depend on these intrinsic quantities.

The two independent measurements that are made in a three terminal device, R_2 and R_3, contain sufficient information to determine the intrinsic properties that we are interested in, G_c and R_s. Each of these measured values is a convolution of both of the intrinsic quantities. However, using a simple Ohm's law model we find that a one to one mapping exists at low bias and that the measured resistances can be written in terms of the intrinsic quantities. These expressions can then be inverted to find how G_c and R_s depend upon temperature. The device modeling required to extract the intrinsic properties was first introduced by Flexner [4] and is extended in this project. The full derivation of the procedure needed to extract the intrinsic properties is contained in Appendix B.

The two independent voltage measurements unambiguously pin down the voltage profile beneath the injector finger. The spatial dependence of the voltage profile is scaled by the value of the transfer length,

$$\lambda = \sqrt{\frac{1}{G_c R_s}} \ , \tag{6.1}$$

which is a function of the two intrinsic parameters we are interested in. As shown in Appendix B, the intrinsic quantities can be rewritten in terms of the measured resistances where $\tilde{R}_2$ is the downstream resistance with the parasitic semiconducting trench resistance removed. These formulae are

$$G_c = \frac{2}{wL} \frac{\tilde{R}_2}{\tilde{R}_2^2 - R_3^2} \ln\left(\frac{\tilde{R}_2}{R_3}\right), \tag{6.2}$$

and

$$R_s = \frac{w}{2L}\frac{\tilde{R}_2^2 - R_3^2}{\tilde{R}_2}\ln\left(\frac{\tilde{R}_2}{R_3}\right). \tag{6.3}$$

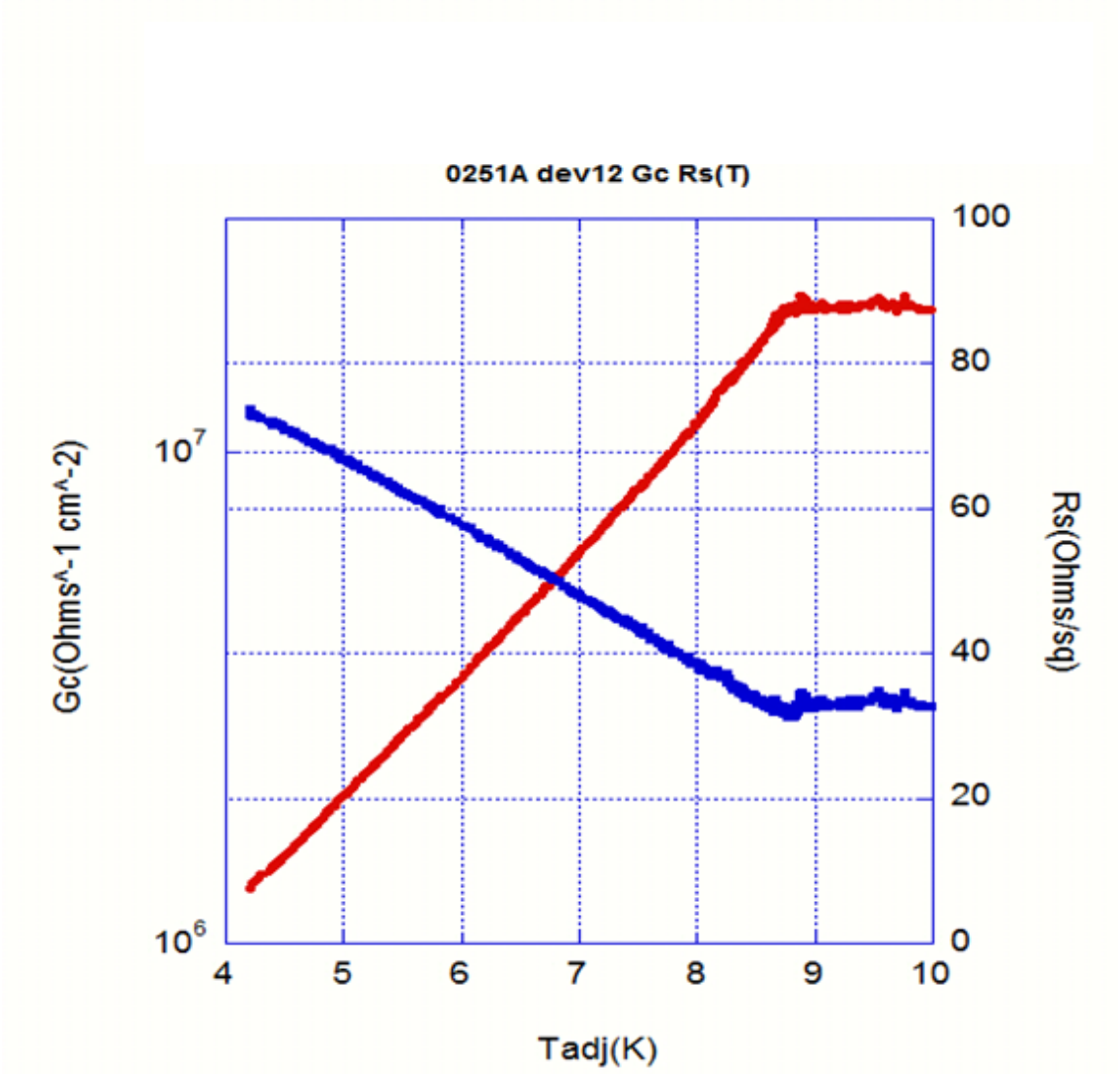

Figure 6.2: Extracted data for the N-S junction conductance, G_c, and the sheet resistance of the semiconductor under the injector finger, R_s, as a function of temperature for a 3 terminal device fabricated out of a $In_{0.30}Ga_{0.70}As$ cap on 2000 Angstroms of doped GaAs. Both values begin to change at the 8.75K T_c of the *in situ* Nb.

The extracted intrinsic quantities for the sample that gave the raw data shown in Figure 6.1 is shown in Figure 6.2. The sample consisted of a 2000 A thick doped GaAs

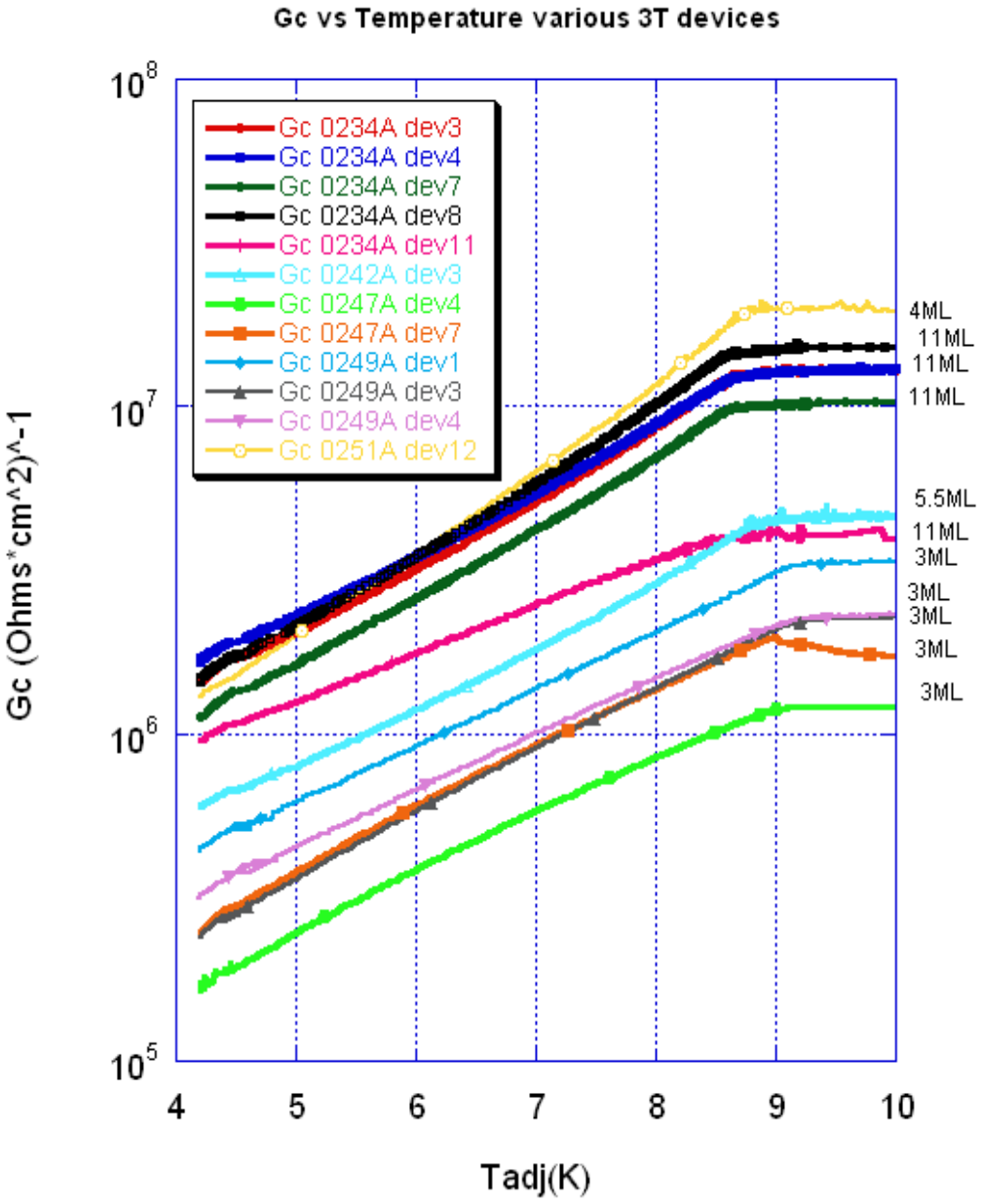

Figure 6.3: Extracted N-S junction conductance vs temperature for 13 devices encompassing 5 differing placements and sheet densities of the final Silicon delta doping layer in otherwise identical $In_{0.30}Ga_{0.70}As$ capped 2000 Angstrom thick GaAs conduction channels. The junction conductance is extremely sensitive to the location of this delta doping layer. Notice how the curves are grouped by the placement of the final delta doping later.

semiconducting layer capped with $In_{0.30}Ga_{0.70}As$ and covered with *in-situ* niobium. In

this particular epitaxial structure as the temperature drops below the 8.75K T_c of the Nb electrodes, the junction conductance decreases and the sheet resistance rises.

Later in the chapter the effect of differing epitaxial structures will be explored, and our ability to tune the strength of pair correlations by altering the N-S junction conductance and the thickness of the semiconducting layers will be shown. Already we have shown that unlike previous authors who lacked 2 independent measurements and were restricted to analyzing raw data and interpreting the measured *device* resistance, the extraction of the intrinsic properties provides a more complete view of the superconducting proximity effect on the transport in the semiconductor and the N-S junction.

The coupling of the superconducting and semiconducting layers depends strongly upon the quality of the contact that couples the two layers. This relationship is supported both by the theoretical basis developed in Chapter 2 and the previous experimental results discussed in Chapter 3. Correspondingly, it is important for us to evaluate the quality of the junctions we create. As can be seen in Figure 6.6, the highest extracted junction conductance using $In_{0.30}Ga_{0.70}As$ based caps is roughly $2x10^{7}$ Scm^{-2}. Comparing this value to our ideal junction limit in section 4.2.3 implies that this cap has a transmission probability of 0.04. This extracted value of $|T|^2$ is very close to the WKB calculation for the predicted transmission coefficient through the remaining Schottky barrier after the with the optimal InGaAs cap. Also from the figure it is clear that small differences in the structure of the cap cause large differences in the measured G_c. All of the devices in this plot are identical except for the placement of the final heavy delta doping layer described in section 5.1.3. This final delta doping layer is designed to terminate the Schottky

barrier at the depth it is placed. The placement ranges from 11 monolayers from the surface in wafer 0234 to 3 monolayers from the surface in wafer 0247. The depth in monolayers of this layer in each $G_c(T)$ curve is labeled, and the curves are clustered based upon this parameter. Slight variations in the cap structure make it is possible to vary the conductance of the junction by a factor of 10. This is mainly due to the difference in the depth of the Schottky barrier, but it is also caused by impurities or defects in the semiconductor. Samples that contained too high of a density of Si donors exhibited decreased epitaxy. While the devices with the final delta doping layer 3 monolayers from the surface would have had the thinnest Schottky barrier, the increase in disorder caused a negative net effect on the junction conductance.

Wafer	Depth of final delta doping layer	Measured G_c	$\|T\|^2$
0234	11 Monolayers	$9x10^6 Scm^{-2}$	.02
0242	5.5 Monolayers	$7x10^6 Scm^{-2}$	.01
0247	3 Monolayers	$2.0x10^6 Scm^{-2}$	.004
0249	3 Monolayers	$2.5x10^6 Scm^{-2}$	.004
0251	4 Monolayers	$2x10^7 Scm^{-2}$	.04

Table 6.1 Comparison of the effect of the depth of the final delta doping layer on the junction conductance G_c and transmission coefficient $|T|^2$.

A summary that compares the cap structures and the measured junction conductance of these devices can also be found in Table 6.1. Figure 6.6 and Table 6.1 also show how the geometry of the cap adjusts the transmission coefficient of the N-S interface. Since

other than the depth of the Schottky barrier these films are otherwise identical, we ensure that the number of modes remains constant. All measured changes in the junction conductance are solely attributable to differences in the transmission coefficient.

These InGaAs-Nb and InAs-Nb interfaces are the most conductive and most transparent devices of their type *ever* created. The extracted value of $2x10^{7}\ Scm^{-2}$ for G_c is greater than what was obtained by any of the previous groups discussed in Section 3.2 or shown in Table 6.2. The fundamental quantity $|T|^2$ exhibits an even greater increase over previously reported results. In fact, the transmission probability of the InGaAs cap is actually a factor of 10 higher than that reported by Nguyen [23] for his Schottky barrier free InAs devices. This result shows the value of the completely *in situ* transfer method.

Author	Structure	Doping	Measured G_c	$\|T\|^2$
Kastalsky [1]	Nb on $In_{0:53}Ga_{0:47}As$	$2x10^{19}cm^{-3}$	$9x10^{5}Scm^{-2}$	.0011
Taboryski [19]	Al on GaAs	$> 4x10^{18}cm^{-3}$	$2x10^{6}Scm^{-2}$	.0063
Nguyen [20]	Evap Nb on InAs	$6x10^{18}cm^{-3}$	$2x10^{5}Scm^{-2}$	.00056
Nguyen [23]	Sputt Nb on InAs	$6x10^{18}cm^{-3}$	$2x10^{6}Scm^{-2}$	.0056
Giazotto[18]	Nb on GaAs	$> 4x10^{18}cm^{-3}$	$2x10^{6}Scm^{-2}$	.0063
Vissers	Nb on $In_{0:30}Ga_{0:70}As$	$8x10^{18}cm^{-3}$	$2x10^{7}Scm^{-2}$	.04
Vissers	Nb on InAs	$4x10^{18}cm^{-3}$	$2x10^{8}Scm^{-2}$	.73

Table 6.2 Table of contact conductances and transmission coefficients of various other authors as compared to those found in this project.

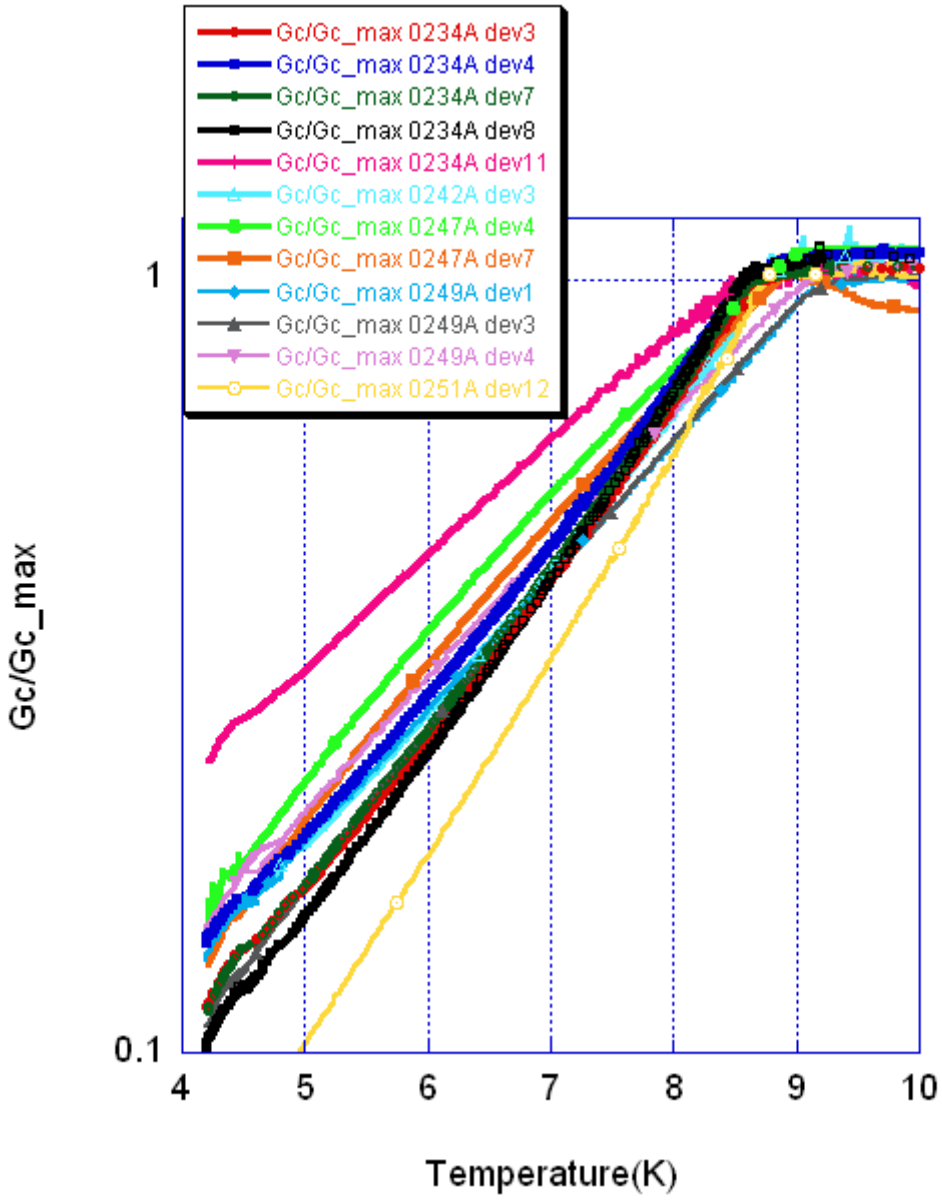

Figure 6.4: Plot comparing $\frac{G_c}{G_c(T_c)}$ for various $In_{0.30}Ga_{0.70}As$ epitaxial capping structures on 2000 Angstroms doped GaAs conduction channels.

While the optimization of the InGaAs cap increased the transmission coefficient of the N-S interface, the inability to completely eliminate the Schottky barrier meant that $|T|^2$ was limited to being 0.04. While the $G_c(T)$ curves look qualitatively similar in Figure

6.3, this similarity is made clearer if we instead plot the reduced conductance $\frac{G_c}{G_c(T_c)}$, as in Figure 6.4. The reduced conductance curves of the interfaces look identical, despite the more than order of magnitude difference in the transmission coefficient. A similar relationship holds true for the dependence of R_s on the transmission coefficient. This result implies that even the most transparent InGaAs interface does not cause a qualitative difference in the coupling of superconductivity. As we will see later, the positive effect of increasing the junction conductance and strengthening the coupling to the superconductor is completely suppressed by the normal reservoir present in these thick semiconducting layers.

6.2 InAs Interfaces

As the InGaAs capped devices did not show sufficient transparency, interfaces containing 100% InAs were also created. Though this is a different semiconductor, it is very similar in doping and normal transport to the GaAs/InGaAs based layers and can be substituted without altering the superconducting electrode. Therefore, comparison of this interface with the InGaAs interface reveals the effect of an increased junction transparency. We found that the ability to grow Schottky barrier free interfaces allowed the transmission coefficient to be tuned to almost its theoretical limit set by the Fermi velocity mismatch of the Nb and InAs.

Three terminal devices were fabricated out of the InAs samples in an identical fashion as in the previous case. An example of the three terminal InAs-Nb raw data and how it contrasts with that of interfaces with an $In_{.30}Ga_{.70}As$ cap is shown in Figure 6.5. The downstream resistance, R_2 decreases as the temperature is lowered below T_c. This is the

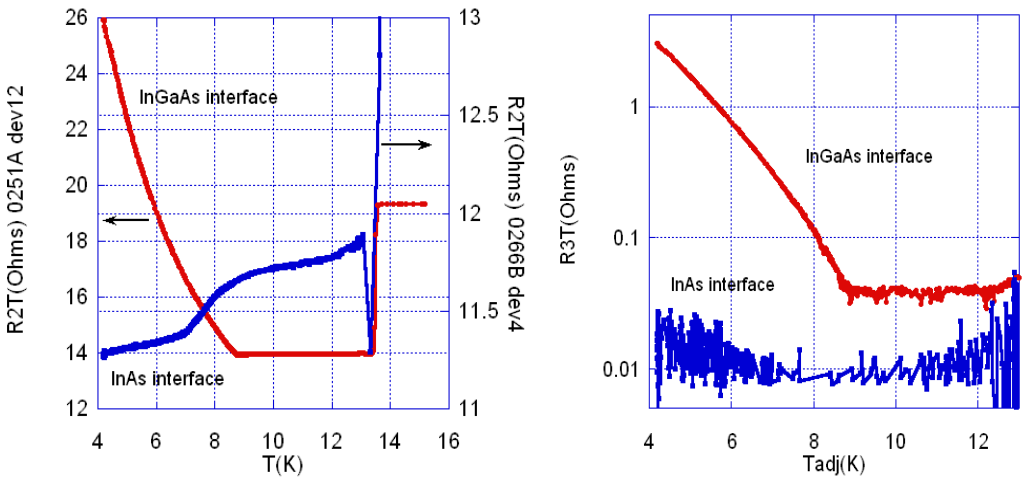

Figure 6.5: Comparison of raw data of 3 Terminal InAs device (Blue) to the most conductive $In_{0.30}Ga_{0.70}As$ device (Red).

opposite of the InGaAs interface where R_2 increases at lower temperatures. The R_3 measurement is similar in that it increases in both cases as the temperature is decreased below T_c, but there is a large difference in magnitude of the measurement.

The difference in the R_3 curves in the right side of Figure 6.5 indicates that there is a large difference in magnitude between the measured resistances of the InAs and InGaAs interfaces. However, this raw measurement is complicated by the decreased transfer length in the higher G_c InAs interfaces. This smaller transfer length implies that the difference in the measured R_3 values is larger than just the increased G_c, once again showing the value of our device model. Processing difficulties arose in fabricating continuous working 3 terminal devices due to the crystallographic effects of the device isolation wet chemical etch. This complication resulted in only devices with wide injector fingers being successfully fabricated. By itself, the larger injector finger would have reduced the measured R_3, but this reduction was further compounded by the increased junction conductance of the Nb-InAs junctions. As can be seen in Figure 6.6, the greatly

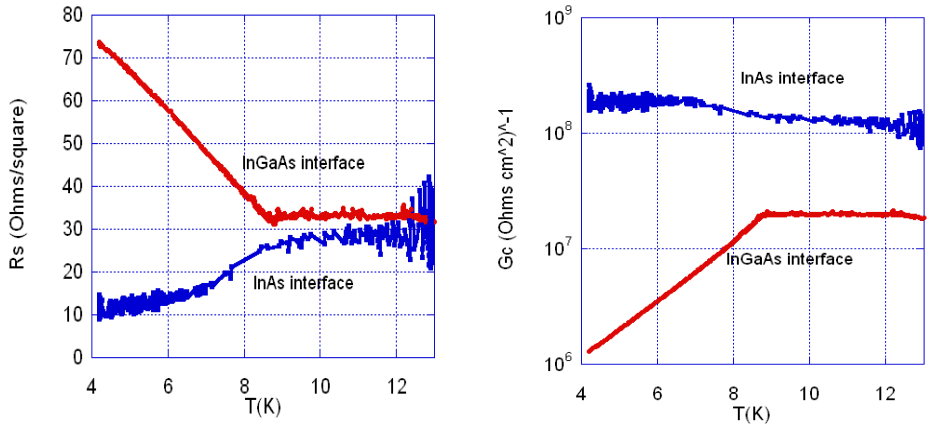

Figure 6.6: Comparison of extracted intrinsic data of a 3 terminal InAs device (Blue) to the most conductive device whose epitaxial structure consists of InGaAs with a thick semiconducting layer(Red).

increased junction conductance along with a sheet resistance that is similar to that of the GaAs caused the transfer length, $\lambda = \sqrt{\frac{1}{G_c R_s}}$, to become much shorter than in the lower transmission coefficient $In_{0.30}Ga_{0.70}As$ caps. This small transfer length compared to the size of the injector finger means that the V_3 measurement that samples the upstream edge of the finger reads a voltage that was a small fraction of the downstream voltage and as a result of this effect the measured R_3 resistance was extremely small.

The very small measured voltage will introduce some uncertainty to the extracted results, but the intrinsic values are still clear enough to understand how the increased transmission coefficient modifies the proximity effect. The raw R_2 and R_3 curves can be processed using the device model outlined in Appendix B; the G_c and R_s of an InAs 3 terminal device are displayed in Figure 6.6. The junction conductance, G_c, of the InAs device, is considerably greater than the best InGaAs device at T_c. Using the analysis of Chapter 4 and the known carrier density, the transmission coefficient of the Nb-InAs interface is 0.73. Additionally, G_c increases by a factor of 1.6 as the temperature is

reduced from the 13K to 4.2k. R_s decreases to almost a third of its normal state value. These are the opposite of the results seen with the InGaAs interface. Whether the curves have the exact form shown in the figure or deviate slightly from that in the temperature

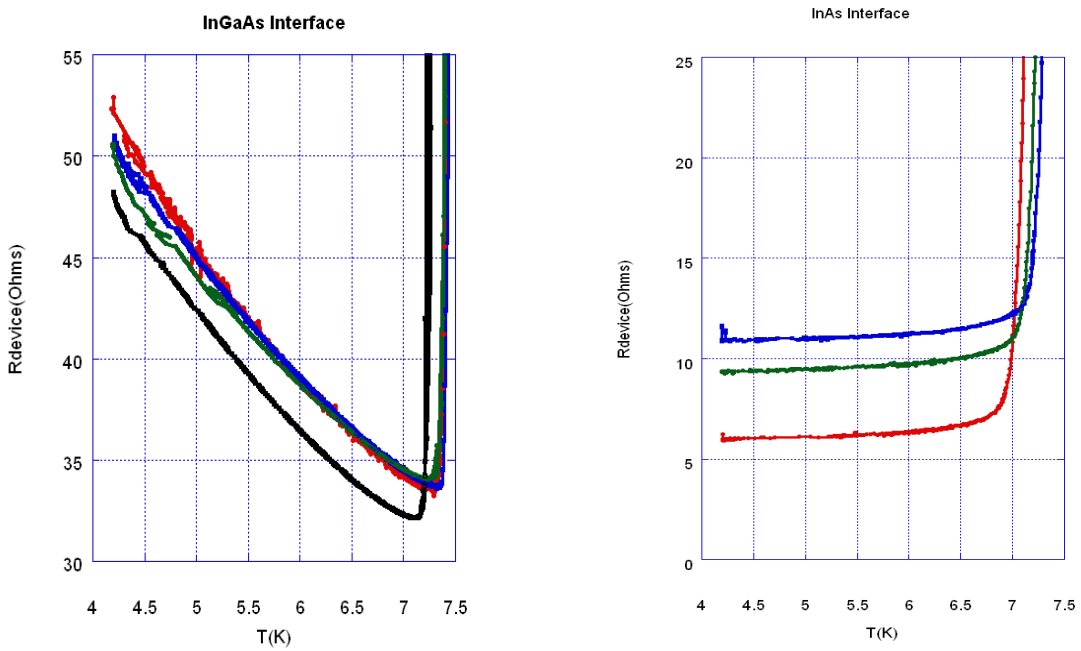

Figure 6.7: Comparison of raw data of thin trench devices for $In_{0.30}Ga_{0.70}As$ on a 2000A GaAs conduction channel (left) and InAs (right) devices for a variety of widths. The resistance of the InGaAs capped devices increases while the resistance of the InAs devices decreases as the temperature drops.

range of 7.5 to 8.5 K is less clear, since the least reliable temperatures in that range are also where the greatest changes occur.

Now that the transparency of the InAs-Nb contacts has been determined, two terminal thin trench devices were fabricated to determine if the superconducting electrodes can be made to coherently couple across the semiconducting trench. An example of the raw RvT data for thin trench InAs devices can be seen in Figure 6.7 with the most transparent $In_{0.30}Ga_{0.70}As$ devices as a comparison. The resistance of the InAs device decreases as the

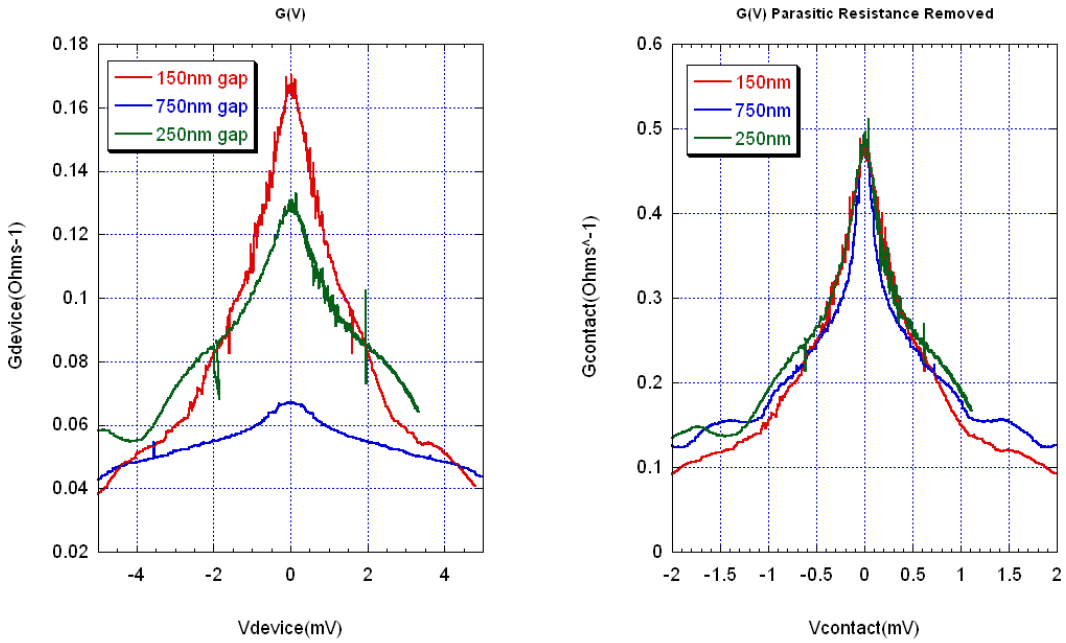

Figure 6.8: Conductance versus voltage plots for identical thin trench InAs devices of various widths. Raw data is on left, on the right is conductance of a single N-S contact. Note that subtracting out the variable gap resistance from both the DC voltage and the differential conductance measurements allows the G(V) curves from all of the devices to collapse on to each other.

temperature is lowered in contrast to the all thick InGaAs capped devices whose resistance increases with decreasing temperature.

Qualitative differences because of the greater junction transparency are also present in the curves taken at finite bias. All measured devices with InGaAs caps on thick GaAs conduction channels exhibit a minimum in the zero-bias conductance at 4K, but the InAs devices instead have a maximum at zero bias as shown in Figure 6.8. The differences in the raw G(V) curves in the figure to the left are due to the differing distances separating the superconducting electrodes. As the length between the electrodes is reduced, the peak in conductance at zero bias increases and becomes sharper. This effect could be due to either coherent coupling between the two electrodes as the trench length shrinks or just the result of a smaller parasitic resistance. In order to discriminate between these hypotheses the raw data is transformed from the conductance of the device into the

conductance of a single contact. The distances separating the electrodes on the different devices were measured using a SEM, and the sheet resistance of the InAs at low temperature was measured on a test sample using the Van der Pauw technique. The combination of these two measurements allowed the calculation of the resistance of the semiconducting trench for each of the three devices. If this resistance was subtracted from both the differential conductance and the DC voltage the curves of the three different devices collapsed onto each other as seen in the right panel of Figure 6.8 This result implies that there is no coupling of the electrodes for distances larger than 250nm and temperatures down to 4.2K. If coupling existed it would have been impossible to fit the curves using a common sheet resistance value.

While the IV curves exhibit clear indications of excess current and are reminiscent of a noise or temperature rounded Josephson junctions, and all devices that were fabricated with unambiguously etched trenches had an increasing zero bias conductance as the temperature was reduced, none exhibited a true supercurrent. Whether a supercurrent would be observed by taking devices to a lower temperature or by fabricating thinner trenches is not known. The application of microwaves acted as an effective temperature, with sufficient amounts of power erasing the effects of superconductivity. No Shapiro steps were ever observed despite the clear presence of an increased zero bias conductance. So the enhanced zero bias conductance we observed as the temperature was lowered is apparently a local effect, happening just at the superconductor to semiconductor interface. It does not happen because of a coherent coupling between the two superconductors, rather it happens because of the local proximity effect at the interface.

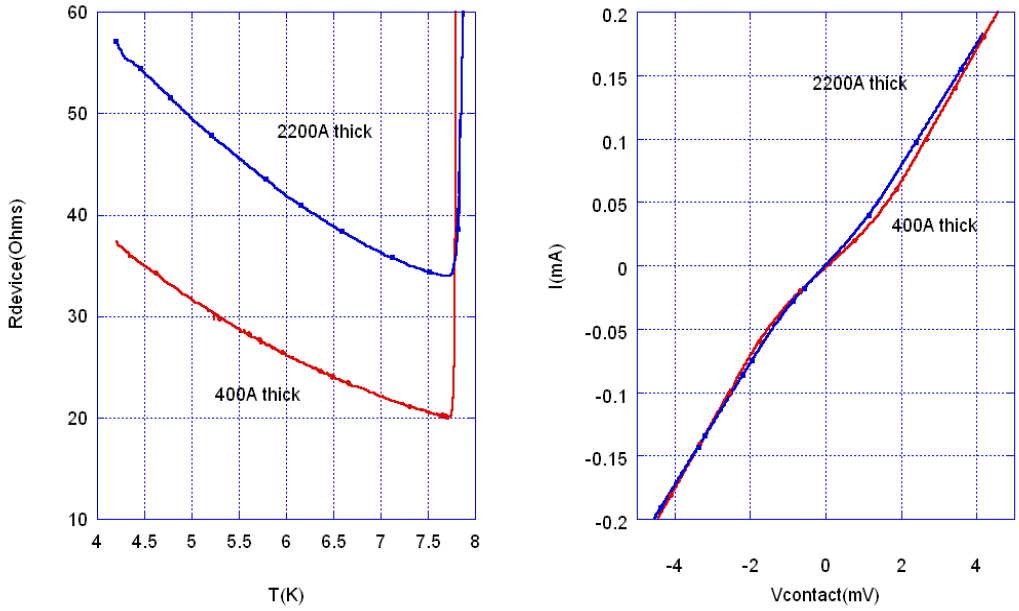

Figure 6.9: Comparison of the resistance versus temperature and current versus voltage of the contacts for 2000A and 200A thick channels. Note the similarity in the IV and RvT curves. In both cases the existence of the normal reservoir suppresses the pair correlations in the interface region. The difference in the normal state sheet resistance is due to the different thicknesses of the semiconducting channel which makes the effective size of the contacts and the absolute resistance scales differ.

6.3 Semiconductor Layer Thickness

Another parameter that can be varied is the thickness of the semiconducting film. When the semiconducting and superconducting layers are both semi-infinite, de Gennes showed [11] that the order parameter decreases exponentially as distance increases from the N-S interface. These models indicate that deep in the normal metal the material will be unaffected by superconductivity and by definition will be part of the normal reservoir. The model of Nazarov [2] and Gueron [16] predicts that the presence of this normal reservoir will lead to a suppression in the pairing correlations near the N-S interface. Conversely when the semiconducting layer is thin, the entire semiconducting layer will be influenced by the superconductor and no normal reservoir will be present. In this case,

Nazarov predicts that the pairing in the interface region will be enhanced relative to the thicker semiconducting layers.

Due to the flexibility of MBE, it is not difficult to construct semiconducting layers of varying thickness that each contain the same 200A $In_{0.30}Ga_{0.70}As$ cap, and hence the same N-S junction transparency. Thicknesses of 2000 and 4000 Angstroms were tried previously by Flexner [4] without any effect, and in this project semiconducting structures consisting of the 200 Angstrom InGaAs cap plus doped GaAs conduction channels of depth 0, 200, 1000, and 2000 Angstroms were created. A comparison of semiconducting epitaxial structures of total depth 2200A and 400A is shown in Figure 6.9. The reduction of depth from 2200 to 400 Angstroms had little qualitative effect as the I-V curves and RvT curves remain quite similar.

If the semiconductor structure is reduced to just the 200A InGaAs cap, a qualitative change occurs. While the resistance versus temperature curve for the 200A cap in Figure 6.10 is still increasing as temperature is lowered, albeit slightly, the I-V curves in Figure 6.12 now exhibit a reduced resistance region at low bias. This indicates that the reduction to just 200A of semiconductor has caused a qualitative difference in the effect of superconductivity on the interface region.

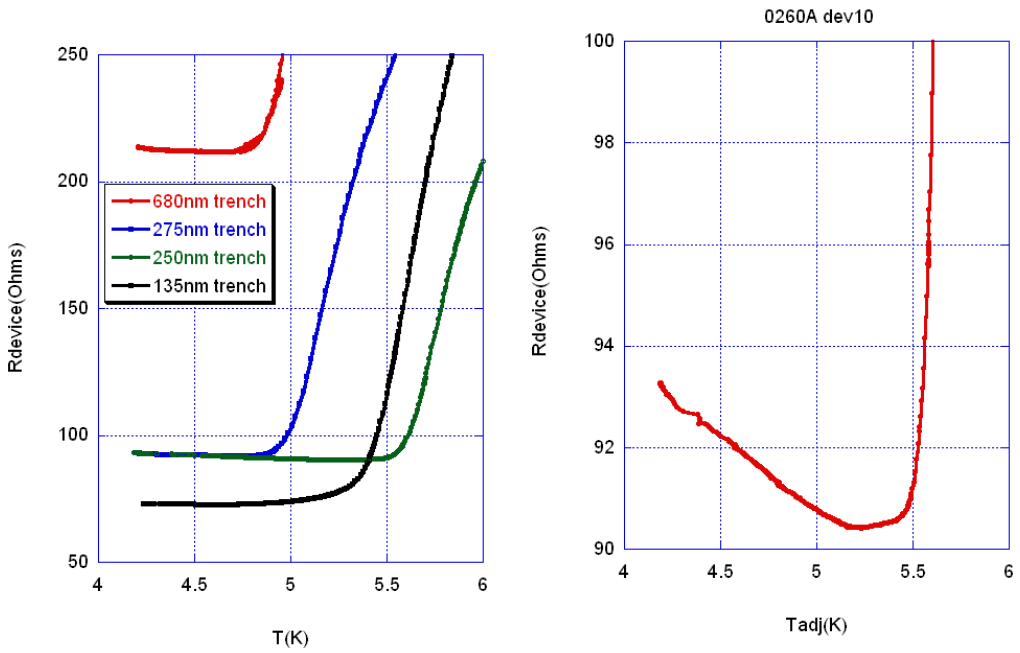

Figure 6.10: (Left) Resistance versus temperature curves for thin trench devices that consist of only a 200A $In_{0.30}Ga_{0.70}As$ cap with various distances separating the Nb electrodes. (Right) Zoomed in on a particular device. The resistance is rising as the temperature is lowered, but at a much lower rate than seen in Figure 6.13; those InGaAs capped devices consisted of thicker semiconducting layers and had a normal reservoir to suppress pair correlations.

The raw RvT data is similarly shaped for trench lengths ranging from 150nm to 750nm, but it is not obvious at first glance there is also a length dependent effect. If a precursor to a supercurrent is coupling these two electrodes it would be expected that as the length separating the two electrodes is decreased by a factor of 5 the coupling would become stronger. This is checked by comparing the resistances of devices with differing lengths both just after the electrodes have become completely superconducting and at 4.2K. Since superconductivity is weak at T_c it does not affect the semiconductor, the resistance of the trench should just be proportional to the trench length. This will give us a good measure of the uniformity of the devices, and if reducing the temperature to 4k has a greater effect on the thinner devices this change should be obvious. However as can be seen in Figure 6.11, there is no substantial change in the distribution as the

temperature is reduced. In both cases the predicted value of the resistance at zero trench length is 28 Ohms. If there had been some sort of coupling the predicted value would have been reduced or the fit would have predicted that the measured resistance reaches zero for finite electrode spacing.

Differences between the thin and thicker semiconducting layers are also present when measurements are taken at finite bias. While the InGaAs interface devices with thick GaAs conduction channels exhibit reduced zero-bias conductance, the devices where the semiconducting layer only consists of a 200A thick InGaAs interface have a maximum in zero bias conductance. These devices have the same N-S junction transparency as the those with GaAs conduction channels. Unlike the highly conductive InAs interfaces, this

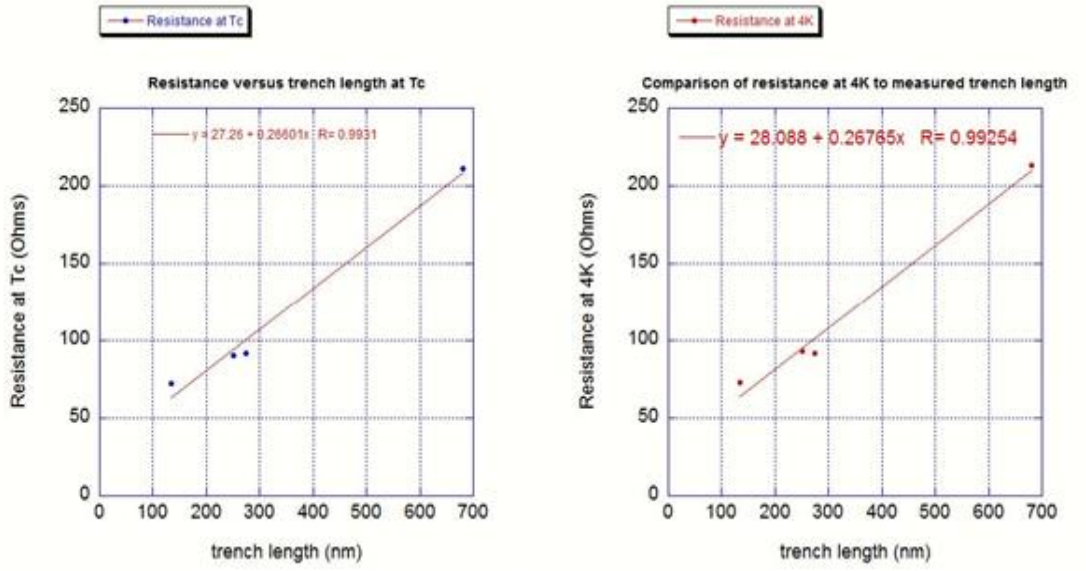

Figure 6.11: Resistance as a function of trench length for a semiconducting structure consisting of solely the 200A $In_{0.30}Ga_{0.70}As$ cap at T_c(Left) and at 4K (Right). If there had been coupling between the two electrodes, the differing distances between the electrodes would have caused the resistances to change relative to each other. The lack of change is indicative that this enhanced zero bias conductance is due to a local effect at N-S interface and is not because of coherent coupling between the electrodes

zero bias conductance maximum is not predicted by BTK theory due to the lower transmission coefficient of the interface. As the temperature is lowered, the conductance increases over a larger voltage range as seen in Figure 6.12.

This result is reminiscent of the interplay of the Thouless length and energy scales describing correlations in a diffusive conductor. When a normal electrode is in good contact with a superconductor, the energy spectrum at a distance L deviates from the normal state value up to the characteristic Thouless energy, $E_{Th} = \frac{\hbar D}{L^2}$. As the thickness of the semiconductor is reduced, correlations of increasing energy are able to diffuse throughout the entire structure before they suffer an inelastic scattering event and dephase from each other [16]. While this theory predicts that there will always be an alteration at a small enough energy for semiconducting structures of all sizes, our results in Figure 6.9 indicate that there is no change when the thickness is reduced from 2200A to 400A. However, when the thickness is reduced by an additional factor of two, the current voltage relationship changes completely; we do not just see the voltage scale of the interaction expanded by a factor of 4. This result implies that our results cannot be explained completely with a Thouless argument.

Another prediction of this theory is that the resistance of the semiconducting link should exhibit reentrance [47]. The sheet resistance of a normal wire linking superconducting and normal reservoirs will be identical at zero temperature and at T_c. The resistance reaches a minimum at the temperature when its physical size L is equal to the thermal length, $L_{Th} = \sqrt{\frac{\hbar D}{kT}}$, and increases in magnitude as the temperature is lowered further. The mean free paths in this project imply the thermal length will be on the order

of 1000A at 4K, corresponding to distances much larger than the 200A thick semiconducting layers at which a qualitative difference in the data occurs. Furthermore in all measured devices, R_s is monotonically increasing or decreasing and no reentrance is observed as the temperature is reduced and the thermal length becomes equal to the thickness of the semiconducting layer Both Thouless' and Nazarov's theories of the influence of the length on the proximity effect should be valid since the Thouless argument discusses how correlations disperse in a diffusive conductor and Nazarov's result discusses the interplay between the superconducting and normal reservoirs. A possible reason for this discrepancy is the relatively poor transparency of the InGaAs N-S interface, but a self consistent suppression of the superconductivity by the normal reservoir present in the thicker samples plays a more likely role.

The presence of the normal reservoir suppresses superconductivity in the interface region by supplying a $\theta = 0$ (no pairing) boundary condition to the quasiclassical equations that govern the proximity effect. If the semiconducting layer is sufficiently thin, the normal reservoir no longer exists in the semiconductor and the appropriate boundary condition is $\frac{d\theta}{dz} = 0$, just as in the problem studied by Belzig [17]. The strength of the pairing is determined solely by the coupling to the superconducting reservoir and in this thin limit we would expect Thouless' predictions for the length and energy dependence to hold true. In our results we see a discontinuous shift in the nature of the manifestation of the proximity effect as the N layer thickness exceeds 200A. This is due to the normal reservoir changing the nature of the problem and suppressing the pair correlations. Thouless' model cannot account for such a suppression.

When the 200A thick semiconducting layer with an InGaAs interface is measured using the 3 terminal device structure, the extracted G_c and R_s curves both exhibit differences as compared to the thicker semiconducting layers with identical interfaces. These results are similar to those extracted from devices with the far more transparent InAs interfaces. The raw data of these thin layers was almost indistinguishable from the other semiconducting structures, with typically shaped increases in the R_2 and R_3 curves. However when the device analysis of Appendix B was performed, a difference in the extracted quantities becomes apparent and can be seen in Figure 6.12. While the junction conductance decreased, it did so only slightly and with a far different slope than the thicker semiconducting structures. Figure 6.4 showed that when the thicker semiconducting layers were coupled to the InGaAs interfaces G_c was reduced by an order of magnitude as the temperature dropped from T_c to 4K. The $G_c(T)$ curve for the 200A thick structure is essentially flat. Additionally, the sheet resistance did not increase as it had on all wafers with InGaAs caps and thicker semiconducting layers. Instead, the sheet resistance slightly *decreased* as the temperature dropped. A qualitative difference has occurred when the semiconducting structure consists of just the InGaAs cap and is occurring in the semiconducting structure directly beneath the superconductor since it has no dependence on the electrode spacing.

If the InGaAs cap had pair correlations induced in it in this case, why was the signature of the same effect not seen in the other structures which contain the same cap? As was discussed earlier, we found that the presence of an additional 200 Angstroms of doped semiconductor instead of semi-insulating GaAs precluded superconductivity from penetrating into the semiconductor. The presence of this normal reservoir outside of the

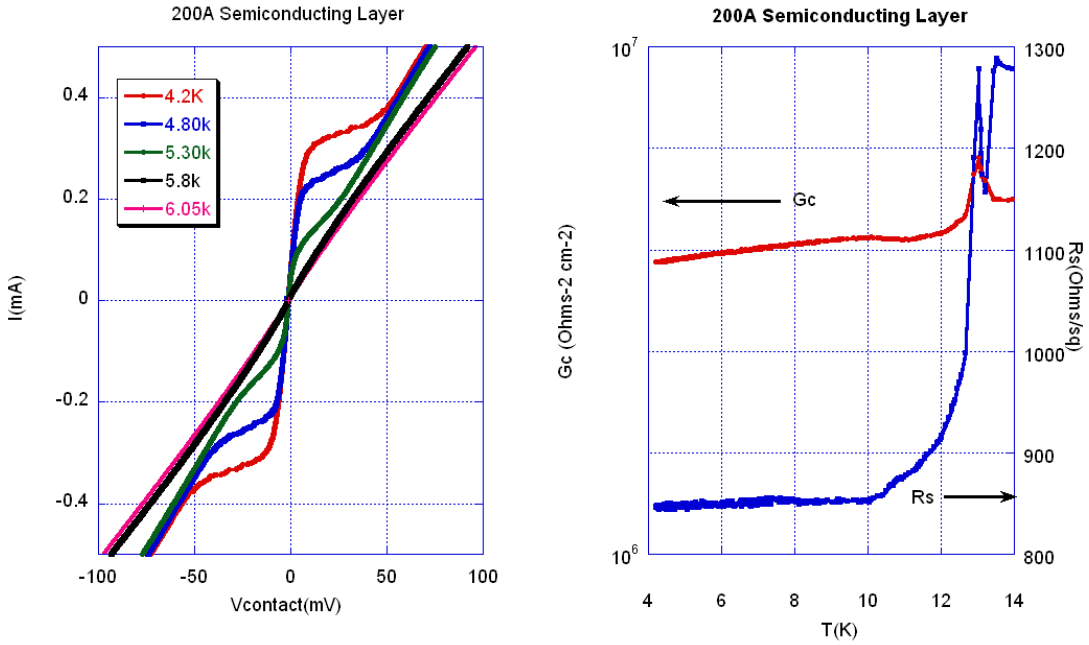

Figure 6.12: (Left) Current vs voltage plot for a thin trench device whose epitaxial structure consisted of solely the InGaAs cap. Note that in contrast to the other InGaAs cap samples that are coupled to GaAs channels this device exhibits a zero bias conductance maximum. (Right) Intrinsic junction conductance, G_c, and sheet resistance, R_s, for InGaAs cap only junction. Note that G_c drops only slightly and R_s is slightly decreasing in contrast to the samples with the doped GaAs channels.

proximity affected region, as was suggested in the discussion of Nazarov in section 2.4, is responsible for this effect. As we observe here, Nazarov claimed that the stronger the proximity coupled region was coupled to the normal reservoir, the weaker the net influence of the superconducting electrode. The extra 200 Angstroms of doped GaAs apparently acts as an anchor to keep the InGaAs cap firmly pinned in the normal state. However if it is removed, or presumably made thinner than 200 Angstroms, there is no longer a normal reservoir to couple to the interface region and keep it fully in the normal state and the signatures of pair correlations through a reduced R_s and the presence of a zero-bias conductance maximum are observed.

6.4 Conclusions and Open Questions

The measurements on the differing semiconducting structures span a wide variety of differing strengths of the proximity effect, but they can still be described coherently using the theoretical picture of Nazarov that was discussed in section 2.4. The almost perfectly transparent InAs interfaces, $|T|^2=0.73$, imply that the probability of Andreev reflection is high and the coupling across the N-S interface is strong. This coupling is strong enough that it induces pair correlations inside the semiconducting layer. These correlations are manifested by a decreasing sheet resistance in the proximity affected region, R_s, as the temperature is reduced. Additionally, a zero bias conductance maximum is measured.

However, semiconducting layers of similar thickness but with interfaces constructed of $In_{0.30}Ga_{0.70}As$ exhibit results that are different. As the InGaAs cap structure was optimized, the transmission coefficient increased to $|T|^2=0.04$, but the shape of the G_c and R_s curves remained identical. G_c continued to decline and R_s continued to increase as the temperature was lowered, both opposite to what is seen in the even more transparent InAs devices. All InGaAs capped devices whose thickness was greater than 200 Angstroms also had a zero bias conductance minimum. These results are very robust as these features are seen in every thick InGaAs capped device and InAs device. These results are not due to instabilities in our model. Appendix B shows that the qualitative result of G_c increasing or decreasing with reducing temperature does not change even for unreasonable choices of the model's geometrical and physical inputs. Furthermore, the discrepancy in the raw data between the two N-S interfaces is confirmed by the two terminal thin trench devices.

The key to understanding this discrepancy is the sample that had an identical $In_{0.30}Ga_{0.70}As$ interface but whose semiconducting layer was just 200 Angstroms thick. It had a differential conductance maximum at low bias, and a decreasing R_s as the temperature was reduced. These two aspects are similar to the InAs devices. Despite these features, the thin layers had the same $|T|^2$ as the thicker InGaAs interfaces. G_c also decreases when the semiconductor is thin, but it decreased at a much slower rate as compared to when the semiconductor is thicker. These results imply that the thin InGaAs samples are in a mixture of the two limiting cases.

As was discussed in section 2.4, in Nazarov's model of the proximity effect the strength of the coupling to superconductivity in the interface region will be proportional to the N-S contact conductance, and also inversely proportional to the conductance coupling the proximity affected region to the physically separate normal reservoir. When the semiconducting layer is thick, far from the N-S interface there exists a region that is not affected by superconductivity and which acts an effective normal reservoir. The thick $In_{0.30}Ga_{0.70}As$ capped samples do not have strong enough coupling between the proximity affected region and the superconductor to overcome the coupling to the normal reservoir at the base of the semiconducting layer. Therefore, the interface region remains pinned in the fully normal state. The InAs devices are thick enough that a normal reservoir should exist in them, too, but the N-S contact is so transparent that coupling to the superconducting reservoir overcomes the coupling to the normal reservoir, and pair correlations are induced. In the case of the thin semiconducting layer with an identical $In_{0.30}Ga_{0.70}As$ cap, the N-S interface is still inferior in conductance and transmission coefficient to the InAs-Nb interface, but its depth is so thin that a normal reservoir does

not develop and the interface region is not as tightly bound to the normal state as the thicker $In_{0.30}Ga_{0.70}As$ samples. The interface region is solely influenced by the superconducting electrode, and in this regime we would expect Thouless arguments on the energy and length dependence to be valid. Therefore pair correlations are induced in the interface region and the device exhibits a zero bias conductance maximum and a reduced sheet resistance R_s just as in the samples with the far more transparent InAs interface However, when the semiconducting layer becomes thicker the suppression of pair correlations due to the normal electrode imply that the nature of the interaction has changed and the Thouless model will not be valid.

Chapter 7 Conclusions

Theoretical predictions for the proximity effect indicate that the strength of the pair correlations in the semiconductor depends on both the N-S junction transparency and the strength of coupling to a normal reservoir [2, 16]. In this project our device design allows us to simultaneously tune both of these parameters. Adjusting the structure of the Indium based capping layers allows us to vary the transmission coefficient of the N-S junction to almost its theoretical limit, and adjusting the thickness of the semiconducting layers modifies the coupling to the normal reservoir.

The novel three terminal device geometry we've developed and used provides two independent voltage measurements which in combination allow us to extract the intrinsic N-S junction conductance, G_C, and the proximity affected sheet resistance in the semiconductor, R_S, and how these depend on temperature. This extracted conductance, in conjunction with our contact theory based upon Landauer's formalism of contacts, gives us a way to determine the "per-mode" transmission coefficient of the N-S system. This result can be used to understand the transparency of our interfaces and to optimize the InGaAs and InAs epitaxial structures. The transmission coefficient for the most transparent InGaAs capped device is $|T|^2=0.04$, while the Nb-InAs interface has a $|T|^2=0.73$. The conductance and transmission coefficient of these devices are the highest ever reported for a junction coupling Nb to InGaAs. We also used a band structure simulator [27] to evaluate the shape of the surface barrier (triangular) for the actual junctions architecture and by employing a simple WKB calculation we found good agreement with the measured transmission coefficient. We also found that changing this

architecture resulted in a decreased contact conductance, so apparently our devices are the most transparent N-S contact that can be fabricated using a 30% InGaAs cap layer. The Nb-InAs interfaces are even more transparent due to their lack of a Schottky barrier, and their transmission coefficient approaches the limit set only by the Fermi velocity mismatch between Nb and InAs.

Despite the relative perfection of the InGaAs to niobium interface, thick semiconducting layers exhibit no evidence that superconductivity is induced in the semiconductor. When the semiconductor layer is thick, semiconducting electrons that are sufficiently far from the N-S interface are apparently not affected by the presence of the superconductor and act as a normal reservoir. As was shown theoretically by Nazarov [2] and Gueron [17], the presence of such a normal reservoir acts to suppress superconductivity in the proximity affected region and pin it in the normal state. This suppression results a conductance minimum at low bias, and an exponentially falling G_c as the temperature is reduced below T_c. These results are consistent with the BTK theory for a Z=5 N-S junction.

However, if the doped semiconductor is made thin enough, 200 Angstroms in the case of the $In_{0.30}Ga_{0.70}As$-Nb interface, we find that a qualitative change occurs. The normal reservoir apparently no longer exists and the proximity affected region exhibits the presence of pair correlations. In the measurements, a low bias conductance maximum now exists, as well as a decreasing R_s with falling temperature. These results are the opposite of those seen in the thicker semiconducting layers.

These thinner samples have an identical N-S interface as those with thicker semiconducting layers, but they exhibit qualitatively different results. Since the

semiconductor is no longer thick enough to have a normal reservoir, the boundary condition on the substrate side of the interface region must no longer be fixed to be the normal state. The value of the pair amplitude is now allowed to freely float, and the interface region is only influenced by the superconducting electrode. Without a normal reservoir to pin the interface region in the normal state, we find that pair correlations develop even with the poorly transparent InGaAs N-S interface. Since only the superconducting electrode is influencing the interface region, we expect that the induced pairing obeys the Thouless theory of how correlations disperse in a diffusive conductor. However, when the semiconducting layers are made thicker, there is now an additional negative influence on the pairing due to the normal reservoir. The nature of the proximity effect changes discontinuously and the Thouless predictions for the length and energy dependence of the superconducting correlations do not apply. This abrupt change results in the qualitatively different behavior we have observed in these two regimes.

If the transmission coefficient is increased by using pure InAs, the results mirror what was seen for the thin InGaAs capped semiconducting layers. InAs does not form a Schottky barrier with Niobium, and since the Schottky barrier is the primary contributor to the remaining barrier, these devices contain extremely transparent interfaces. The transmission coefficient according to our Landauer formalism based theory is equal to $|T|^2 = 0.73$, almost at the theoretical limit for Fermi velocity mismatch limited interfaces. These devices exhibit different characteristics compared to the thick InGaAs devices, the resistance decreases with temperature, and the InAs devices have a zero bias conductance maximum. These findings are consistent with the prediction that due to the extremely high transparency of the Nb-InAs junction Andreev reflection has a high probability and

can easily transmit pair correlations across the N-S interface. The extremely transparent InAs devices are thick enough to have the presence of a normal reservoir. The difference is that the coupling through the InAs-Nb layer is strong enough that the processes leading to induced pair correlations can overcome the suppression of it by the normal state reservoir. While these devices do show an enhanced conductance which increases as the temperature falls, a full DC supercurrent never develops. The G(V) curves of differing devices can be collapsed onto each other by subtracting out the parasitic trench resistance of their differing widths. Additionally under the illumination of microwaves, Shapiro steps were not observed. This indicates that the enhanced zero bias conductance we observed as the temperature was lowered is apparently a local effect, happening just at the superconductor to semiconductor interface. The enhancement does not happen because of a coherent coupling between the two superconductors, rather it happens because of the local proximity effect at the interface.

It is possible that the lengths between the electrodes were too large for a true supercurrent to develop at the higher temperatures where these devices were measured. Another possibility is that since the InAs layers are more than 1000 Angstroms thick there is still too much normal material too strongly coupled to the proximity enhanced region. While this normal reservoir is not strong enough to completely suppress superconductivity, it could be enough to prevent the device from become fully superconducting. If the conducting channel could be made thinner, and the unintentionally doped region even less doped, the extremely high transmission coefficient of the interface might be sufficient to make the InAs fully superconducting.

7.1 Future Directions of Research

The success this project had in tuning the strength of the proximity effect in the semiconductor implies that this method of coupling can be expanded and used in meso-scale devices. Based on our device theory, the InGaAs capped devices have reached their practical limit. It can now be determined if their junction transparency is sufficient for coupling superconductivity to the uniquely transparent two dimensional electron gases developed by Stephanie Law [37] that are in the integer Quantum Hall edge states. If they are transparent enough, then it should be possible to probe the spectroscopy of the QHE states using the superconducting contacts, and validate a number of predictions regarding the ability of non-dissipative Quantum Hall edge states to carry a non-dissipative supercurrent made by Fisher [48]. If the InGaAs contacts are not transparent enough, then a new semiconducting epitaxial structure must be tried, as it will have been determined that even the best InGaAs contacts are of insufficiently transparent.

Another elaboration of this project would be to create a combination of the two types of devices that were studied in this project. The 3 terminal device geometry permits extraction of the intrinsic junction conductance and the sheet resistance of the N-S system. However, it is unable to determine how what effect the distance between the electrodes has on the intrinsic properties of the N-S system. The thin trench devices do have the ability to observe the effect of the size distance between the superconducting electrodes, but are limited to a lone measurement. This measurement by itself cannot determine the necessary information to fully understand the manifestation of the proximity effect. While attempts at creating these hybrid types of devices were made in this project, the *ad hoc* combination of several different processing steps was never successful. However, a

properly thought out and calibrated device process should be able to create these hybrid thin 3 terminal devices.

Based upon the positive effect on pair correlations that were observed when thinner GaAs layers are used, another possibility for increasing the pairing in the semiconducting layer would be to create very thin InAs layers. Unfortunately since the unintentionally doped InAs grown in our chamber is still relatively conducting, an improvement in the semiconductor growth would have to occur prior to the successful reduction of the normal reservoir. Another possibility would be to continue to attempt to use Indium based caps in conjunction with GaAs semiconducting layers. Since we are already at the upper limit of transmission using strained InGaAs, a new method of forming the capping layer would have to be used. One option to explore would be to create superlattices of GaAs/InAs that were sufficiently small in pitch that they could combine the high transparency of InAs but not allow strain to build until the surface fractured. This method, if it proves feasible, would greatly increase the conductivity of the contacts without the restriction of thick doped semiconducting layers.

Appendix A Growth of GaAs

Growing thin flims requires extreme precision and exacting techniques. The samples used in this project were grown using the techniques of Molecular Beam Epitaxy (MBE) and occurred in two chambers, the III-V chamber, System B, and the Niobium chamber, System E. Both were Perkin Elmer 430 MBE systems and while they were used for different purposes, the general technology of the two chambers is quite similar. The base pressure of the chambers with liquid nitrogen running through the cryoshrouds was 2.5×10^{-11} Torr for System B and 1.0×10^{-11} Torr for System E. The disparity in the base

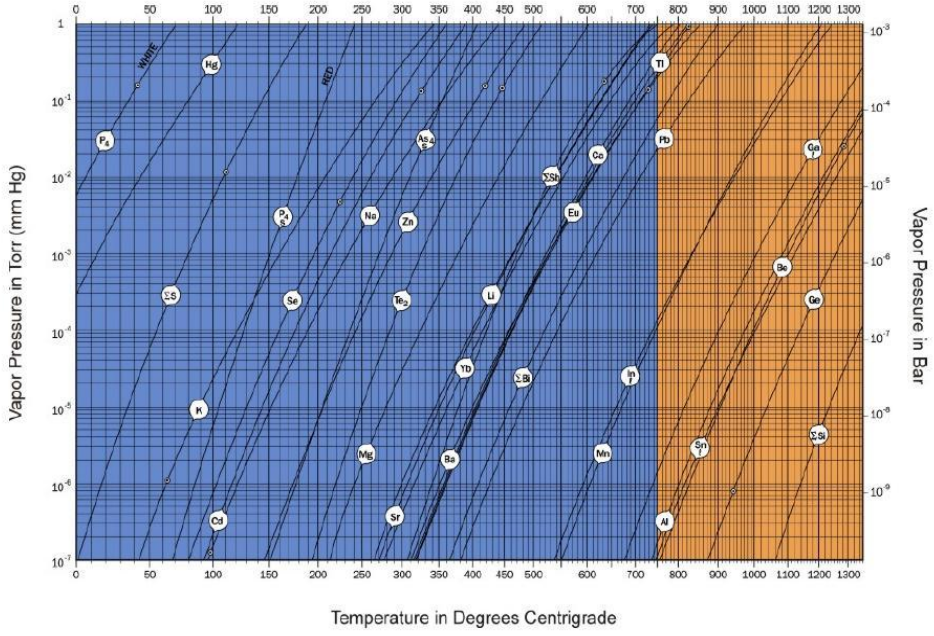

Figure A.1: Vapor Pressure curves for selected elements, note the wide range of temperatures required to achieve substantial partial pressures for Silicon and Arsenic. From Veeco[49]

pressures is due to the difference in materials deposited in them. High vapor pressure arsenic, though not harmful to the growth, constitutes the majority of the pressure in

System B while the natural gettering ability of the refractory metals used in the Nb chamber reduces its measured pressure. These systems are coupled by a UHV transfer tube, with base pressures less than $1x10^{-9}$ Torr allowing for completely *in situ* transfers.

A.1 Vapor Pressures

In the realm of vapor phase epitaxy with elemental solid or liquid sources, the vapor pressure of the material plays a crucial role. Governed by thermodynamics and statistical mechanics, at any given temperature, even below the boiling point, there will be a competition between the vapor phase and the liquid or solid phase of the material in question. Though each element or compound has its own unique curve, the favorability of the vapor phase is roughly exponentially increasing with temperature. An example of these curves can be seen in Figure A.1. The values, slopes, and relative positions of the vapor pressure curves underly many of the decisions that will have to be made in the growth of materials by MBE. They determine the temperatures at which materials are evaporated, the amount of damage impurities can cause and the amount and methods of cleanliness that are required.

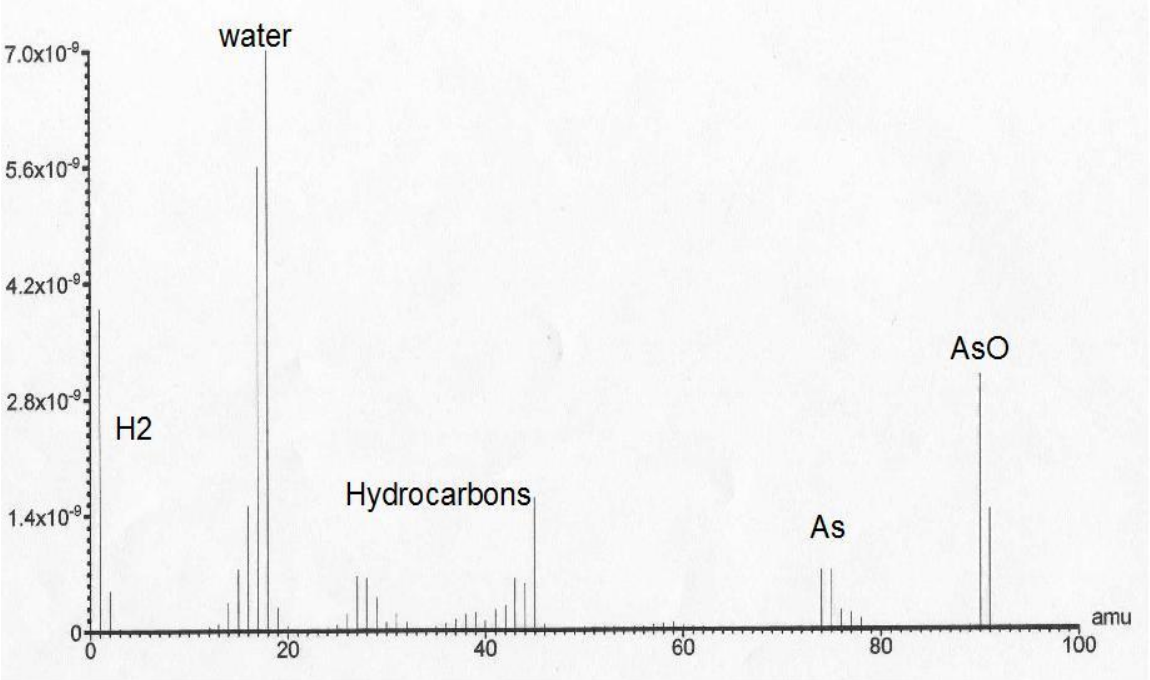

Figure A.2: Residual Gas Analyzer trace of the gases inside the chamber before baking. After baking, all mass/charge ratios greater than 4 will not be visible.

A.2 Growth Technology

Though the general principle of deposition is quite similar for both chambers, the actual techniques used are different. In order to deposit material on the substrate, the heating of sources, almost always elemental, until a substantial flux of vapor begins to be evaporated or sublimated from the surface is required. This flux-temperature relationship is broadly exponential as can be seen in A.1. However the temperature at which the substantial evaporation occurs can vary over thousands of degrees predicating a variety of different growth techniques which will be discussed throughout the chapter. Though the hot sources emit these evaporated atoms omni-directionally, the geometry of the furnaces, crucibles and chambers restrict the flow of atoms to being only incident on the sample. This reduces the total amount of source material used during the growth, and

additionally reduces the likelihood of cross contamination. While the atoms are initially evaporated towards the substrate, they also arrive unperturbed. According to kinetic theory the mean free path of an atom in the low pressure limit will be

$$l = \frac{kT}{\sqrt{2}\pi d^2 p} \tag{A.1}$$

where d is the diameter of the molecules and p is the pressure. At the base pressure of the chamber this expression indicates that the mean free path is thousands of kilometers. The growth pressure is considerably higher, and is approximately $1x10^{-6}$ Torr. However, this still implies that the molecules have mean free paths that are hundreds of meters in length. Therefore, since the pressure in the chambers are so low, the likelihood of the atoms colliding with any other atom and hybridizing is minuscule, and the flux of atoms is almost perfectly directional to whatever is within the sources' line of sight.

For solid or liquid source III-V applications the primary source of evaporation is the effusion cell, or Knudsen-cell. These cells consist of a crucible containing the appropriate source material, a heater filament with suitable heat shielding, and a thermocouple to allow for a feedback based control of the temperature. As the vapor pressure of a material is a function of its temperature, the temperature feedback is also a method for controlling the evaporated flux. While there exists many variations on effusion cells, for an equally large range of applications all of the cells used in this project consisted of this standard representative design. The crucibles holding the source material were fabricated out of Pyrolytic Boron Nitride (PBN). PBN was chosen due to its high purity, general unreactivity with the source material and to its stability up to the maximum necessary cell temperatures of 1250C. Above this temperature the crystalline structure of the crucible

begins to decompose and Nitrogen is emitted. Fortunately N_2 is unreactive with GaAs, and therefore the small amount of nitrogen that are unintentionally incident on the sample do not have a negative effect. Care does have to be made when dealing with elements such as Gallium or Aluminum since they chemically wet the walls of the crucible. This chemical bonding implies that when the elements pass through the liquid-solid phase transition the changes in the density of the source and the strength of the bonding can cause the crucible walls to crack. In order to minimize the potential for catastrophic failure, double walled PBN crucibles were used for these sources and once melted the source material was not allowed to re-solidify until the system was to be vented and the sources could be checked.

While all the sources used in the semiconductor chamber were of high enough vapor pressure that standard effusion cells could be used, the evaporation of Niobium was different. Since Nb only has fluxes suitable for growth at temperatures above 2500C, electron beam evaporation must be employed. In this technique a tungsten filament is heated to thermionically emit electrons. These electrons are then accelerated over a 10kV DC potential before impinging on the target sitting in a water cooled hearth. Typical emission currents run in the hundreds of mA implying that several kilowatts of power can be delivered locally to a region of the target. As direct rather than radiative heating is being employed, sufficient fluxes from even extremely high temperature materials such as Nb can be obtained.

A.3 System Preparation

Element	Manufacterer	Purity
Arsenic	Furukawa	99.999995%
Aluminum	United Mineral Corp.	99.9999%
Gallium	United Mineral Corp.	99.99999%
Indium	United Mineral Corp.	99.9999%
Silicon	Alfa Aesar	99.9999%

Table A.1 Table summarizing source material manufacturer and purity used in this project.

In contrast to metallic or insulating systems, the electronic density of semiconductors can be varied over many orders of magnitude by intentionally implanting impurities otherwise known as doping. The doping of GaAs can range from less than $1x10^{15}$ cm^{-3} to as high as $1x10^{19}$ cm^{-3}. The ability to reliably vary both the charge sign and density of the mobile carriers by as much as 4 orders of magnitude allows for the creation of much of modern electronics, but it also necessitates an extremely high level of cleanliness of the system, sample and source material. If one wants to control the doping at one part in 10 million, one must eliminate unintentional defects to an even higher level. The source material is all purchased at the highest commercial grades and is listed in Table A.1. The typical purity is of 6N or 99.9999 percent. Despite this high purity this still implies a defect level of 1 part in 1 million which would correspond to unintentional doping at

more than $1x10^{16}$ cm^{-3} just from the source material alone. Fortunately, proper outgassing of the sources allows us to preferentially eliminate the higher vapor pressure impurities and obtain even purer source materials.

In addition to any impurities that are present in the source material, it is also important to remove any gases that have adsorbed onto the walls of the chamber while it was vented and exposed to atmosphere. After the source material has been loaded into clean, fired crucibles, the cells are thoroughly outgassed at 100-150C above growth temperature to eliminate not only stray impurities that are still present in the source material, but also those impurities which might be on the crucibles, the surrounding flanges or any other component which can be subjected to high temperatures during the growth.

While low pressure is a useful measure of the level of impurities, the proper metric for determining the cleanliness of the system should be the partial pressures of the species of gas molecules that are harmful to the growth of the sample. For III-V semiconductors these represent most molecules containing oxygen, O_2, H_2O, CO_2, AsO and those containing carbon such as hydrocarbons. All of the gas species listed above have substantial vapor pressures at room temperature and are therefore quite damaging to the film growth as they have a high probability of being desorbed from the walls and being available to be incorporated into the sample. A residual gas analyzer spectrum of the chamber just after initial pump down can be seen in Figure A.2. In order for the system to be made into a growth ready state these gas species must be pumped out and removed from the system. Some of them, such as O_2, have a high enough vapor pressure that they will be pumped out in a timely manner without any additional measures. Unfortunately

others, water and Arsenic oxide in particular, are contained in particularly dangerous regime of the vapor pressure curves which is high enough to be an ongoing problem but too low to be pumped out readily at room temperature, the system must be baked.

Baking is a necessary component of the pump down cycle of all UHV systems and consists of increasing the temperature of the walls of the chamber in order to increase the outgassing rate of the walls while still maintaining pumping efficiency. Since the outgassing rate will be exponentially related to temperature, the effectiveness of the bake will be related to the ability to evenly heat the entire chamber to as high as possible temperature. If the temperature of the walls is too low, or the bake lasts for too short of time there will still be an unacceptable amount of impurities present on the walls. Also, it is crucial that the bake be done as evenly as possible. According to Pfeiffer [51], baking at 200C for 5 days will reduce the outgassing rate of stainless steel by a factor of 10,000. Therefore if a small percentage of the chamber is not fully heated it will dominate the outgassing spectrum after the bake is turned off despite the remainder of the chamber being quite clean.

The effectiveness of the bake is monitored by a combination of 8 strategically placed thermocouples and the residual gas analyzer. These allow us to monitor the heating across the chamber and also the spectrum of gases remaining in the chamber. The bake was continued until the partial pressures of the offending gases, especially arsenic oxide, was barely detectable. This involved the partial pressures of these harmful gas species falling 2-3 orders of magnitude which typically required a period of 10-14 days. After the bake has been turned off and the chamber has returned to room temperature there should no longer be any visible peaks on the residual gas analyzer corresponding to atomic

masses above that of helium. Since the amount of adsorbed gas and hence time that must be devoted to baking is proportional to the system's exposure to atmosphere, it is important to minimize exposure to oxygen and water vapor. This should be done by following proper UHV procedures such as but not limited to reducing time spent with the chamber at atmosphere and using dry nitrogen gas for venting and overpressurizing when forced to open the chamber.

After the bake has been concluded and the system is cooled to room temperature a pressure of $1x10^{-10}$ Torr should be present. Since this pressure is measured prior to the introduction of Arsenic, it will typically be the lowest pressure the chamber sees at room temperature during the entire growth campaign. After growth commences all surfaces inside the chamber will be freshly coated with elemental arsenic which by nature has a high enough vapor pressure to have a substantial outgassing rate at room temperature. This will result in system pressures ranging from $1x10^{-7}$ Torr directly after growth to the low $1x10^{-9}$ Torr range if no growths are performed for several weeks and the Arsenic has slowly been pumped out of the chamber. Despite the absolute pressure being much higher, it is important to note that the overall cleanliness of the chamber is the same or better as in the original $1x10^{-10}$ case immediately after baking since background elemental arsenic is not harmful to the growth of GaAs and the spectral weight of harmful gas species is the same or less as impurities are either pumped out, incorporated into the GaAs samples, or buried in the walls.

A.4 RHEED

Now that the chamber is fully prepared for growth the cells must be properly calibrated as to provide the proper fluxes. While all of the effusion cells have temperature control intrinsic in their design, the accuracy and precision of the thermocouples should always be considered suspect. While other forms of growth can use a quartz crystal monitor (QCM), the binary nature of the III-V structure requires us to make different measurements. III-V crystals are typically grown in the presence of a significant overpressure of one of the two elements; the QCM readings would be swamped by the high rates of the higher flux element without indicating the flux of the limiting reactant that actually governs the growth rate of the sample. Fortunately Reflection High Energy Electron Diffraction or RHEED coupled with a CCD camera detection system provided by K-space Associates can be used to determine the actual growth rates.

RHEED consists of an electron beam that impinges at a grazing angle to the substrate, diffracts, and the displays the resulting diffraction pattern on a phosphorescent screen. This pattern is then captured by the CCD camera, converted to a digital map and analyzed by the acquisition software. In this project RHEED was used in two primary ways, diffraction patterns were analyzed to monitor epitaxy and surface reconstruction, and intensity oscillations were used for calibrating growth rates and determining growth modes.

As in the electron beam evaporator, the electron beam is generated by thermionic emission from a hot filament. The electrons that pass through the Wehnelt cap and are then accelerated through a 10kV potential with electrostatic focusing plates emerge as a

well collimated beam of electrons with energy 10keV and a relatively narrow spread in momentum. Electrostatic deflection plates in the head of the gun in conjunction with the adjustable position of the manipulator arm allow for the beam impinge on the substrate at an extremely shallow angle of less than 2 degrees.

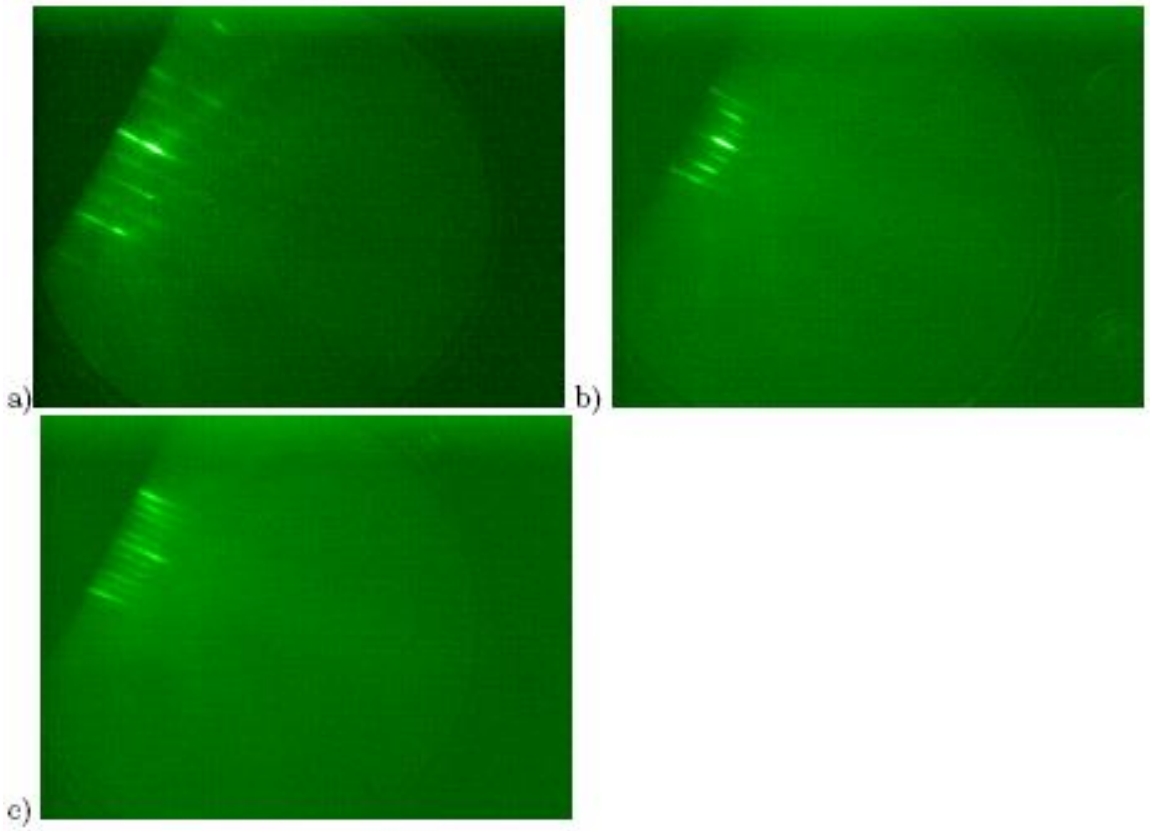

Figure A.3: Various RHEED reconstruction patterns: a)half b)third and c)quarter order reconstruction patterns

Since the incident electron beam is entering the substrate at such a grazing angle it only samples the top few layers of the crystal structure before exiting. This small sampling depth allows us to very precisely measure what is happening on the surface of the wafer. Though in the simplest case the diffraction pattern will merely show the reciprocal space map of the 3 dimensional crystal structure, III-V systems typically will show some more complicated surface reconstruction due to the position of bonding

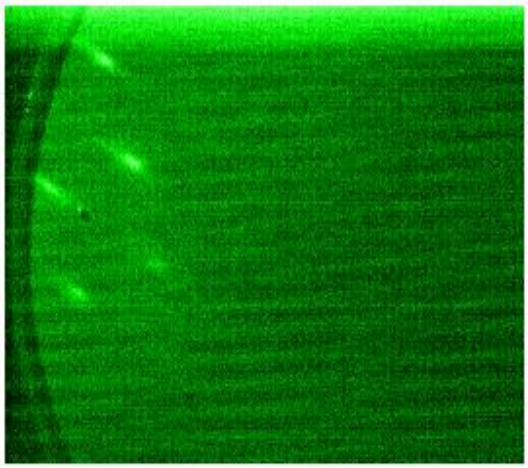

Figure A.4: RHEED pattern of a 3 dimensional surface, In addition to the 3 dimensionality notice the width of each of the individual features compared to Figure A.3.

hybridization at the surface. This reconstruction depends upon both the temperature and the ratio of the Group III and Group V elements and can be used to determine the quality of the surface.

The position, intensity and shape of the RHEED diffraction peaks displays vital information about the characteristics of the GaAs surface. The diffraction pattern is the result of simultaneously satisfying both momentum and energy conservation. As the RHEED pattern is primarily the result of single elastic collisions with the surface of the crystal, energy conservation can be represented as a sphere of size $\frac{\sqrt{2mE}}{\hbar}$ in reciprocal space. The corresponding momentum conservation relationship will be satisfied when the incident and diffracted k-vectors differ by a reciprocal lattice vector. In an infinite three dimensional crystal this momentum requirement will be represented by a lattice of points in K-space, whose intersection with the Ewald sphere would then be a pattern of dots. However, in two dimensions the spacing in the vertical dimension becomes effectively infinite and the momentum conservation instead becomes a series of rods extending in k-

space. In this case the intersection of these rods and the Ewald sphere will produce a series of streaks instead of points. The position and dimensions of these streaks will tell us important information about the surface. Since the relative two dimensionality of the surface will determine whether we are in the streak or spot limit we can characterize the flatness of the surface based on the length and uniformity of the observed diffraction pattern. The flatter the surface the sharper the streaks will be, while if the surface begins to become more 3 dimensional there will first start to become a superposition of streaks and spots resulting in a modulated RHEED structure and then finally a fully 3 dimensional structure as seen in Figure A.4. While the vertical size of the streaks tells us the variation in the vertical direction, the width of the streaks gives information on how flat the surface is. The flatter the surface the longer the periodicity is maintained, giving a larger number of potential momentum states and hence in reciprocal space the thinner the streak.

The geometry of the RHEED pattern tells us important information about the semiconductor surface as well because while all III-V semiconducting structures that were grown in the course of this project have zinc-blende crystal structures, they exhibit different surface reconstructions based upon what the particular growth conditions are. These growth conditions will define a particular type of hybridization on the surface of the crystal which is then visible in the RHEED pattern. In an arsenic rich growth mode at 600 C the GaAs surface has a 2x4 reconstruction [30]. Since the periodicity of the surface is 4 times the lattice constant along 1 axis and 2 times the lattice constant in the other axis the RHEED pattern in reciprocal space will have corresponding quarter and half order streaks as seen in Figure A.3.

While important information about the surface roughness can be seen from the shape of the RHEED pattern, it has also been shown [52, 53] that the quality of the GaAs surface can be understood from the relative intensities of these streaks, and that growth parameters such as III-V flux ratio, substrate temperature and absolute arsenic pressure can all be adjusted such that the growth conditions are maximized.

While the structure of the pattern can tell us important information about the crystalline nature of the surface, the intensity of the specular, or undiffracted, spot can be used to calibrate the growth fluxes of the various elements. As was described earlier, since the surface is Arsenic stabilized, the rate of deposition is completely dependent on the flux of the Group III element. After annealing for some time the mobility of the GaAs molecules on the surface will allow for the surface to become quite flat as the molecules move to form the lowest energy configuration. This flatness and hence long range order

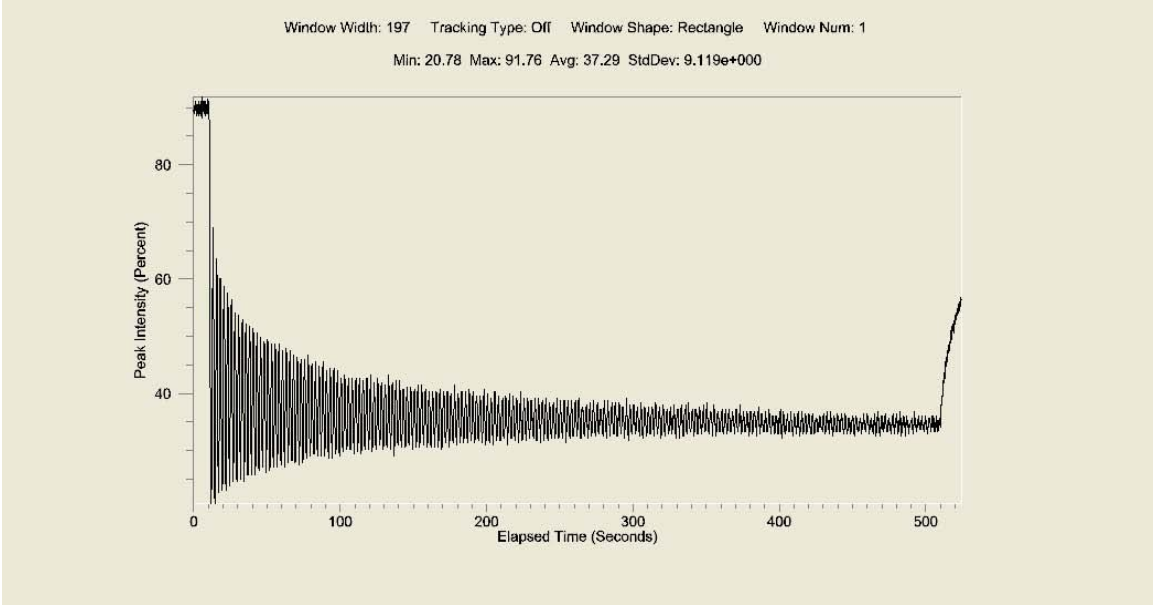

Figure A.5: RHEED oscillations captured by the analysis software. Each oscillation corresponds to the growth of one monolayer or 2.82 Angstroms. Note that the oscillations are still distinct after 500 seconds which at this growth rate is over 500A.

will be represented in K-space by a very tight range of momentums which result in a narrow, bright streak on the RHEED screen. When the shutter is opened atoms begin to be deposited on the surface. Since the periodicity of the surface has been disrupted the width of the streak will begin to increase lowering the maximum intensity. However, at some point more than half of the surface will be covered by fresh deposition meaning the maximum intensity will reach a minimum and begin to rebound. Because of the continued deposition of fresh material and the finite surface mobility of the atoms, the surface will never be as smooth as when the growth cycle was initiated, but a new maximum will be reached when maximum coverage is reached. The RHEED oscillations shown in Figure A.5 can be modeled as a damped sinusoid. The sinusoidal term represents the growth rate in monolayers and the damping term conveys important information about the growth mode of the system. Growth modes that are strongly layer by layer will exhibit oscillations that persist for hundreds of Angstroms. Conversely growth modes that reach a island growth mode steady state quickly rapidly damp to a constant RHEED intensity.

Growth conditions will determine which growth mode you are in, but the primary contribution will be due to the surface mobility of the atoms. This mobility is determined by the species of atom or molecule on the surface and the substrate temperature. In the characteristic case of GaAs and this is simplified to the relationship between the III-V ratio and the substrate temperature. As we have discussed before, at 600C the vapor pressure of Arsenic is very high, and its sticking coefficient on the substrate is effectively nil unless it encounters an unbound Ga atom on the surface. Alternatively, Gallium will have a very sticking coefficient at this temperature. Layer by layer growth is typified by

the incident atoms filling in the gaps in the previous layer prior to a new layer being formed. If the temperature is too low, or the flux is too high the Ga atoms do not have sufficient time or surface mobility to find the edge of the previous layer prior to binding to an Arsenic atom. Once Ga incorporates into a GaAs molecule the surface mobility of the molecule is reduced almost ensuring that the atom will not be able to fill in the vacancies in the previous layer. If the temperature is too high or the As flux is too low the Ga atoms have sufficient time to bond with another Ga atom prior to being bound to an As. These metallic Ga-Ga molecules have very poor side effects for good GaAs.

A.5 Dopant Calibration

The final step in properly calibrating the growth system is to calibrate the flux from the Silicon source which serves as the source of intentional doping in this project. As was discussed earlier, even the best GaAs has some unintentional doping but at low enough levels to be considered in most cases to be semi-insulating material. However, one of the most useful features of growth in semiconductors is the ability to adjust the level of mobile carriers by adjusting the number of intentionally placed impurities with differing electronic structure. As their name suggests, all III-V semiconducting compounds contain a group III element such as Gallium with three valence electrons and a Group V element such as Arsenic with five valence electrons. In the bulk these atoms form neutral compounds with a full valence shell. Instead if an atom with a differing number of valence electrons is inserted into the lattice the result is an extra electron, which is now donated to the lattice, or a lack of an electron, also called a hole. Of course since the donor or acceptor atom is electrically neutral an ionic core with the opposing chargee as the mobile carrier is also introduced, but the very small effective mass in GaAs, .066 m_e,

means that the bound radius of the donated electron is much larger than the interatomic spacing. This large radius means that neighboring carriers can overlap and the electrons can be treated as if they are effectively free. Due to the binary nature of the III-V system, the nature of the mobile carriers being electrons or holes is due to both the electronic structure of the impurities and the growth conditions of the sample. This has been extensively studied elsewhere so will restrict ourselves to just a simple outline. One example is Silicon, which is a Group IV element that we will substitutionally dope into our GaAs film. If the Si atom replaces a Ga atom it will donate an extra electron to the lattice. Conversely if it substitutes on the As site it will contribute a hole instead. However, the growth conditions that are used in this project with the large overpressure of Arsenic imply that Si will overwhelming prefer to substitute on the Ga site and each Si atom will contribute on average an electron to the lattice. As the concentration of Si atoms increases, it becomes less and less preferable for the Si atoms to substitute on the Ga site, and the average effective charge each Si atom contributes on average to the lattice drops. This is known as the amphoteric limit, and in our growth conditions is typically about $6x10^{18}$ cm^{-2}. Above this limit you are contributing to the disorder in the semiconductor by adding additional ionic cores and impurities, but are no longer increasing the number of free electrons as rapidly.

Despite the Si atoms substituting on the Ga site, and increasing the growth rate of our films slightly, since the highest flux we can achieve is still on the order of $1/10000^{th}$ of the Ga flux. Hence, we are unable to measure the flux of the Si *in situ* using the RHEED oscillation method described above. Instead several bulk doped calibration films must be grown, and their Hall resistance [44] measured using a 4500 Gauss magnet. As long as

we were below the amphoteric limit, the number of donors will be very closely related to the Si flux, and we can then interpolate to any flux using the exponential approximation to the vapor pressure curves. This method is quite repeatable and quite stable with drifts of less than 5% over many months.

A.6 Preparation for Device Film

Now that all of the fluxes of the elemental sources are knowm, we are now ready to grow an actual device structure. This process consists of several distinct parts, the preparation of the wafer prior to being placed into the chamber, the preparation of the sample surface inside the chamber to create the best possible surface for growth, and the actual device section of the sample. The device film is described in section 5.1, while the preparation will be described below.

A.6.1 Wafer Preparation

All wafers in this project were grown on quarters of 2 inch GaAs wafers obtained from AXT. Though the wafers were classified as EPI ready it was found [4] that the initial surface flatness was improved by first degreasing in acetone and isoproponal followed by an etch in 10:1:1 H_2SO_4 : H_2O : H_2O_2 and finally rinsing in deionized water. The acid etch not only cleaned the surface of any organic residue, but it also acted as a flattening etch on the substrate. It should be noted that the flattening of the acid etch is strongly related to temperature, with higher temperatures of the acid bath resulting in rougher surfaces. Since the mixture is very exothermic, care should be taken to properly cool the acid bath prior to use. In this project the beaker containing the acid mixture was placed in a bath of room temperature water for 15 minutes to allow it to cool. After

cleaning, the wafer was mounted in a custom open backed Molybdenum puck and held down by Mo wires. It was then placed in the load lock for to begin the transit to the growth chamber.

The load lock was roughed out by commercial pumping station consisting of a diaphragm pump coupled to a turbomolecular pump. After 45 minutes the load lock would be at a pressure of less than $1x10^{-5}$ Torr, and the load lock would then be crossed over to its integrated cryo pump. After an additional 30 minutes the load lock pressure would be less than $1x10^{-7}$ Torr and the sample could be transferred down into the UHV transfer tube. This transfer tube is pumped by an ion pump and has a base pressure less than $1x10^{-9}$ Torr. It provides an extremely clean method for transferring samples between the different MBE chambers. Despite the low pressure in the transfer tube and all the efforts at cleanliness, both the sample and the puck in which it sits are covered in several monolayers of adsorbed water from their time spent in the atmosphere. Though this water will evaporate slowly at room temperature, it will evaporate rapidly when the sample is heated in the growth chamber if not been removed prior to growth. As water has negative effects on the ability to grow extremely pure samples, the substrate is heated in the transfer tube to desorb the water into the walls and pump of the transfer tube and preserve the cleanliness of the chamber. Unfortunately the sample cannot be heated to growth temperature without significant outgassing of Arsenic from the lattice and causing increased surface roughness. This restriction puts an upper limit to the maximum temperature we can outgas in the tube of about 350C. Higher temperatures will result in significantly worse initial RHEED patterns [4]. However, in practice this temperature limit just forces an increase in outgassing time. The sample is outgassed in the tube

typically overnight with the recorded pressure with the substrate hot falling from $2x10^{-8}$ Torr back to the base pressure of $1x10^{-9}$ Torr the following morning.

A.6.2 Chamber Preparation

The pressure in the chamber depends upon when a sample was most recently grown. Due to the high vapor pressure of Arsenic and the large overpressure required to grow good semi-conducting films the room temperature pressure can be quite high. However, this is solely due to the high Arsenic background and should not be viewed as a measure of how clean the chamber is. Once the sample is loaded the liquid nitrogen is allowed to flow though the cryoshrouds which causes the walls of the chamber to cool. The shrouds cover the sides, source flange and bottom of the chamber and serve a two fold purpose. They are designed to increase the pumping speed of the chamber by trapping additional gas molecules on the walls. This occurs since the vapor pressure many elements falls by many orders of magnitude as the temperature is reduced from room temperature to 77K. The active cooling of the walls also prevented them from being radiatively heated by the substrate or cells and outgassing. This low temperature also ensured that all incident particles to the substrate were the result of zeroth order processes. No atoms could first strike the walls, hybridize in some fashion and then desorb and land on the substrate. As the walls cool their stickiness to the various gas elements increases and the pressure in the chamber rapidly approaches $1x10^{-10}$ Torr. After the walls are cool and lower vapor pressure materials have already been temporarily pumped out of the system the Titanium sublimation pump is activated. This pump consists of a titanium filament surrounded by a shield. When current flows through the filament it heats due to Ohmic loss, and rises to a

temperature high enough to evaporate a few monolayers of Titanium onto the shield surrounding the filament. These titanium atoms form a very reactive surface which will chemically bond to any volatile gas species left in the chamber. These volatile species, such as oxygen or carbon dioxide, have sufficiently high enough vapor pressures that they are almost unaffected by the cryoshrouds being at 77K. However, they will readily form lower vapor pressure compounds such as TiO2 with the activated Ti surface and therefore are effectively removed from the system. The sublimation source could have been run without first having the cryo-shrouds cold, but its effectiveness would have been greatly reduced due to the majority of the gas species reacting with the surface being the less volatile Arsenic atoms. Using the sublimation source in this fashion to only pump the higher vapor pressure elements greatly improves the final pressure of the chamber. This final pumping step reduces the pressure by a factor of two within minutes and the chamber finally reaches its typical base pressure of 5×10^{-11} Torr.

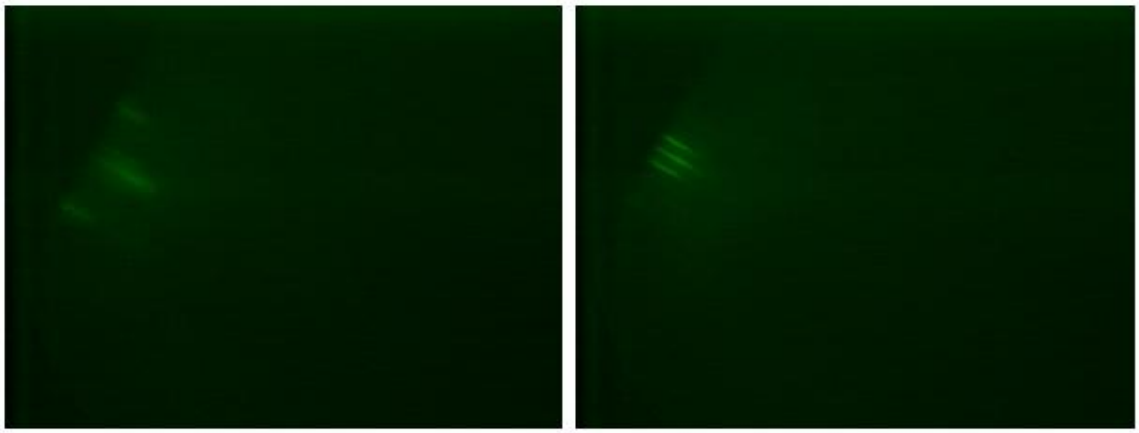

Figure A.6: RHEED images as the oxide blows off, and then after roughly 50 Angstroms of GaAs flatten the surface.

The next step in the growth process is to heat the cells from their idle positions to near their growth temperatures. The objective of doing this well before the actual beginning of the growth is again two-fold. First it is important that all surfaces on the source flange are thoroughly outgassed prior to the sample being raised into the growth position. All undesirable but sufficiently volatile elements are deposited safely on the 77K back wall of the chamber instead. Secondly there takes a finite amount of time for the source material to fully equilibrate with the thermocouple. This is particularly pronounced in the Arsenic sources which have the unfortunate combination of large volumes of source material and low operating temperatures. The large volume increases the heat capacity of the charge, and its difficulty in reaching equilibrium. Furthermore, since the temperature response will be related to the thermal radiation which goes as T^4 the lower target temperatures of the Arsenic cells delay this equilibration further. All the furnaces are fully controlled by temperature controllers set to the appropriate PID parameters. The cells are allowed to equilibrate for roughly one hour prior to proceeding.

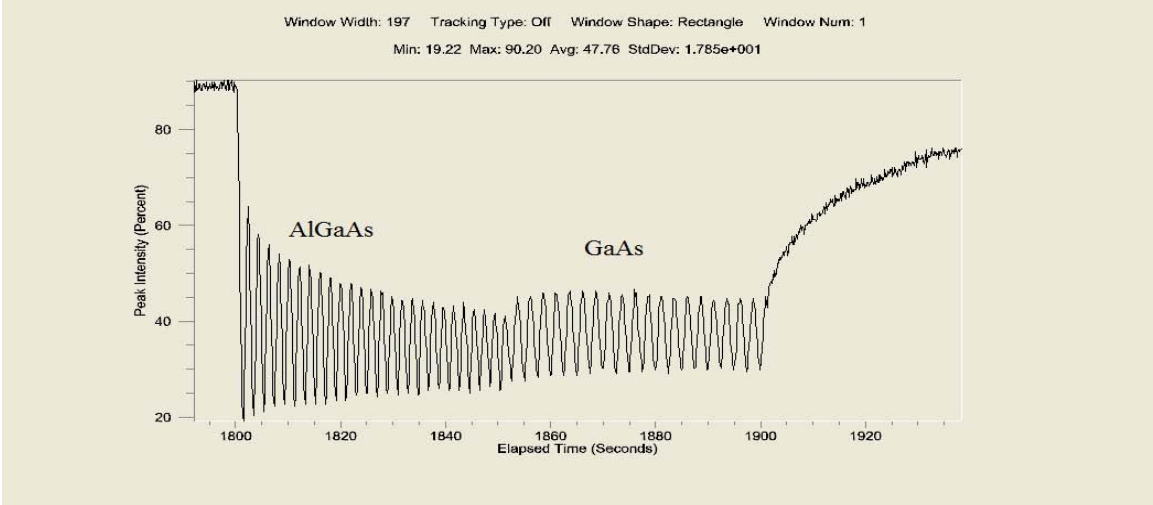

Figure A.7: RHEED oscillations depicting growth of AlGaAs SL. Impurities are trapped at the interface between the two different growths. Note the difference in growth rate between the two sections, the different oscillation rates can be used to calibrate the flux of the different furnaces

A.6.3 Growth Preparation

The next goal is to prepare the surface of the wafer for the best possible film growth. The first step is to remove the native oxide barrier from the surface of the substrate. This is accomplished by heating the GaAs surface in the presence of an Arsenic flux. At the elevated temperatures used in this project, 615C, an appreciable amount of Arsenic vapor and Gallium liquid will be evaporated out of the crystal structure. In order to prevent Arsenic vacancies this Arsenic beam flux is necessary to fill in any missing sites in the lattice and also to react with the temporarily unbound Gallium atoms. Despite having solely an incident Arsenic flux, we do not need to worry about metallic arsenic forming on the surface since the lifetime of elemental Arsenic on the surface of the substrate is measured in microseconds and hence the As atoms will only stick if they are incident on an available site in the lattice. The As flux can be calibrated using a beam flux gauge and has roughly a beam equivalent pressure of 5×10^{-6} at the substrate. As the temperature is

increasing, the sample is positioned in the Arsenic flux and the RHEED setup is activated. Below the oxide blowoff temperature a diffusive RHEED pattern is observed as seen in Figure A.6 as we are just imaging the top few monolayers of amorphous arsenic oxide. As the temperature rises through 600C as measured by an infrared pyrometer through a viewport, the oxide layer begins to desorb from the surface and a crystalline RHEED pattern emerges. Despite being shuttered, the viewports become coated with Arsenic over time which interferes with the ability of the pyrometer to accurately measure temperature. As the oxide blowoff temperature is a consistent calibration of temperature it is useful to note its value as a reference to all future temperatures during that growth. Once the oxide has been blown off, RHEED can be used to make the first measurement of the crystallinity of the sample. If the substrate preparation has been done properly it should consist of two dimensional streaks, but even if the surface is not perfectly flat the surface can typically be fixed during the flattening sections of the growth.

Despite the previous efforts to have the surface as flat as can be prior to growth, the next step will be to grow a large number of buffering layers. While in principle the device section of the growth could be deposited directly on the unconditioned substrate, it is common lore that for the best results up to one micron of material should be grown on the surface prior to the actual device section of the film [51]. The first step in these buffer layers is just flattening sections of GaAs. By continually dosing the surface with Ga, and letting it anneal and flatten the smoothness of the surface can be greatly increased. After typically 500 Angstroms of GaAs the surface is smooth enough and the RHEED oscillations are pronounced enough that they can be easily measured and the Aluminum

Gallium Arsenide-Gallium Arsenide superlattices as seen in Figure A.7 may begin. The ability to easily substitute Al for Ga in III-V semiconductors is the basis for a tremendous variety of devices that allow the ability to explore the most fundamental physics questions involving the integer [35] and fractional [36] quantum Hall effect to allowing ubiquitous solid state electronics components such as MODFETS. In addition to having a much different band gap, Al is a much more reactive atom than Ga. In general impurities ride the growth front and are continually substituted by Ga or As atoms, but an impurity that is bonded to an Al atom is slightly less likely to allow itself to be substituted than if it is bonded to a Ga atom. Therefore, by cycling between the layers of GaAs and AlGaAs it is possible to segregate impurities at these interfaces. Typically 50 of these AlGaAs-GaAs superlattices are grown, with the goal of further increasing the quality of the film.

During these flattening layers and the superlattices the flux of Ga and Al can be rechecked and an optimal III-V ratio can be found. Finally a large buffer of GaAs is grown to insulate the device part of the film from whatever impurities you have trapped below and the distortion to the band structure caused by the presence of the Al below. Three to five thousand Angstroms of GaAs are grown with plenty of annealing to maintain the excellent growth mode. This GaAs also served to continue to flatten out the surface until the highest quality surface was obtained. The growth characteristics such as substrate temperature and Arsenic flux would be modified until sufficiently high quality material was obtained. The metric for determining this was the quality and length of the RHEED oscillations of a specular spot in the (011) crystalline direction. In order to proceed these oscillations had to exceed a minimum value corresponding to at least 200 Angstroms and preferably greater 300 Angstroms of freshly grown material before

having to anneal and recover the surface. In the best samples the oscillations would persist for growths exceeding 500 Angstroms between anneals as was seen in Figure A.5. These oscillations are a good measure of the growth since they indicate how much of the growth mode is a layer by layer process. The identification of this growth mode is very important since we are interested in accurately placing the heterojunctions, not having interfaces diffuse across many monolayers. Once the surface and growth has been suitably maximized the device film sections of the growth described in Chapter 5 are begun.

Appendix B 3 Terminal Device Model

B.1 Extracting G_c and R_s

Two independent measurements are required to separate out the intrinsic quantities that govern the proximity effect, the sheet resistance in the proximity affected region, R_s, and the junction conductance across the normal-superconducting interface, G_c. However, each of the two measurements, R_2 and R_3, involve a convolution of both of these intrinsic quantities. Figure B.1 shows a scale drawing of a cross-sectional view of the injector finger. Below the critical temperature of the Niobium, the injector finger is superconducting and is an equipotential at DC. Since it is an equipotential, no current will flow laterally inside the injector finger; it will only flow vertically across the N-S interface. However, once in the semiconductor all the current will flow laterally towards the drain electrode off the page to the left, with no current flowing towards the upstream voltage contact on the right hand side. Notice that the aspect ratio between the width of the superconducting electrode and the depth of the conducting GaAs is large. This aspect ratio of 5-20:1 means that local dynamics can be assumed in this system and this situation can be reduced to two coupled one dimensional problems. One is in the transport across the N-S boundary, and the other is of the transport in the proximity affected region in the semiconductor.

Since there is no current flowing toward the upstream contact there will be no voltage difference between the upstream side of the semiconductor beneath the injector finger and the upstream electrode. However, this does not imply that the voltage difference

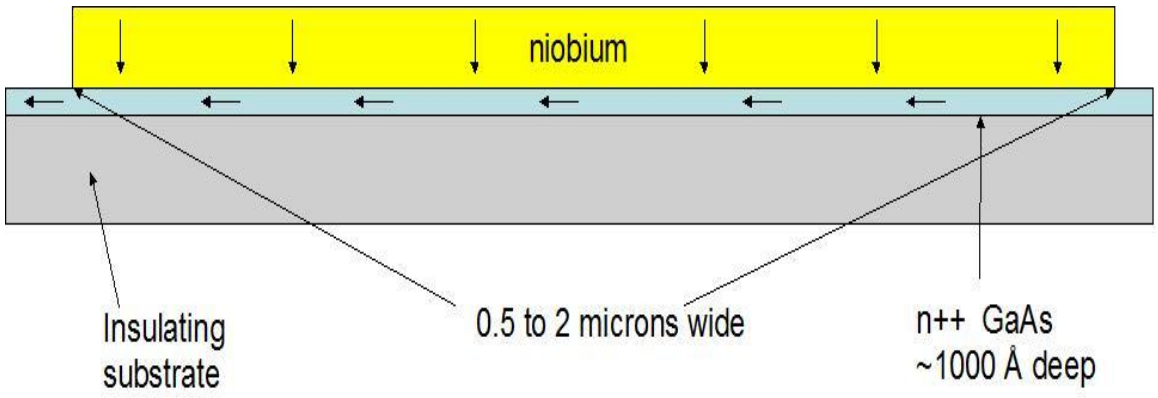

Figure B.1: Scale diagram of the cross section of the injector finger. Since the aspect ratio is so large, the problem can be effectively reduced to a 1 dimensional transport problem across the N-S interface, and a 1 dimensional transport problem inside the semiconductor.

between the injector finger and the upstream electrode is zero. As long as the injector finger is small enough, there will be a finite amount of current density traversing the upstream edge of N-S interface. This interface has its own intrinsic finite junction conductance and will have a measurable voltage drop referenced to the equipotential of the injector finger's superconducting electrode. However, the current density at the upstream edge depends upon not only the total current and geometrical size of the junction, but also the junction conductance and sheet resistance. These two intrinsic quantities determine the current and voltage profiles beneath the injector finger and if we can independently determine the profiles we are able to extract these intrinsic quantities.

As it turns out, this situation closely parallels a well known phenomenon in semiconductor-metal junctions called the transmission line problem [31]. This situation occurs when current is flowing between a bilayer of two different materials with sheet resistances different enough that voltage losses due to current flow in the lower resistance metal can be safely ignored and can assumed to be essentially an equipotential. The

current density profile in the semiconductor depends upon the contact resistance between the two layers, and the sheet resistance inside the lossy material. It is easy to understand the interplay between these two quantities if we imagine the two limiting cases of the sheet resistance being much larger or smaller than the corresponding contact resistance. In both cases the current will arrange itself such that it minimizes the total energy loss in traversing the entire system. Since the low resistance material is considered to be at an equipotential the current will arrange itself with regard only to the losses in the junction and through the lossy material. In the limiting case where the specific junction resistance is far greater than the sheet resistance the current profile will be as uniform as possible across the junction in order to maximize the effective area. This will happen at the expense of increasing the distance that must be traveled in the lossy region with its relatively negligible resistance. Conversely, in the case where the sheet resistance is much larger than the contact resistance the current will all crowd on the downstream side of the injector finger. In this case the current is sacrificing effective junction area in order to minimize the energy loss associated with traveling in the high resistance lossy material. In this limiting case it is well known that the effective size of this current contact will be the width times the transfer length $\lambda = \sqrt{\frac{R_c}{R_s}} = \frac{1}{\sqrt{G_c R_s}}$ where R_c and G_c are the specific contact resistance and conductance in either Ωcm^2 or Scm^{-2} and R_s is the two dimensional sheet resistance in the lossy material in Ohms per square.

In order to understand the actual measurements of our devices it is important to rigorously solve the current and voltage profiles beneath the injector finger. This model was solved in conjunction with Soren Flexner and first appeared in reference [4]. Let us

consider the case where shown in Figure B.2, where the Nb is superconducting and therefore an equipotential. As discussed earlier, the right hand side of the injector finger, V(L) is equal to the measured upstream voltage V_3. If we look at a point underneath the injector finger a small distance x downstream, its potential will be

$$V(x) = V(L) - R_s \int_x^L K(x')dx' \tag{B.1}$$

where K is the sheet current density and R_s is the sheet resistance beneath the injector finger. The next question to ask is what composes the sheet current, and since current is conserved it is merely the sum of all of the current densities traversing the N-S boundary upstream of that point x.

$$V(x) = V(L) - wR_s \int_x^L dx' \int_{x'}^L J(V(x''))dx'' \tag{B.2}$$

If we are in the linear response regime we can rewrite the current density,

$$J(V(x)) = G_c V(x), \tag{B.3}$$

in terms of the junction conductance and local voltage. Placing this result back into equation B.2 gives the expression

$$V(x) = V(L) - wR_s G_c \int_x^L dx' \int_x^L V(x'')dx'' \tag{B.4}$$

This expression can be reduced to a single integral equation by a theorem in [50] to

$$V(x) = V(L) - wR_s G_c \int_x^L (t - x)V(t). \tag{B.5}$$

Notice that this expression for the voltage profile depends only on the intrinsic physical quantities we are interested in, G_c and R_s, and the physical dimensions of the contact *w* and *L*. This Volterra equation can be solved analytically in this low bias case to give the general solution

$$V(x) = Ae^{x/\lambda} + Be^{-x/\lambda}. \qquad \text{(B.6)}$$

We can solve this equation with the appropriate boundary conditions. Beneath the

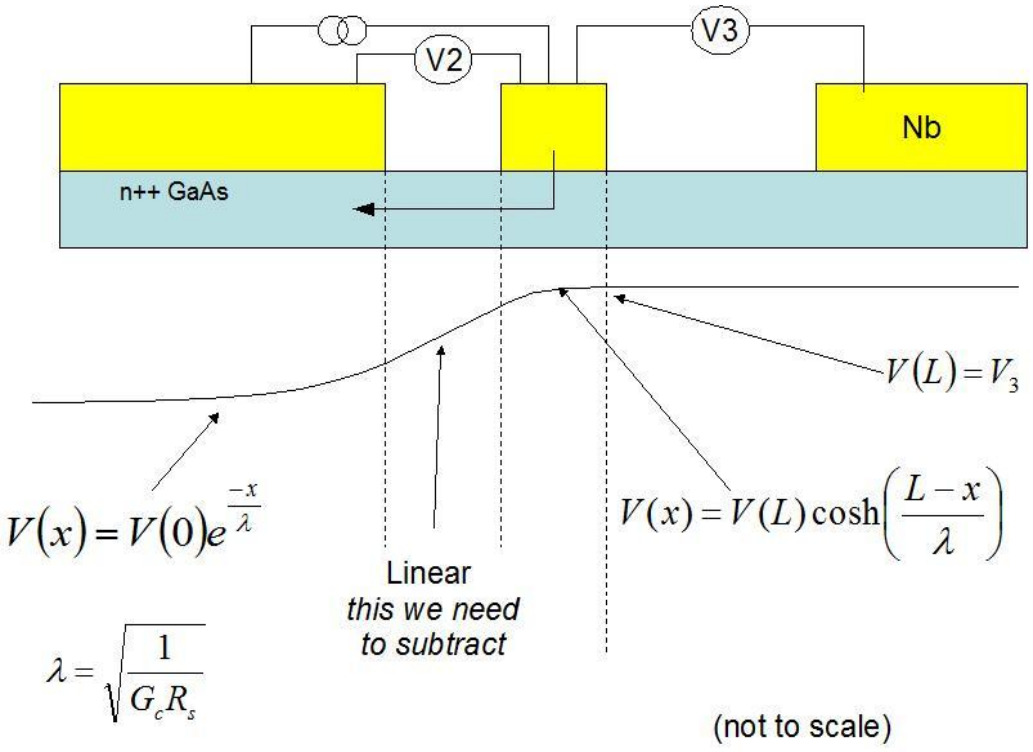

Figure B.2: Schematic of the 3 Terminal device voltage profile in the semiconductor. Current flows between the central injector finger and the downstream drain electrode on the left side. Since no current flows between the injector and the upstream contact there is no change in the voltage. Beneath the injector finger the voltage profile will be a cosh function, between the injector and the drain there will Ohmic resistance and the voltage profile will be linear. Underneath the drain electrode the voltage will be exponentially decaying.

drain electrode the length of the contact is hundreds of microns long, many times the transfer length, and is in the long junction limit. In order for the total voltage to be finite,

the voltage must go to zero for large values of x. Therefore, this boundary condition will give us an exponential dependence to the voltage profile beneath the downstream electrode

$$V(x) = V(0)e^{-x/\lambda}. \tag{B.7}$$

Conversely, the injector finger has been designed such that the size of the contact is comparable to a transfer length. In this situation, the appropriate boundary condition comes from the requirement that no current flows in the upstream direction. Because of this lack of current, the slope of the voltage profile must be equal to zero at this upstream edge of the injector finger. Therefore, the voltage profile takes on the form

$$V(x) = V(L)\cosh\left(\frac{x-L}{\lambda}\right). \tag{B.8}$$

V(L) is identical to V_3,

$$V(x) = V_3\cosh\left(\frac{x-L}{\lambda}\right). \tag{B.9}$$

Since the measured value V_3 differs by $\cosh\left(\frac{L}{\lambda}\right)$ from the downstream side of the electrode it is vital that the size of the contact be comparable to the transfer length. Figure B.3 shows the rate at which cosh increases as the ratio of the physical length to transfer length increases. While a ratio of 3 between the length and the transfer length only causes a distortion of a factor of 10 between the sides of the injector finger, if the ratio is increased to 5 then the downstream end of the electrode is now close to 80 times greater in magnitude. In addition to reducing the signal to noise ratio, in order to maintain the linear response regime small measurement currents are required which makes measuring

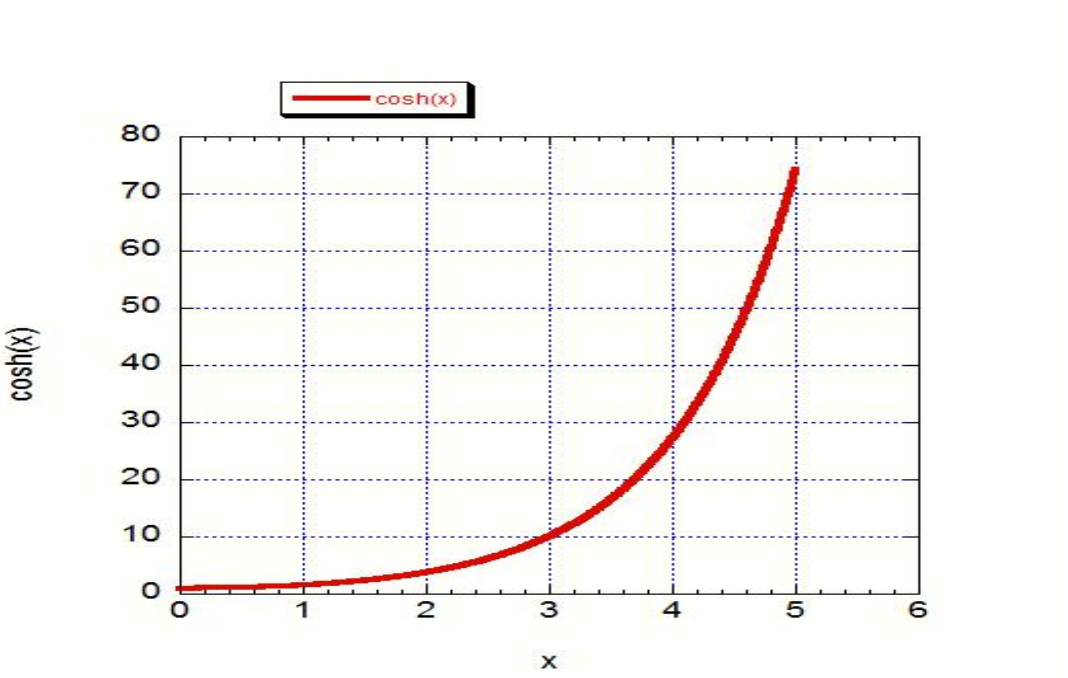

Figure B.3: Cosh of x, this illustrates the importance of having contacts that are comparable to the transfer length. Contacts that are too wide will rapidly have an extremely nonuniform current density, and have very small measured upstream voltages.

the upstream voltage vanishingly small in case when the transfer length is much smaller than the size of the contact.

Another measured quantity is the current which is found by integrating the current density J(x)= G_cV (x) over the entire contact which giving

$$I = \int_0^L V(x) = V_3 w \cosh\left(\frac{x-L}{\lambda}\right) = V_3 \lambda w \sinh\left(\frac{l}{\lambda}\right) \qquad \text{(B.10)}$$

We can construct the final measured quantity, V_2, by summing up its three components, the injector finger, the voltage drop due to the parasitic resistance of the semiconducting gap and the drain electrode. Since we already know the voltage profile underneath the injector finger, the voltage drop across this portion will be the voltage on

the downstream side of the electrode, $V_3 \cosh\left(\frac{L}{\lambda}\right)$. Since the distance between the electrodes, on the order of 5 microns, is much larger than any of the superconducting length scales, this gap will just contribute an Ohmic contribution to the total measurement. This contribution will depend on the geometrical width *w*, the distance between the electrodes *d* as well as the unaffected sheet resistance of the semiconductor R_{s_0}. By Ohm's Law it will be equal to $IR_{s_0}\frac{d}{w}$. The drain electrode's contribution will be the full height of the exponential V(0). This can be found by equating the currents and will depend on the size of the effective contact, the width of the device times the transfer length, and the specific junction conductance in Siemens per unit area.

$$V(0) = \frac{I}{G_c w \lambda} \tag{B.11}$$

If all these voltages are divided by the current we are left with the final expression for the measured resistance

$$R_2 = R_3 \cosh\left(\frac{L}{\lambda}\right) + \frac{R_{s_0} d}{w} + \frac{1}{G_c w \lambda} \tag{B.12}$$

Since it will not be a function of temperature, for the sake of convenience we can move the parasitic semiconducting gap resistance to the left hand side and define a new quantity.

$$\tilde{R}_2 = R_2 - \frac{R_{s_0} d}{w} = R_3 \cosh\left(\frac{L}{\lambda}\right) + \frac{1}{G_c w \lambda}. \tag{B.13}$$

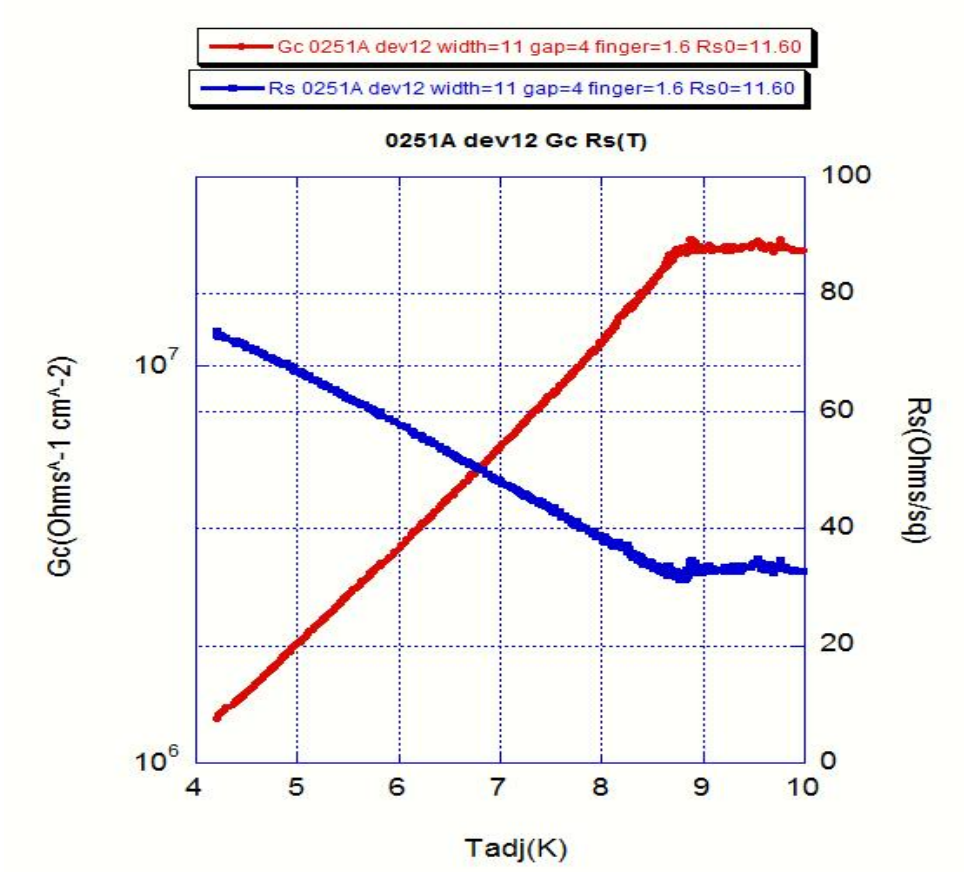

Figure B.4: Extracted data for the junction conductance G_c and the sheet resistance under the injector finger R_s as a function of temperature for a 3 Terminal device.

Now we have equations that relate the measured quantities in terms of the intrinsic quantities we are interested in. We can now invert these expressions to find how G_c and R_s depend on temperature.

$$G_c = \frac{2}{wL}\frac{\tilde{R}_2}{\tilde{R}_2^2 - R_3^2}\ln\left(\frac{\tilde{R}_2}{R_3}\right) \tag{B.14}$$

and

$$R_s = \frac{w}{2L}\frac{\tilde{R}_2^2 - R_3^2}{R_2^2}\ln\left(\frac{\tilde{R}_2}{R_3}\right) \tag{B.15}$$

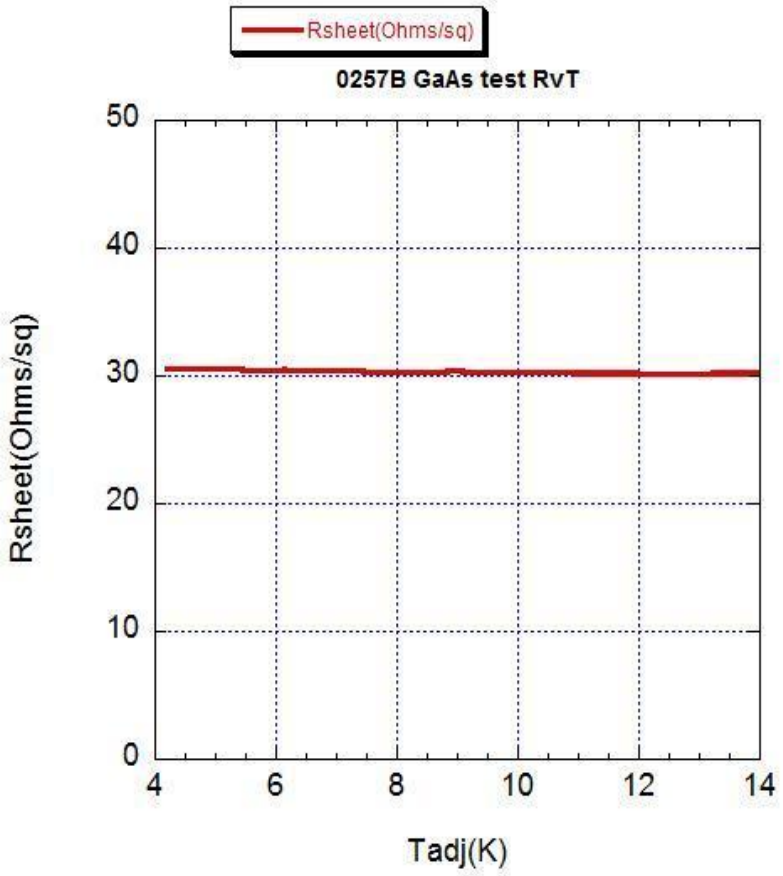

Figure B.5: Resistance versus temperature of semiconducting film without superconducting contacts. Without the presence of superconductivity the RvT curve is completely flat as the temperature drops.

B.2 Validity of Model

These equations allow us to take the raw voltage and current measurements as a function of temperature and instead convert these into having the intrinsic quantities as a function of temperature as is shown in Figure B.4. It seems that there is potentially one free parameter here, the parasitic resistance of the semiconducting gap, $R_{gap} = \left(\frac{R_{s_0} d}{w} \right)$,

that folds into $\tilde{R}_2$. However, choice of R_{gap} is constrained in three ways. First, Van der Pauw measurements of the other pieces of the same wafer can be performed as a function of temperature down to 4 Kelvin. As is seen in Figure B.5, these structures are degenerately doped dirty semiconductors, and the sheet resistance of these films is constant at low temperatures. Thus the value of the normal state sheet resistance is well known for all temperatures. This fact, coupled with accurate measurements of the geometrical width and length of the gap from microscopy allow for the proper subtraction of this parasitic resistance. Secondly, the device is asymmetric, it is also possible to reverse the upstream and downstream electrodes and obtain a new set of resistance versus temperature curves that differ solely on the value of the contribution of the semiconducting gap due to the different geometrical size. Finally, the analysis can be performed and $R_s(T)$ obtained for a range of values of R_{s_0}. Since just below the critical temperature of the niobium there will not be any measurable proximity effect on the semiconductor, the predicted value of the sheet resistance beneath the injector finger should be identical to the measured normal state film value at that temperature. This provides a self consistent check on the value of the semiconducting gap resistance, and in good samples all three methods of determining the value of R_{gap} agree.

Even if the subtracted resistance was off slightly and there were a compounding series of events that made the values still be self consistent the general shape of the extracted datasets are fairly stable with regard to what the magnitude of the resistance that is subtracted from R_2. Figure B.6 shows how these predicted intrinsic values behave for a real device. While the shape of the curves are the same, they are offset at T_c by different values. The correct choice for R_{s0} for this device was 11.6 Ohms since it predicts a normal sheet resistance in the GaAs of 32.5 Ohms, almost exactly what was measured in the Van der Pauw sample at this temperature. Also with a measured geometrical aspect ratio of 4/11, the extracted normal state R_s will predict a value for the semiconducting gap of 11.8 Ohms, very close to the 11.6 Ohms that were subtracted implying self-consistency. If we examine the other curves, the one that subtracted 10.6 Ohms predicts a normal state resistance of 49.5 Ohms, far from the measured value of the film, and its self consistent prediction for the semiconducting gap is 18 Ohms, 40%

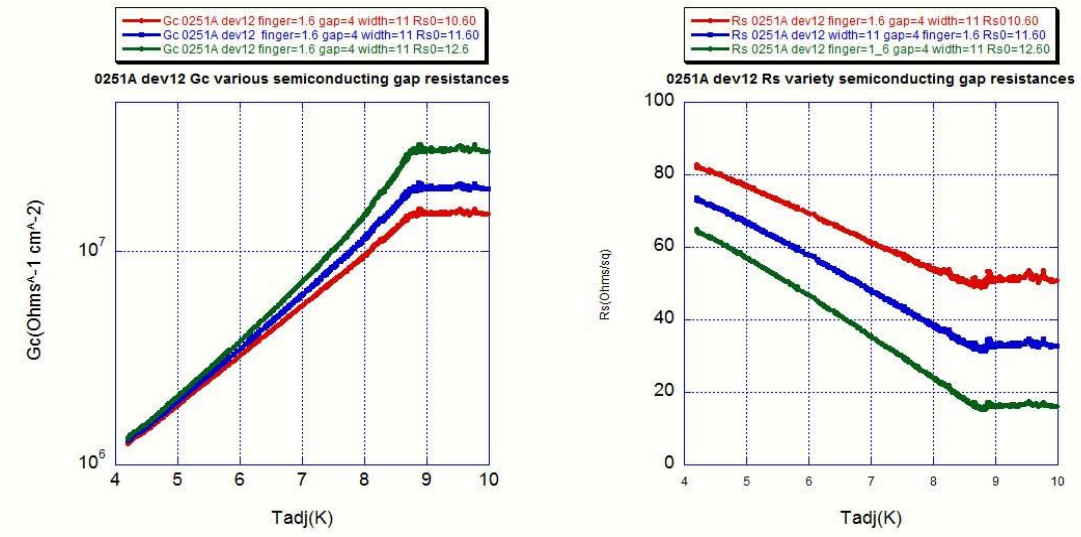

Figure B.6: Extracted datasets for the junction conductance and the sheet resistance as a function of temperature. Note that while they have the same shape, the G_c and R_s plots lie at different points.

higher than the value used in the model. The same is also true for the curve subtracting 12.6 Ohms. The 15 Ohm prediction for the normal state sheet resistance is far too low, and the self consistent prediction for the semiconducting gap is 5.4 Ohms, only a third of the hypothesized value. Despite the tremendous quantitative differences in the predictions, all three curves have similar shapes implying that we can make even stronger qualitative conclusions about the shape of the temperature dependence of the junction conductance and sheet resistance in the semiconductor.

B.3 Thin Trench Device Modeling

Schematically the lone voltage measurement can be thought of as the sum of three voltages in series, the voltage drop across the first N-S contact, the voltage drop across the thin semiconducting gap, and the voltage drop across the second N-S contact. Since these three measurements are all in series they will all share the same current and can equivalently be thought of as resistances. As the effective length of each N-S junction is hundreds of microns, the two contacts are both in the long junction limit and are identical. Therefore, the measured resistance R_{meas} of the device will be

$$R_{meas} = R_{trench} + 2R_{interface}. \tag{B.16}$$

R_{trench} and $R_{interface}$ are the resistances of the semiconducting trench and the N-S interface respectively. Since the N-S contacts are in the long junction limit, their resistance can be rewritten in terms of the transfer length λ and the width of the junction w using the model developed in Appendix B. The measured resistance will be

$$R_{meas} = R_{trench} + \frac{2}{G_c w \lambda}. \tag{B.17}$$

G_c is the specific conductance of the contact in units of $Ohms^{-1}cm^{-2}$. Since the transfer length is $\lambda = \frac{1}{\sqrt{G_c R_s}}$, we can now rewrite the expression for the measured resistance in terms of the intrinsic properties of the device and its geometrical measurements.

$$R_{meas} = R_{s_0} \frac{d}{w} + \frac{2}{w} \sqrt{\frac{R_s}{G_c}} \,. \tag{B.18}$$

The trench resistance has now also been rewritten in terms of the unadulterated sheet resistance of the semiconductor, R_{s_0}, and its geometrical length, d, and width, w.

Unlike the results of the three terminal model, there is only one measured resistance and two unknowns, R_s and G_c. However, the value of the sheet resistance of the semiconductor is known just below the critical temperature of the semiconductor. At this temperature the measurement does not include any lead resistance, but superconductivity has not yet been able to influence the underlying semiconductor. Therefore, the sheet resistance of the semiconductor at this temperature will be identical to the normal state sheet resistance. This resistance is well known as it was measured in both the Van der Pauw sample at that temperature, and at another test structure elsewhere on the device wafer. Using the known sheet resistance we can then find the value of the junction conductance just below T_c as an independent check to the transparency of our devices. Rewriting Equation 6.6, the junction conductance at T_c will be

$$G_c(T_c) = \frac{4R_{s_0}}{w^2 \left(R_{meas} - R_{s_0} \frac{d}{w} \right)^2} \,. \tag{B.19}$$

Notice how G_c and R_s are intertwined in the measurement and cannot be separated. This illustrates how a single four point measurement cannot by itself provide the information needed to fully understand the proximity effect.

References

[1] A Kastalsky, A Kleinsasser, L Greene. et. al. *Phys. Rev. Lett.* **67** 3026 1991

[2] Yu. Nazarov. *Phys. Rev. Lett.* **73** 1420. 1994

[3] K Usadel. *Phys. Rev. Lett.* **25** 507 1970

[4] Flexner, Soren. *Fluctuating and Phase Stiff Proximity Induced Superconductivity in Superconductor-Semiconductor Junctions* Dissertation. University of Illinois. 2006

[5] G E Blonder, M Tinkham, T M Klapwijk. *Phys. Rev. B* **25** 4515 1982

[6] J Bardeen, L Cooper, J Schrieffer. *Phys. Rev. B*. **108** 1175. 1957

[7] P G de Gennes. 1966 *Superconductivity in Metals and Alloys* (New York: Benjamin)

[8] E V Thuneberg. *Journal of Low Temperature Physics*. **91** 49 1992.

[9] L P Gor'kov. Sov. Phys. JETP **7** 505. 1958

[10] A A Abrikosov, L P Gor'kov, I E Dzyaloshinskii. 1963 *Method of Quantum Field Theory in Statistical Mechanics* (London: Pergamon)

[11] P G de Gennes. *Rev. Mod. Phys*. **36** 225. 1964

[12] G Deutscher, P G de Gennes. Superconductivity Vol 2. ed R D Parks (New York: Dekker) p1005 1969

[13] T M Klapwijk. *Journal of Superconductivity: Incorporating Novel Magnetism* **17** 593. 2004

[14] J Rammer, H Smith. *Rev. Mod. Phys*. **58** 323. 1986

[15] G Eilenberger. *Z. Phys*. **214** 195. 1968

[16] Gueron, Sophie *Quasiparticles in a Diffusive Conductor: Interaction and Pairing* Dissertation. CEA-Saclay. 1997.

[17] W Belzig, C Bruder, G Schon. *Phys. Rev. B* **54** 9443. 1996

[18] F Giazotto, P Pingue, F Beltram, et. al *Phys. Rev. Lett*. **87** 216808-1 2001

[19] R Taboryski, T Clausen, J B Hansen, et. al. *Appl. Phys. Lett*. **69** 656 1996

[20] C Nguyen, H Kroemer, E L Hu. *Phys. Rev. Lett*. **69** 2847 1992

[21] W L McMillan. *Phys. Rev*. **175** 559 1968

[22] B van Wees, P de Vries, P Magnee, T Klapwijk. *Phys. Rev. Lett*. **69** 510 1992

[23] C Nguyen, H Kroemer, E Hu. *Appl. Phys. Lett*. **65** 103. 1994

[24] M Thomas, H Blank, K Wong, H Kroemer, E Hu. *Phys. Rev. B* **58** 11676. 1998

[25] R Landauer. IBM *J. Res. Dev*. **32** 306. 1988

[26] S Datta. *Electronic Transport in Mesoscopic Systems* (Cambridge University Press, Cambridge) 1995

[27] G. Snider, 1D Poisson Solver, URL http://www.nd.edu/ gsnider/.

[28] N Ashcroft, D Mermin. *Solid State Physics*. Harcourt College Publishers. Fort Worth, Tx. 1976.

[29] G Blonder. *The I-V Curves of Superconducting Microconstrictions*. Dissertation. Harvard University. 1982

[30] E Parker. Ed. *The Technology and Physics of Molecular Beam Epitaxy* Plenum Press, New York, NY. 1985

[31] Williams, R. *Gallium Arsenide Processing Techniques* Artech House Inc, Dedham, MA. 1984

[32] S Ghandhi. *VLSI Fabrication Principles Silicon and Gallium Arsenide* John Wiley and Sons, New York, NY. 1983

[33] A R Clawson. *Materials Science and Engineering* **31** 1. 2001

[34] K Williams, K Gupta, and M Wasilik. *Journal of Microelectromechanical Systems* **12** 761. 2003

[35] K v Klitzing, G Dorda, M Pepper. *Phys. Rev. Lett*. **45** 494. 1980

[36] D Tsui, H Stormer, A Gossard. *Phys. Rev. Lett*. **48** 1559. 1982

[37] S Law. private communication

[38] C Foxon, B Joyce. *Journal of Crystal Growth* **44** 75. 1978

[39] D Leonard, K Pond, P Petroff. *Phys. Rev. B* **50** 11687. 1994

[40] L Pfeiffer, E Schubert, K West. *Appl. Phys. Lett*. **58** 2258. 1991

[41] Dobblaere et al. *Appl. Phys. Lett.* **60** 568. 1992

[42] P Welander. *Epitaxial Aluminum Oxide Thin films on Niobium(110)* Dissertation. University of Illinois. 2007

[43] L van der Pauw. *Phillips Technical Review* **20** 220. 1958

[44] E Hall. *Am. J. Math* **2** 287. 1879

[45] T McArdle. *Resistance in Superconducting Epitaxial Niobium Nanowires Dissertation*. University of Illinois 2009.

[46] T Van Duzer. *Superconductive Devices and Circuits* Prentice Hall, Upper Saddle River, NJ. 1999

[47] P Charlat, H Courtois, Ph. Gandit. et al. *Czech J Phys.* **46** Supplement S6, 3107. 1996

[48] M P A Fisher. *Phys. Rev. B* **49** 14550. 1994

[49] Veeco Compound Semiconductor. Vapor Pressures of Selected Elements URL:www.veeco.com

[50] G Arfken, H Weber. *Mathematical Models for Physicists*, 6th Ed Academic Press. Burlington, MA. 2005

[51] L Pfeiffer, K West, H Stormer, K Baldwin. *Appl. Phys. Lett*. **55** 1888. 1989

[52] A Ohtake, M Ozeki, T Yasuda, T Hanada. *Phys. Rev. B* **65** 165315. 2002

[53] H Farrell, C Palmstrom. *J. Vac. Sci. Technol B* **8** 903. 1990

Author's Biography

Mike was born in Houston, Texas on June 26, 1981 to his parents William and Barbara Vissers. He has a twin sister Sarah who due to the tyranny of the alphabet spent far too many years sitting next to him in school. He married Jennifer Eddins in Austin, Texas on June 18, 2005.

After spending time in three different Houston area school districts he graduated from Katy High School in suburban Houston in the spring of 1999. That fall he began to attend the University of Texas in Austin initially majoring in Physics but later also in Math. He graduated four years later with Bachelor of Science degrees in both Physics and Pure Mathematics.

In August of 2003, he began his studies at the University of Illinois in Urbana-Champaign. He was a teaching assistant for 9 semesters, teaching discussion and laboratory sections in the Physics Department. He taught the entire introductory physics sequence for scientists and engineers as well as the Advanced Electronics lab. He began working in Jim Eckstein's lab in the spring of 2004. After graduation Mike will join the National Institute of Standards and Technology in Boulder, Colorado as a post-doctoral researcher.